Lawrence Berkeley National Laboratory
Recent Work

Title
WORKSHOP ON MODELING OF ELECTRICAL AMD ELECTROMAGNETIC METHODS. PROCEEDINGS, MAY 17-19, 1978

Permalink
https://escholarship.org/uc/item/0qc701qv

Author
Lawrence Berkeley National Laboratory

Publication Date
1978-12-04

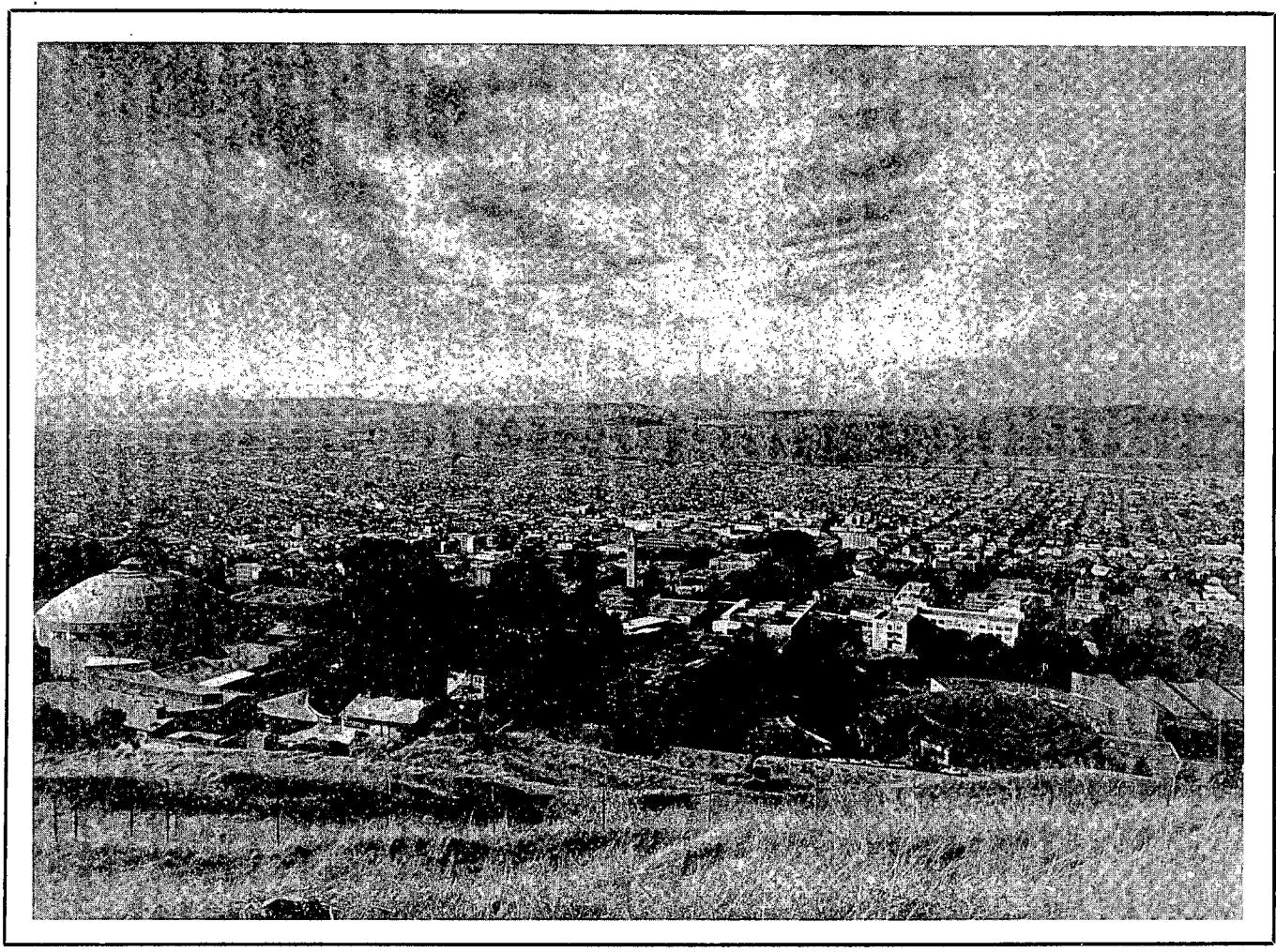# WORKSHOP ON MODELING OF ELECTRICAL AND ELECTROMAGNETIC METHODS

PROCEEDINGS

MASTER

May 17 - 19, 1978

Earth Sciences Division

Lawrence Berkeley Laboratory/University of California
Berkeley, California

DISCLAIMER

This report was prepared as an account of work sponsored by an agency of the United States Government. Neither the United States Government nor any agency Thereof, nor any of their employees, makes any warranty, express or implied, or assumes any legal liability or responsibility for the accuracy, completeness, or usefulness of any information, apparatus, product, or process disclosed, or represents that its use would not infringe privately owned rights. Reference herein to any specific commercial product, process, or service by trade name, trademark, manufacturer, or otherwise does not necessarily constitute or imply its endorsement, recommendation, or favoring by the United States Government or any agency thereof. The views and opinions of authors expressed herein do not necessarily state or reflect those of the United States Government or any agency thereof.

DISCLAIMER

Portions of this document may be illegible in electronic image products. Images are produced from the best available original document.

PROCEEDINGS OF THE WORKSHOP ON MODELING OF ELECTRIC

AND ELECTROMAGNETIC METHODS

May 17-19, 1978

Lawrence Berkeley Laboratory
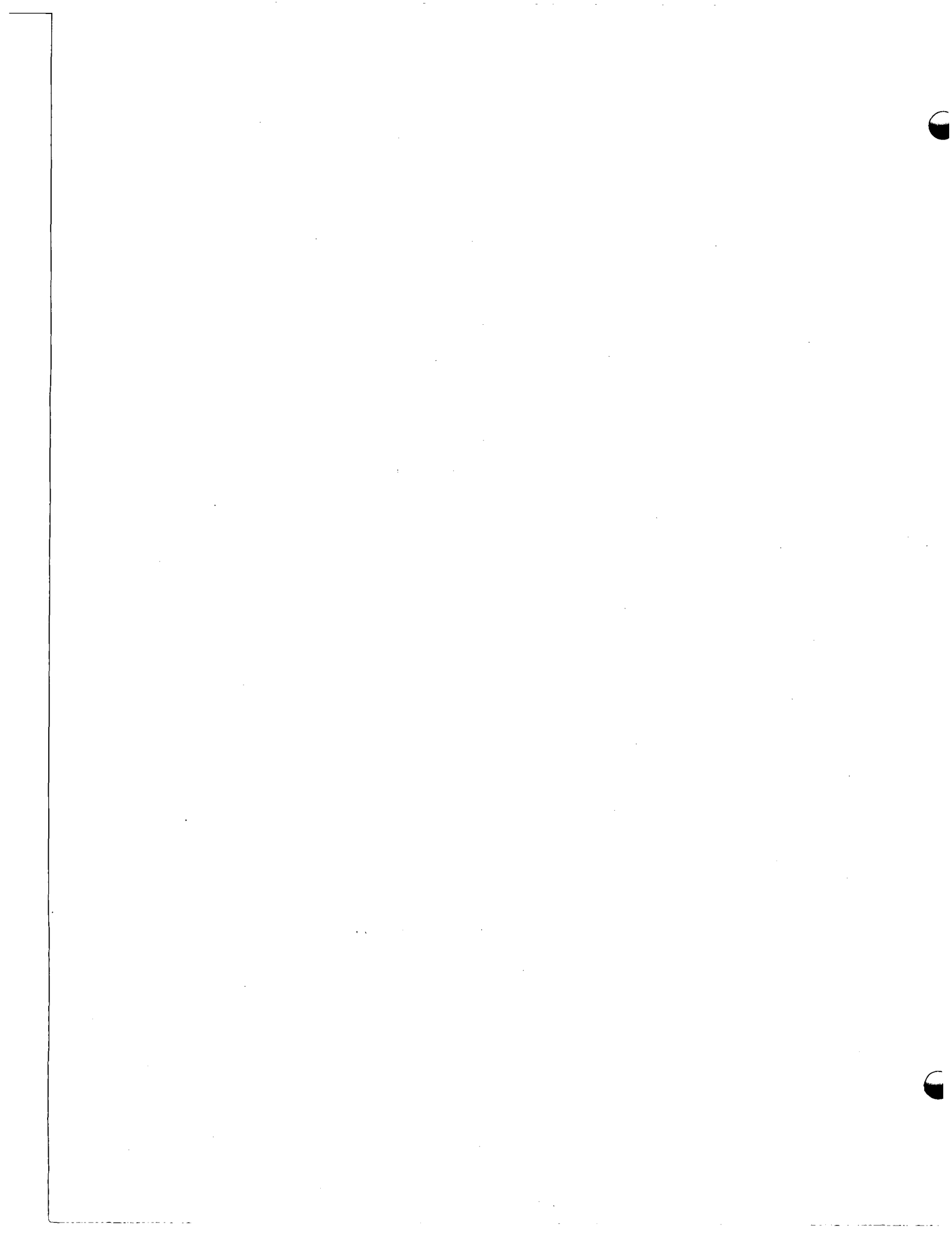University of California
Berkeley, California

TABLE OF CONTENTS

INTRODUCTION

The workshop on the Modeling of Electrical and Electromagnetic Methods was held at the Lawrence Berkeley Laboratory on May 17, 18, and 19, 1978. It was sponsored by the U.S. Department of Energy through the University of California, Lawrence Berkeley Laboratory, Division of Earth Sciences, and the University of Utah; together with the National Science Foundation (RANN Division) through the University of Utah. The purpose of the workshop was to bring together active workers in the field of numerical and scale modeling to discuss progress, results, and problems associated with the various techniques that apply. The work reported by many of the invited participants is or was funded through the DOE geothermal or fossil fuel programs; other participants from industry and universities are concerned either with mineral exploration or more general crustal studies problems.

The workshop was divided into six sessions: finite element method, finite difference method, integral equation method, two sessions on 'other techniques', and a conclusion and recommendation session. Authors were asked to make their presentations quite technical, concentrating as much on the problems encountered in their techniques as on the final results.

Papers originating outside LBL were printed directly from the manuscripts submitted by the authors.

MAGNETOTELLURIC OBSERVATIONS AT THE ROOSEVELT

HOT SPRINGS KGRA AND MINERAL MTS., UTAH

Philip Wannamaker
University of Utah

Abstract

Twenty-five magnetotelluric soundings in the Roosevelt Hot Springs area indicate a very complicated, three-dimensional electrical environment. The assembly of a profile of one-dimensional, transverse electric interpretations yields a calculated 2-D apparent resistivity-frequency pseudosection far removed from the observed data. Trial-and-error modelling improves the fit only a little. The most notable difficulty, the presence in both TE and TM pseudosections of pronounced contrasts in ρ_a persisting to the lowest observed frequency, may be explained by the discontinuities in electric field that are found for all directions of wave excitation for 3-D geometries.

The estimation of electrical strike is also difficult in the 3-D case since the total fields do not decompose into the two principal excitation modes. Whenever a plane of symmetry exists, the estimated electrical strike will be normal to it; otherwise an oblique estimation results. The observed consistency of strike estimation at Roosevelt is likely due to the gross, elongate, resistive horst-structure of the Mineral Mts. in surrounding conductive valley fill. Mode identification and the effects of near-surface 3-D inhomogeneities pose potential major limitations to the magnetotelluric method.

*   *   *

Previous active source electrical and electromagnetic measurements show a range of interpreted true resistivities spanning 3 to 10^3 Ω-m at the Roosevelt Hot Springs KGRA. Contour pattern lows of first separation dipole-dipole apparent resistivity values are roughly coincident with highs of near-surface thermal gradient measurements. During the summer of 1976, twenty-five magnetotelluric (MT) soundings were obtained in the vicinity of the Roosevelt Hot Springs in an attempt to describe any possible deep conductive heat source for the conductive hydrothermal system (see Figure 1).

Sources of electrical conductivity to consider are electrolytic conduction through pore passages, surface conduction along mineral surfaces, thermally activated semiconduction, and electrolytic conduction in wet, partial melts. The Basin and Range tectonic province conductivity model of W. F. Brace in the AGU Monograph 14 (1971) is used as a rough standard by which to judge the observed MT results. Petrological work on the Mineral Mts. rhyolitic volcanics indicated substantial magma chambers existed at indeterminate depths as little as 0.5 myrs. ago. Any present-day partially molten magmas may be detected electrically.

As is the standard procedure, 1-D layered and continuous inversions of the transverse electric (TE) data for several individual sites were performed. In the conductive Milford Valley graben, values of apparent resistivity drop to 0.10 Ω-m for the lowest frequencies of observation and interpreted true resistivities are below 0.02 Ω-m. Such results are unreasonable in the light of established notions about conductivities of earth materials. Soundings in the Mineral Mts. granodiorite are more reasonable although, compared to the Brace model, interpreted true resistivities are low by a factor of 5 to 10 while interface depths are too shallow by a factor of 2 or more.

Multifrequency apparent resistivity data for a profile of 12 MT stations is presented in the form of frequency-distance pseudosections for both TE and TM modes of wave excitation (see Figs. 2 and 3). The major difference between the two pseudosections involves the overall level of ρ_a values. Except perhaps for the westernmost stations on conductive valley fill, the TM values generally exceed those of TE by a factor of about ten. One important common characteristic is the presence of pronounced, station-to-station apparent resistivity contrasts enduring to the lowest frequency of observation at two of the sites. For use as an interpretational starting point, the best-fit discrete-layer inversion results for each of the twelve stations in the profile were stitched together to form a crude, initial 2-D estimate of the resistivity structure (see Fig. 4). The computed TE, 2-D pseudosection for this ensemble matches the observed ρ_a section only for the stations in the conductive graben and for the very high frequency values for the rest of the stations (see Fig. 5). Trial-and-error attempts at improving the basic model yield an adequate fit only down to about 0.5 Hz whereafter the degeneration of agreement is marked (see Figs. 6 and 7). A TM pseudosection calculation for the 1-D assembly agrees very well with the observed TE contours however TE modelled does not agree whatsoever with TM observed so a mere mode misidentification is not the answer (Fig. 8).

Some outcropping, single conductor, multifrequency, TE and TM model results may explain some of the problems in terms of 3-D effects (Fig. 9). In the 2-D, TE model, continuity of tangential electric field ($\vec{E}_t$) parallel to media boundaries requires a continuous apparent resistivity function for all frequencies. In the TM model, the electric vector is orthogonal to the media contacts, normal current density ($\vec{J}_n$) must be continuous, and so the total electric vector at the contacts will be discontinuous by a factor of (ρ_1/ρ_2). For the TM case, $\rho_a \sim E^2$ so one expects and observes a $(\rho_1/\rho_2)^2$ discontinuity at vertical contacts for all frequencies. Please note that the apparent resistivity values within the prism are greatly depressed below the true value while those outside are only slightly elevated w.r.t. the true resistivity. The anomaly for a simple, outcropping, conductive 3-D prism will possess characteristics of both TE and TM 2-D models (see Fig. 10). Measurements along line A-A' (with $\vec{E}$ normal to the resistivity discontinuity) will yield a profile resembling a TM excitation. Continuity of $\vec{J}_n$ requires that the $(\rho_1/\rho_2)^2$ discontinuity in ρ_a be present for all frequencies. Measurements along line B-B' (with $\vec{E}$ parallel to the resistivity discontinuity) will give a profile resembling a TE situation. Continuity of $\vec{E}_t$ requires a smooth ρ_a curve.

Analogous $\rho_a(\omega)$ profiles will appear for an $\vec{E}$ polarization orthogonal to that depicted. Line A-A' would be "TE" and line B-B' would be "TM". Hence, finally, a map view of the anomaly of this 3-D body will consist of pronounced ρ_a contours lasting down to the lowest frequency measured. Since in the field both E_x and E_y are present, then regardless of which observed pseudosection (TE or TM) is chosen, a profile across a conductive prism of finite strike length will exhibit such exaggerated, persisting contrasts in ρ_a. The enclosed pseudosections contain examples of this very phenomenon and they cannot be fit by any purely two-dimensional model.

Depth of exploration is another problem in 3-D environments. A 2-D, TM model of a deeply extending conductive model is very similar to the previous shallow model and one may reason as above that the 3-D anomalies will also be very similar. MT soundings within such 3-D conductive prisms may provide no meaningful information about deeper structures.

The plane wave mode identification (i.e. estimation of electrical strike) is also difficult in the 3-D case. Standard strike estimation procedures assume approximate two-dimensionality where the vertical component of magnetic field, H_z, is linearly related to, or completely coherent with, only the component of $\vec{E}$ parallel to strike (say E_x). The relation is defined by Maxwell's second equation, in the general case, as

$$H_z = \frac{-1}{i\omega\mu_o}\left[\frac{\partial E_x}{\partial y} - \frac{\partial E_y}{dx}\right].$$

In the 2-D case, $\partial/\partial x = 0$ so the above reduces to

$$H_z = \frac{-1}{i\omega\mu_o}\frac{\partial E_x}{\partial y} = Y_{zx} E_x$$

where Y_{zx} is the admittance. In the field, neither measurement electrode is likely to be parallel to strike and a component of E_x will be in each electric record. If x' and y' represent the measurement axes, then one must write

$$H_z = Y_{zx'} E_{x'} + Y_{zy'} E_{y'}$$

where $Y_{zx'}$ and $Y_{zy'}$ are the relevant admittance functions determined by standard spectral analysis techniques. The patent approach is to rotate mathematically the measurement axes to maximize $Y_{zx'}$ and the corresponding x'-direction is estimated strike. In three dimensions, however, H_z no longer depends on a single direction of electric vector. Referring to Fig. 10, from symmetry observe that along A-A', $\partial/\partial y = 0$, H_z will be wholly related to E_y and the estimated strike will be along the y-axis. Along B-B', $\partial/\partial x = 0$, H_z will be wholly related to E_x and the estimated strike will be along the x-axis. Along diagonals of the prism, both derivatives are important and an oblique estimation will result.

The mode identification for the Roosevelt Hot Springs stations is pretty consistent, however, and parallels the long axis of the Mineral Mts. Regional structure is likely responsible. The mountains form a very elongate,

north-south trending resistive body flanked on the west by deep, very conductive alluvium and to a minor extent on the east by the same. Especially for east-west profiles across the central portions of this range, $\partial/\partial y \gg \partial/\partial x$ where x is the north-south axis of the mountains. The consistency in the electrical strike estimation does not appear related to smaller-scale hot-spring structures but instead to the gross topography of the region.
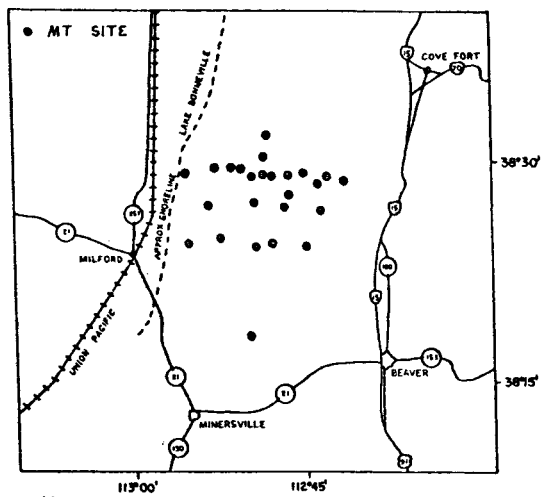
FIGURE 1: Roosevelt Hot Springs KGRA
location of MT Soundings

FIGURE 2: Observed transverse electric apparent resistivity
pseudosection for MT stations 1 through 12. Values of
contours are in Ω-m.

FIGURE 3: Observed transverse magnetic apparent resistivity
pseudosection for MT stations 1 through 12. Values of
contours are in Ω-m.
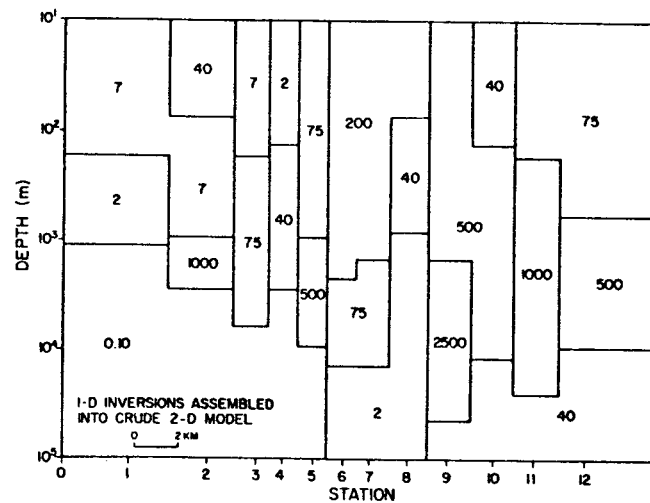
FIGURE 4: Assembly of best-fit, discrete-layer inversion results
(TE mode) for stations 1 through 12. Resistivities are
in Ω-m.

TE ρa MODELED
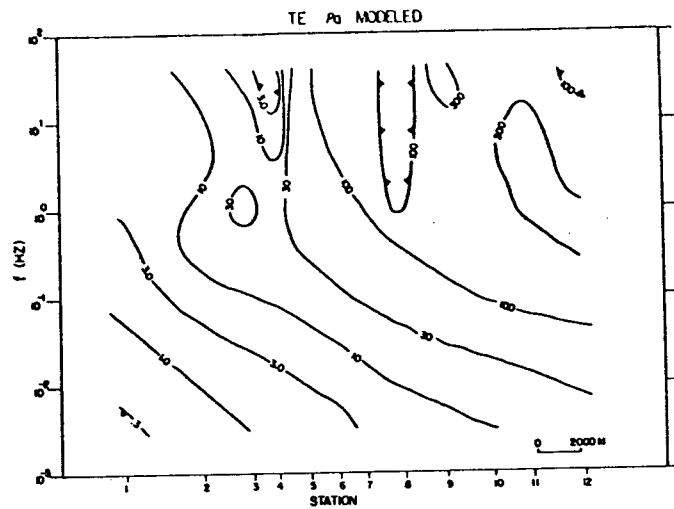
FIGURE 5: Transverse electric 2-D finite element pseudosection calculated for preceding one-dimensional assembly.

FIGURE 6: Trial-and-error best-fit model for observed transverse electric pseudosection of Figure 9. Resistivities are in Ω-m.

TE ITERATIVE BEST FIT

FIGURE 7: Calculated apparent resistivity pseudosection for previous trial-and-error best-fit model. Contours are in Ω-m.

TM ρa MODELED
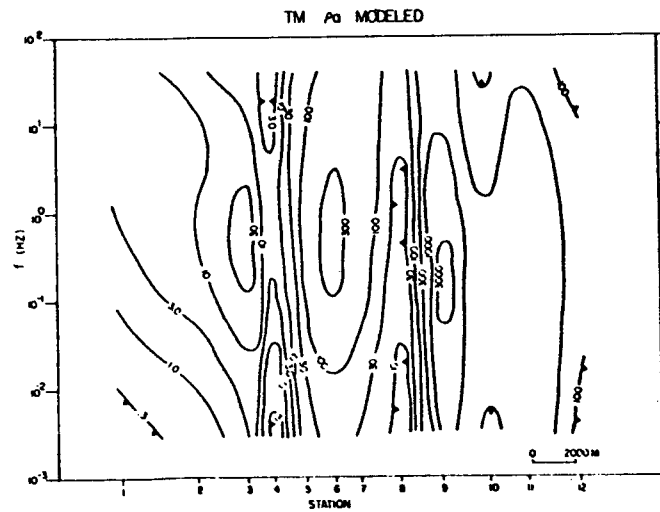
FIGURE 8: Transverse magnetic 2-D pseudosection for the one-dimensional assembly of Figure 11.
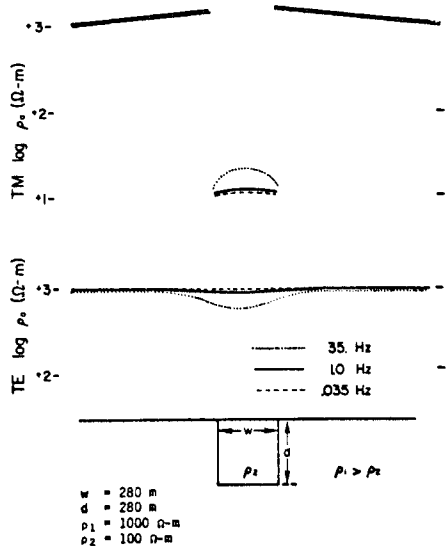
FIGURE 9: TM and TE multifrequency profiles for single, outcropping, shallow, 2-D conductor.

w = 280 m
d = 280 m
ρ_1 = 1000 Ω-m
ρ_2 = 100 Ω-m

35. Hz
10 Hz
.035 Hz

$\rho_1 > \rho_2$
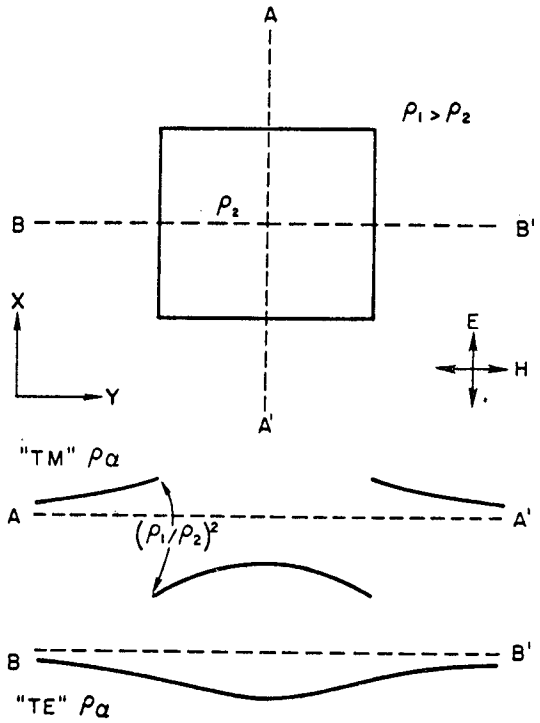
FIGURE 10: Conductive rectangular prism in resistive environment plus proposed apparent resistivity signatures for single polarization of electric vector.

LEGEND

FIGURE 11
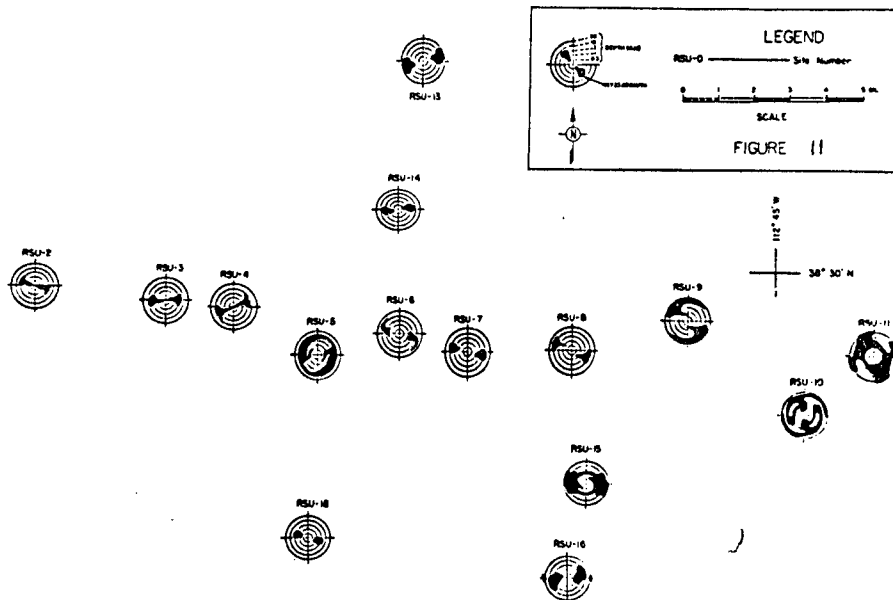
APPLICATION OF THE FINITE ELEMENT METHOD TO THE
FINITE SOURCE 2-D EARTH E-M PROBLEM

John Stodt
The University of Utah
Salt Lake City 84112

An outline of the application of the Galerkin finite element method to the solution of the finite source 2-D earth E-M problem is presented. The conventions used are the following:

1) e^{+jwt} time dependence

2) Spatial Fourier transform pair:

$$F(k_x) = \int_{-\infty}^{\infty} f(x) e^{-j2\pi k_x x} dx \quad ; \quad f(x) = \int_{-\infty}^{\infty} F(k_x) e^{+j2\pi k_x x} dk_x$$

3) Right hand coordinate system with x the strike direction, z positive down.

Maxwell's equations with electric and magnetic sources may be written as follows:

(1) $$\nabla \times \vec{E} = -jw\mu[\vec{H} + \vec{M}_s]$$

(2) $$\nabla \times \vec{H} = (\sigma + jw\varepsilon)\vec{E} + \vec{J}_s \equiv \hat{y}\vec{E} + \vec{J}_s$$

where

$$\vec{M}_s = \hat{m}\,\delta(x)\delta(y)\delta(z) \qquad \hat{m} \equiv \text{magnetic moment} \qquad \vec{J}_s = \vec{J}\,\delta(x)\delta(y)\delta(z)$$

It is possible to treat equations 1 and 2 directly when applying the finite element technique, or else one can re-formulate the problem in terms of secondary fields. The advantage of the latter approach lies in the ease with which the resulting "fictitious" sources may be handled with the finite element methodology. In addition, the secondary fields are smoother, allowing coarser meshes to be used. The price one says is that the primary fields must be found at each node point in the earth where 2-D inhomogenieties exist.

To develop the appropriate set of equations let

$$\tilde{E} \equiv \tilde{E}_p + \tilde{E}_s$$

$$\tilde{H} \equiv \tilde{H}_p + \tilde{H}_s$$

$$\sigma(y,z) \equiv \sigma_p(\mathbf{z}) + \sigma_s(y,z)$$

where subscripts p, s denote primary, secondary respectively. Let the primary field be the solution to the finite source layered earth problem. Equations (1) and (2) become:

$$(3) \qquad \nabla \times (\tilde{E}_p + \tilde{E}_s) = -jw\mu \ (\tilde{H}_p + \tilde{H}_s + \tilde{M}_s)$$

$$(4) \qquad \nabla \times (\tilde{H}_p + \tilde{H}_s) = (\sigma_p(z) + \sigma_s(y,z) + jw\epsilon)(\tilde{E}_p + \tilde{E}_s) + \tilde{J}_s$$

$\tilde{E}_p$, $\tilde{H}_p$ have been defined as solutions to

$$(5) \qquad \nabla \times \tilde{E}_p = -jw\mu \ [\tilde{H}_p + \tilde{M}_s]$$

$$(6) \qquad \nabla \times \tilde{H}_p = (\sigma_p(z) + jw\epsilon) \ \tilde{E}_p + \tilde{J}_s$$

Substitution of (5) and (6) into (3) and (4) yields

$$(7) \qquad \nabla \times \tilde{E}_s = -jw\mu \tilde{H}_s$$

$$(8) \qquad \nabla \times \tilde{H}_s = [\sigma(y,z) + jw\epsilon] \ \tilde{E}_s + \sigma_s(y,z) \ \tilde{E}_p$$

These last equations can now be solved for the secondary fields, due to the "ficticious" source $\sigma_s(y,z) \ \tilde{E}_p$.

Finite element analysis may now be applied to either eqns. (1) and (2) or (7) and (8). The approach is similar, differing only in how the source terms are handled. The approach taken will be to Fourier transform the strike direction out of Maxwell's equations and rearrange them to obtain

$$\hat{E}_{ys} = -\varphi\left[j\bar{F}_x\frac{\partial\hat{E}_{xs}}{\partial y} - jw\mu\frac{\partial\hat{H}_{xs}}{\partial z} + jw\mu\sigma_s\hat{E}_{yp}\right]$$

(10)

$$\hat{E}_{zs} = -\varphi\left[j\bar{F}_x\frac{\partial\hat{E}_{xs}}{\partial z} + jw\mu\frac{\partial\hat{H}_{xs}}{\partial y} + jw\mu\sigma_s\hat{E}_{zp}\right]$$

where

$$\bar{F}_x = 2\pi k_x \qquad \varphi = \frac{1}{(\bar{F}_x^2 - k^2)} \qquad k^2 = w^2\mu\varepsilon - jw\mu\sigma$$

Substituting equations 10 into the top two expressions of the set 9, we obtain two coupled second order equations to be solved simultaneously over (y,z) at fixed K_x for E_{xs} and H_{xs}. They are:

(11)

$$\nabla \times \varphi\vec{A} \circ \vec{\iota} = -jw\mu\hat{H}_{xs}$$

$$\nabla \times \varphi\vec{B} \circ \vec{\iota} = \hat{\gamma}\hat{E}_{xs} + \sigma_s\hat{E}_{xp}$$

where

$$\vec{A} \equiv \vec{\jmath}\left[-j\bar{F}_x\frac{\partial\hat{E}_{xs}}{\partial y} + jw\mu\frac{\partial\hat{H}_{xs}}{\partial z} - jw\mu\sigma_s\hat{E}_{yp}\right]$$

$$+ \vec{k}\left[-j\bar{F}_x\frac{\partial\hat{E}_{xs}}{\partial z} - jw\mu\frac{\partial\hat{H}_{xs}}{\partial y} - jw\mu\sigma_s\hat{E}_{zp}\right]$$

$$\vec{B} \equiv \vec{\jmath}\left[-j\bar{F}_x\frac{\partial\hat{H}_{xs}}{\partial y} - \hat{\gamma}\frac{\partial\hat{E}_{xs}}{\partial z} - j\bar{F}_x\sigma_s\hat{E}_{zp}\right]$$

$$+ \vec{k}\left[-j\bar{F}_x\frac{\partial\hat{H}_{xs}}{\partial z} + \hat{\gamma}\frac{\partial\hat{E}_{xs}}{\partial y} + j\bar{F}_x\sigma_s\hat{E}_{yp}\right]$$

two coupled equations in the unknown fields. The (y,z) dependence of these equations will then be solved with finite element analysis. The four field components not in the strike direction may then be found from inverse transforms of linear combinations of the fields in the strike direction. A tentative analytic method of evaluation of these four integrals will be discussed. If this technique proves successful, it may be more efficient to obtain E_x and H_x directly form Maxwell's equations rather than by a numerical inverse transformation, where a large number of K_x values may be required.

Re-writing equations 7 and 8 in component form, Fourier transformed with respect to the strike direction, we obtain (the $\wedge$ indicates Fourier transformation):

$$(9) \quad \begin{array}{c|c}
\dfrac{\partial \hat{E}_{zs}}{\partial y} - \dfrac{\partial \hat{E}_{ys}}{\partial z} = -j w \eta \hat{H}_{xs} & \dfrac{\partial \hat{H}_{zs}}{\partial y} - \dfrac{\partial \hat{H}_{ys}}{\partial z} = \hat{\eta}\,\hat{E}_{xs} + \sigma_s \hat{E}_{xp} \\
\hline
\dfrac{\partial \hat{E}_{xs}}{\partial z} - j\bar{k}_x \hat{E}_{zs} = -j w \eta \hat{H}_{ys} & \dfrac{\partial \hat{H}_{xs}}{\partial z} - j\bar{k}_x \hat{H}_{zs} = \hat{\eta}\,\hat{E}_{ys} + \sigma_s \hat{E}_{yp} \\
j\bar{k}_x \hat{E}_{ys} - \dfrac{\partial \hat{E}_{xs}}{\partial y} = -j w \eta \hat{H}_{zs} & j\bar{k}_x \hat{H}_{ys} - \dfrac{\partial \hat{H}_{xs}}{\partial y} = \hat{\eta}\,\hat{E}_{zs} + \sigma_s \hat{E}_{zp}
\end{array}$$

By rearrangement and cross substitution in the bottom four equations of this set, we obtain expressions for E_y, E_z, H_y, H_z in terms of the fields in the strike direction, i.e.

$$\hat{H}_{ys} = -\varphi\left[j\bar{k}_x \frac{\partial \hat{H}_{xs}}{\partial y} + \hat{\eta}\frac{\partial \hat{E}_{xs}}{\partial z} + j\bar{k}_x \sigma_s \hat{E}_{zp} \right]$$

$$(10) \quad \hat{H}_{zs} = -\varphi\left[j\bar{k}_x \frac{\partial \hat{H}_{xs}}{\partial z} - \hat{\eta}\frac{\partial \hat{E}_{xs}}{\partial y} - j\bar{k}_x \sigma_s \hat{E}_{yp} \right]$$

If total fields are being solved for, a similar set of equations
is obtained, i.e.

(12)
$$\nabla \times \varphi \vec{C} \circ \vec{i} = -jw\eta \left[\hat{H}_x + \hat{M}_{sx} \right]$$

$$\nabla \times \varphi \vec{D} \circ \vec{i} = \hat{g} \hat{E}_x + \hat{J}_{sx}$$

where

$$\vec{C} \equiv \vec{j} \left[jw\eta \frac{\partial \hat{H}_x}{\partial z} - j\bar{k}_x \frac{\partial \hat{E}_x}{\partial y} - \bar{k}_x w\eta \hat{M}_{sz} - jw\eta \hat{J}_{sy} \right]$$

$$+ \vec{k} \left[-jw\eta \frac{\partial \hat{H}_x}{\partial y} - j\bar{k}_x \frac{\partial \hat{E}_x}{\partial z} + \bar{k}_x w\eta \hat{M}_{sy} - jw\eta \hat{J}_{sz} \right]$$

$$\vec{D} \equiv \vec{j} \left[-\hat{g} \frac{\partial \hat{E}_x}{\partial z} - j\bar{k}_x \frac{\partial \hat{H}_x}{\partial y} - j\bar{k}_x \hat{J}_{sz} - jw\eta \hat{g} \hat{M}_{sy} \right]$$

$$+ \vec{k} \left[\hat{g} \frac{\partial \hat{E}_x}{\partial y} - j\bar{k}_x \frac{\partial \hat{H}_x}{\partial z} + j\bar{k}_x \hat{J}_{sy} - jw\eta \hat{g} \hat{M}_{sz} \right]$$

Notice that in general, delta function sources occur in equations
12. These need careful handling when the finite element discretization is
obtained. On the other hand, if a solution in terms of secondary fields
is sought, these problems do not arise.

Application of the finite element technique to the solution of equations
11 proceeds as follows. We divide the domain over which a solution is
sought into triangular sub-domains over which the behavior of the fields
is approximated by a linear function of position. The nature of this
approximation is outlined in Figure 1.

Before element equations are derived the right side of equations

11 are manipulated as follows.

recall $\qquad \nabla \times \varphi \vec{A} = \varphi \nabla \times \vec{A} + \nabla \varphi \times \vec{A}$

Application of this identitiy allows us to write

(13) $\qquad \nabla \times \vec{A} \circ \vec{\imath} + \frac{1}{\varphi} \nabla \varphi \times \vec{A} \circ \vec{\imath} = \frac{-j w \mu}{\varphi} \hat{H}_{xs}$

$\qquad \nabla \times \vec{B} \circ \vec{\imath} + \frac{1}{\varphi} \nabla \varphi \times \vec{B} \circ \vec{\imath} = \frac{\hat{\gamma}}{\varphi} \hat{E}_{xs} + \frac{G_s}{\varphi} \hat{E}_{xp}$

Since φ is constant at the element level, the second term on the

left need not be considered when deriving the element equations, as long

as we choose our basis functions so that the known behavior of the fields

(continuity) is preserved at physical property interfaces. We now obtain

discrete element equations by forcing the inner product of the error of

approximation with the basis functions to be zero, i.e.

(14) $\qquad \langle N_n^e, \varepsilon \rangle \equiv \iint_e N_n^e \, \varepsilon \, dS = 0 \qquad n = \vec{\imath}, \vec{\jmath}, \vec{k}$

where $\qquad N_n^e$ and ε are defined in figure 1.

The domain of integration is over the triangular region e. Three types

of integrals are encountered in evaluating 14:

First Type:

$$\iint_e N_n^e \nabla \times \vec{A} \circ \vec{\imath} \, dS = \iint_e \nabla \times N_n^e \vec{A} \circ \vec{\imath} \, dS - \iint_e \nabla N_n^e \times \vec{A} \circ \vec{\imath} \, dS$$

$$= \int_{\delta e} N_n^e \vec{A} \circ d\vec{\ell} - \nabla N_n^e \times \vec{A} \circ \vec{\imath} \iint_e dS$$
$$\underset{O}{\downarrow}$$

Second Type:

$$e.g. \quad jw\mu[\bar{H}_x^2 - K^2]\iint_e \hat{H}_{xs} N_n^e \, dS$$

Third Type:

$$e.g. \quad \sigma_s[\bar{H}_x^2 - K^2]\iint_e \hat{E}_{xp} N_n^e \, dS$$

The second and third types differ in that H_{xs} is approximated linearly over the triangular region e in the usual manner whereas E_{xp} is given only at the nodes. Therefore, two different integral formulas must be used in their evaluation. They are:

Type 2:
$$\iint_e N_i^a N_j^b N_k^c \, dS = \frac{2\,a!\,b!\,c!\,\Delta}{(a+b+c+2)!}$$

Type 3:
$$\iint_e F(y,z)\, G(y,z)\, dS = \left[\frac{\Delta}{12}\right]\left[F_i \; F_j \; F_k\right]\begin{bmatrix} 2 & 1 & 1 \\ 1 & 2 & 1 \\ 1 & 1 & 2 \end{bmatrix}\begin{bmatrix} G_i \\ G_j \\ G_k \end{bmatrix}$$

where

$F(y,z), G(y,z)$ are linear functions defined on the triangular region e

and

$$2\Delta = \begin{vmatrix} 1 & Y_i & Z_i \\ 1 & Y_j & Z_j \\ 1 & Y_k & Z_k \end{vmatrix}$$
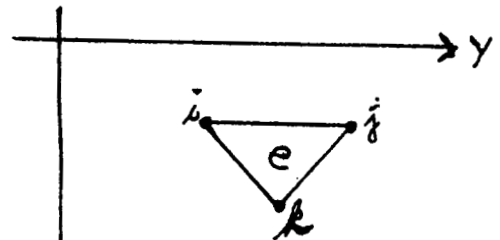
Δ = area of triangular region.

After the integrations in (14) are carried out, the element equations shown in figure 2 are obtained. These element equations are then combined in the usual manner to form the global matrix. The solution of this large scale linear system after application of appropriate boundary condidtions gives the approximate Fourier transformed fields in the strike direction.

The obvious way to obtain the fields in the space domain is to solve the finite element problem for a number of K_x values and then obtain inverse transforms numerically. Computationally this can be very expensive, depending on the number of K_x values needed. It is the purpose of this section to suggest a technique whereby the inverse transforms may be done with what amounts to a contour integration in the complex plane. I do not have all the details worked out, so this section must be considered tentative. Briefly, we desire to evaluate the following integrals:

(15)
$$E_{ys} = \int_{-\infty}^{\infty} \frac{1}{(\bar{k}_x^2 - k^2)} \left[jw_4 \frac{d\hat{H}_{xs}}{dz} - j\bar{k}_x \frac{d\hat{E}_{xs}}{dy} \right] e^{j2\pi k_x x} dk_x$$

$$E_{zs} = \int_{-\infty}^{\infty} \frac{-1}{(\bar{k}_x^2 - k^2)} \left[jw_4 \frac{d\hat{H}_{xs}}{dy} + j\bar{k}_x \frac{d\hat{E}_{xs}}{dz} \right] e^{j2\pi k_x x} dk_x$$

$$H_{ys} = \int_{-\infty}^{\infty} \frac{-\hat{\gamma}}{(\bar{k}_x^2 - k^2)} \left[\frac{d\hat{E}_{xs}}{dz} + j\frac{\bar{k}_x}{\hat{\gamma}} \frac{d\hat{H}_{xs}}{dy} \right] e^{j2\pi k_x x} dk_x$$

$$H_{zs} = \int_{-\infty}^{\infty} \frac{\hat{\gamma}}{(\bar{k}_x^2 - k^2)} \left[\frac{d\hat{E}_{xs}}{dy} - j\frac{\bar{k}_x}{\hat{\gamma}} \frac{d\hat{H}_{xs}}{dz} \right] e^{j2\pi k_x x} dk_x$$

These are all of the form

$$f(x) = \int_{-\infty}^{\infty} \frac{A}{(k_x^2 - k^2)} F(k_x) e^{j 2\pi k_x x} dk_x$$

We desire to evaluate these integrals at x=0, i.e.

$$f(0) = \frac{A}{2\bar{k}} \int_{-\infty}^{\infty} \left[\frac{F(k_x)}{k_x - \bar{k}} - \frac{F(k_x)}{k_x + \bar{k}} \right] dk_x$$

(16)

$$\text{where} \quad \bar{k} = k/2\pi = a - jb \qquad a, b > 0$$

$$\text{and} \quad k^2 = w^2 \mu \varepsilon - jw\mu\sigma$$

To evaluate (15), make use of the following properties of Fourier transforms:

$$F(k_x) = F_+(k_x) + E(k_x) = \int_{-\infty}^{0} f(x) e^{-j 2\pi k_x x} dx + \int_{0}^{\infty} f(x) e^{-j 2\pi k_x x} dx$$

where

(17) $\quad F_+(z) = \frac{1}{2\pi j} \int_{-\infty}^{\infty} \frac{F(t) dt}{t - z} \qquad z = k_x + jy \quad y > 0 \qquad$ *analytic in upper z-plane*

$\quad E_-(z) = \frac{-1}{2\pi j} \int_{-\infty}^{\infty} \frac{F(t) dt}{t - z} \qquad z = k_x - jy \quad y > 0 \qquad$ *analytic in lower z-plane*

$$\text{and} \quad \lim_{y \to 0^+} F_+(z), E_-(z) = F_+(k_x), F_-(k_x)$$

We see immediately that the integral 16 is of the form 17. The answer is:

$$f(0) = \frac{-2\pi j A}{2\bar{k}} \left[F_+(-\bar{k}) + E(\bar{k}) \right]$$

I hope to be able to use this result to obtain the inverse transforms (15) with one or at most two K_x values. Once the fields in 15 have been obtained, the components H_{xs}, E_{xs} would be obtained by direct applications of Maxwell's equations.

Figure 1: Finite Element Method

ORIGINAL
   EQUATION: $Lf = S$

APPROXIMATE f BY SOME $\tilde{f}: \Rightarrow L\tilde{f} - S = \varepsilon$

LET $\tilde{f} \cong \tilde{F}^e(y,z) = \alpha_1 + \alpha_2 y + \alpha_3 z$

IN TERMS OF NODAL VALUES:

$\tilde{F}_n^e = \alpha_1 + \alpha_2 y_n + \alpha_3 z_n$

$n = i, j, k$

3×3 SYSTEM —
   SOLVE FOR α's
      AND SUBSTITUTE INTO $\tilde{f}$ ABOVE

FINALLY, GET

$\tilde{F}^e(y,z) = N_i^e \tilde{F}_i^e + N_j^e \tilde{F}_j^e + N_k^e F_k$

$N_i^e = \frac{1}{2\Delta}(a_i + b_i y + c_i z)$

$a_i = y_j z_k - y_k z_j$

$b_i = z_j - z_k$

$c_i = y_k - y_j$
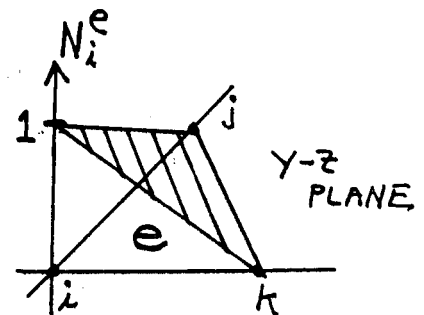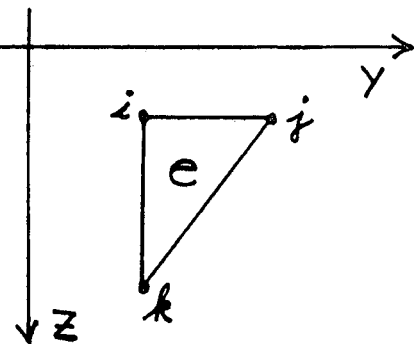
PERMUTE SUBSCRIPTS TO
   OBTAIN N_j^e, N_k^e

Figure 2: Form of the Element--Equations

$$
\begin{bmatrix}
A & \vdots & j\bar{F}_x C \\
\text{SYMMETRIC} & \vdots & \substack{\text{ANTI-}\\ \text{SYMMETRIC}} \\
\text{---} & + & \text{---} \\
j\bar{F}_x C & \vdots & B \\
\substack{\text{ANTI-}\\ \text{SYMMETRIC}} & \vdots & \text{SYMMETRIC}
\end{bmatrix}
\begin{bmatrix}
H_{x_i} \\ H_{x_j} \\ H_{x_k} \\ \hline E_{x_i} \\ E_{x_j} \\ E_{x_k}
\end{bmatrix}
=
\begin{bmatrix}
S_1 \\ S_2 \\ S_3 \\ \hline S_4 \\ S_5 \\ S_6
\end{bmatrix}
$$

IF $\bar{F}_x = 0$ THEN

$$[A]H = S_H \qquad GIVES \quad TM \; mode \; MT$$

$$[B]E = S_E \qquad GIVES \quad TE \; mode \; MT$$

$\bar{C}$ IS OF FORM $\begin{bmatrix} 0 & A & B \\ -A & 0 & C \\ -B & -C & 0 \end{bmatrix}$

Figure 2--continued

$$A = \frac{jw\eta\Delta[\bar{K}_x^2 - K^2]}{12}\begin{bmatrix} 2 & 1 & 1 \\ 1 & 2 & 1 \\ 1 & 1 & 2 \end{bmatrix} - \frac{jw\eta}{4\Delta}\begin{bmatrix} b_i^2+c_i^2 & b_ib_j+c_ic_j & b_ib_k+c_ic_k \\ \text{SYMMETRIC} & b_j^2+c_j^2 & b_jb_k+c_jc_k \\ & & b_k^2+c_k^2 \end{bmatrix}$$

$$B = \frac{-\hat{y}\Delta[\bar{K}_x^2 - K^2]}{12}\begin{bmatrix} 2 & 1 & 1 \\ 1 & 2 & 1 \\ 1 & 1 & 2 \end{bmatrix} + \frac{\hat{y}}{4\Delta}\begin{bmatrix} b_i^2+c_i^2 & b_ib_j+c_ic_j & b_ib_k+c_ic_k \\ \text{SYMMETRIC} & b_j^2+c_j^2 & b_jb_k+c_jc_k \\ & & b_k^2+c_k^2 \end{bmatrix}$$

$$C = \begin{bmatrix} 0 & c_ib_j-b_ic_j & c_ib_k-b_ic_k \\ \text{ANTI-SYMMETRIC} & 0 & c_jb_k-b_jc_k \\ & & 0 \end{bmatrix}$$

$$\begin{bmatrix} S_1 \\ S_2 \\ S_3 \end{bmatrix} = \frac{jw\eta\mathcal{G}_s}{6}\begin{bmatrix} b_i\sum_n E_{Pzn} - c_i\sum_n E_{Pyn} \\ b_j\sum_n E_{Pzn} - c_j\sum_n E_{Pyn} \\ b_k\sum_n E_{Pzn} - c_k\sum_n E_{Pyn} \end{bmatrix}$$

$$\begin{bmatrix} S_4 \\ S_5 \\ S_6 \end{bmatrix} = \frac{-j\bar{K}_x\mathcal{G}_s}{6}\begin{bmatrix} c_i\sum_n E_{Pzn} + b_i\sum_n E_{Pyn} \\ c_j\sum_n E_{Pzn} + b_j\sum_n E_{Pyn} \\ c_k\sum_n E_{Pzn} + b_k\sum_n E_{Pyn} \end{bmatrix} + \frac{\mathcal{G}_s\Delta[\bar{K}_x^2 - K^2]}{12}\begin{bmatrix} 2 & 1 & 1 \\ 1 & 2 & 1 \\ 1 & 1 & 2 \end{bmatrix}\begin{bmatrix} E_{xPi} \\ E_{xPj} \\ E_{xPk} \end{bmatrix}$$

ELECTROMAGNETIC SCATTERING BY TWO-DIMENSIONAL INHOMOGENEITIES

K. H. Lee
University of California
Berkeley

A numerical solution for electromagnetic scattering by two-dimensional inhomogeneities has been developed. The system is excited by a magnetic dipole oriented in the direction perpendicular to the strike, Figure 1.

The theoretical basis is variational principle. A two-dimensional version of variational integral has been developed by transforming out the strike, y, directional dependence. Using finite element technique, the secondary electric field has been obtained in harmonic space. The final solution can be derived by performing inverse Fourier transformation.

It can be shown (Stratton, 1941) that the variational integral I, the total electromagnetic energy contained in a volume V surrounded by S, is written as

$$I(\bar{E}, \bar{H}) = \int_V \left(\frac{\mu}{2} \bar{H}^2 + \frac{\epsilon}{2} \bar{E}^2 + \frac{\sigma}{2j\omega} \bar{E}^2 + \mu \bar{H} \cdot \bar{M}_s + \frac{1}{j\omega} \bar{E} \cdot \bar{J}_s \right) dv \qquad (1)$$

where $\bar{M}_s$ and $\bar{J}_s$ are a magnetic dipole moment and a source current density respectively. The equation can be rewritten in terms of $\bar{H}$ alone or of $\bar{E}$ alone depending upon the type of solution desired. Mainly due to the numerical problem (Pridmore, 1978) encountered at the air-to-earth interface associated with the magnetic field solution, I have chosen the variational integral expressed in terms of electric field;

$$I(\bar{E}) = \int_V \left[\frac{k^2}{2\omega^2 \mu} \bar{E}^2 - \frac{1}{2\omega^2 \mu} (\nabla \times \bar{E})^2 + \frac{1}{j\omega} \bar{E} \cdot \bar{J}_s \right] dv \qquad (2)$$

where

$$\bar{J}_s = \nabla \times \bar{M}_s \qquad (3)$$

and

$$k^2 = \omega^2 \mu \epsilon - j \sigma \omega \mu. \qquad (4)$$

Following variational principle, it can be shown that the station-

ary condition imposed upon the total energy $I(\bar{E})$ results in the following vector wave equation in $\bar{E}$.

$$k^2\bar{E} - \nabla \times \nabla \times \bar{E} = j\omega\mu\,\bar{J}_s. \qquad (5)$$

In order to eliminate the strike directional dependence from $I(\bar{E})$, $\bar{E}$ and $\bar{J}$ have been approximated by Fourier cosine and sine series expansions;

$$P(x,y,z) \doteq \frac{1}{L} \sum_{i=0}^{N} P(x,\eta_i,z)\cos\eta_i y \qquad (6)$$

$$Q(x,y,z) \doteq \frac{j}{L} \sum_{i=0}^{N} Q(x,\eta_i,z)\sin\eta_i y \qquad (7)$$

where $\eta_i = \frac{\pi i}{L}$. The distance L should be long enough to justify our assumption that the half space is two-dimensional. Substituting (6) and (7) into (2) and integrating in y over L, we obtain

$$I\left\{\bar{E}(x,y,z)\right\} \doteq I_0\left\{\bar{E}(x,o,z)\right\} + \sum_{i=1}^{N} I_i\left\{\bar{E}(x,\eta_i,z)\right\} \qquad (8)$$

where

$$I_i\left\{\bar{E}(x,\eta_i,z)\right\} = \frac{1}{L}\int_s \left[\frac{k^2}{2\omega^2\mu}\left(-E_x^2 + E_y^2 - E_z^2\right) \right.$$

$$- \frac{1}{2\omega^2\mu}\left\{\left(j\eta_i E_z - \frac{\partial E_y}{\partial z}\right)^2 - \left(\frac{\partial E_x}{\partial z} - \frac{\partial E_z}{\partial z}\right)^2 + \left(\frac{\partial E_y}{\partial x} - j\eta_i E_x\right)^2\right\}$$

$$\left. + \frac{1}{j\omega}\left(-E_x J_x + E_y J_y - E_z J_z\right)\right]\,dx\,dz. \qquad (9)$$

The last equation is the two-dimensional version of variational integral written for $k_y = \eta_i$.

A numerical representation for equation (9) has been formulated using finite element technique. The electric field has been separated into the primary field, a free space dipolar field, and the secondary field, so that the direct source $\bar{J}_s$ could be eliminated in the formulation process.

The entire cross section, xz plane, is composed of a number of rectangular cells within each of which a bilinear field beha-

viour has been forced.

$$f = a + bx + cy + dxy \qquad (10)$$

Upon substituting equation (10) into the variational integral and integrating over the rectangular area, we obtain a (12 X 12) elementary matrix equation. The total system matrix equation can finally be constructed by simply stacking up all the elementary matrix equations consecutively. Hence, we have

$$I_i \doteq \frac{1}{2} (E^s)^T [K] (E^s) + (E^s)^T (B) \qquad (11)$$

where (E^s) is the unknown secondary electric fields at every nodal points and $[K]$ is a sparsely banded symmetric matrix. The source vector (B) is composed of the prescribed secondary electric fields at the boundary and the terms basically proportional to the primary fields multiplied by the <u>anomalous conductivities</u>.

Taking variations of equation (11) with respect to the unknown secondary electric fields, we obtain a set of simultaneous equations from which the desired solution can be found by

$$(E^s) = - [K]^{-1} (B) . \qquad (12)$$

The associated magnetic fields have been obtained numerically using Maxwell's equation. A bicubic spline fit has been used for the interpolations of the secondary electric fields.

Since our solution has been in k_y harmonic space, we must inversely Fourier transform the solution into the real space domain. After properly interpolated in k_y, the harmonic solutions have been transformed by Fourier integral. The total field solution can be found by superposing analytically calculated primary field.

A few computer modeling for simple models has been done using CDC 7600 at Lawrence Berkeley Laboratory. Figure 2 shows an internal consistency of the solution developed here. The model is a 100 ohm-meter half space with a vertical magnetic dipole located at 2 meters above the ground. The frequency of the transmitting dipole moment is 25 kilocycles/sec. The apparent radial symmetry of the horizontal secondary electric fields can be observed. A maximum of 5 % difference in magnitude can be seen between the two Cartesian

components, E_y and $-E_x$, measured along the two horizontal axes, x
and y.   Another test run has been made to insure the reciprocity
of the opposite source-receiver configurations for the same model.
This time the source frequency is 100 cycles/sec and the location
of the source is on the surface of the earth.   In the vicinity of
source two solutions differ by a maximum of 10 % in magnitude.
However, the phases of the two solutions show a considerable amo-
unt of discrepancies mostly confined within the range of a half of
skin depth from the source.   The difference obviously has been or-
iginated from the unstable solution obtained in the presence of a
horizontal magnetic dipole especially when the source is close to
or on the air-to-earth interface.   The vertical electric field at
the interface seems to have played a major role in causing the in-
stability.

The last model shown here is a half space composed of two qu-
arter spaces; one with resistivity of 100 ohm-meters and the other
of 10 ohm-meters.   An array consists of a vertical magnetic dipole
of unit moment and a receiver separated by 200 meters is moving al-
ong the surface in the direction perpendicular to the contact.
The magnitudes and the phases of E_y, H_x, and H_z versus the array
center have been plotted in Figure 5, Figure 6, and Figure 7 res-
pectively.   The frequency used has been 100 cycles/sec.   The most
dramatic change in magnitude across the contact has been observed
in H_x with an increase of one order of magnitude.   All three com-
ponents show more or less similar transient phase changes across
the contact.   It should be noticed that no anomalous response can
be observed in the ranges towards both boundaries starting from a-
pproximately a half of skin depth away from the contact.

Acknowledgements

$$\bar{M}_s = M_x \bar{I}_x + M_z \bar{I}_z$$
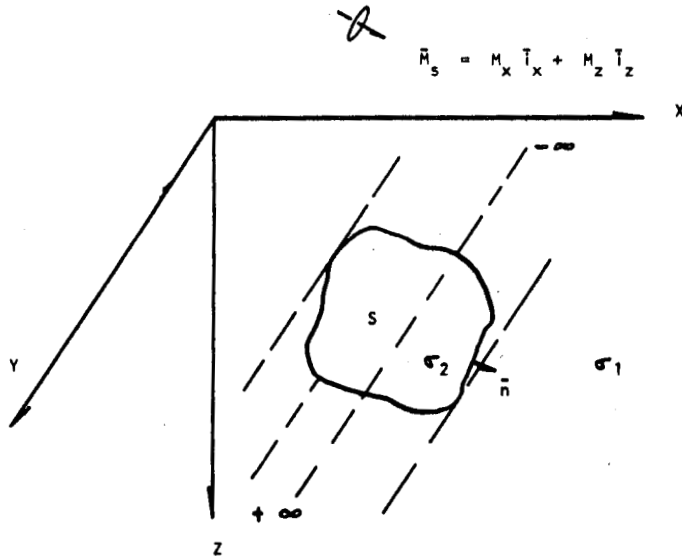
Figure 1. A geophysical system.
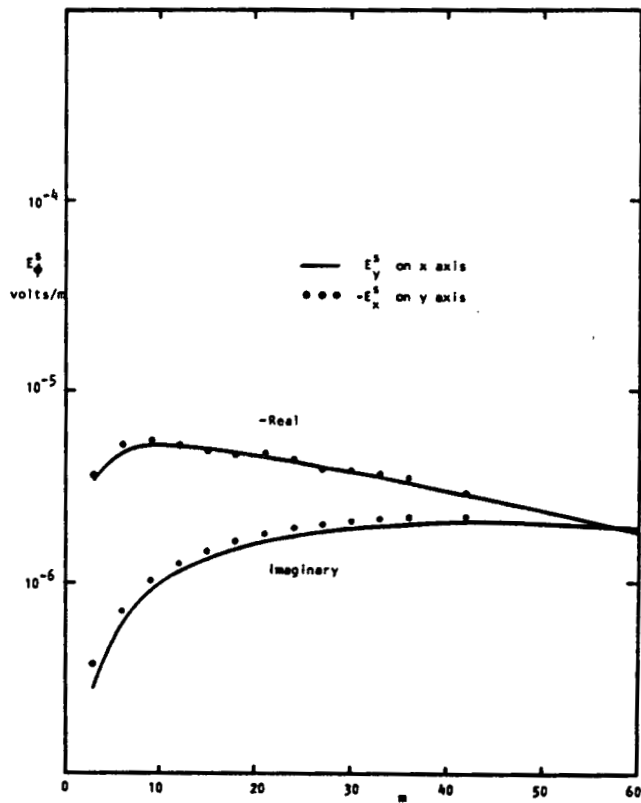
Figure 2.   Symmetry of horizontal electric fields.
Frequency = 25 kilocycles/sec
Half space resistivity = 100 ohm-meters
Source; A vertical magnetic dipole of
unit moment located at 2 meters above
the ground
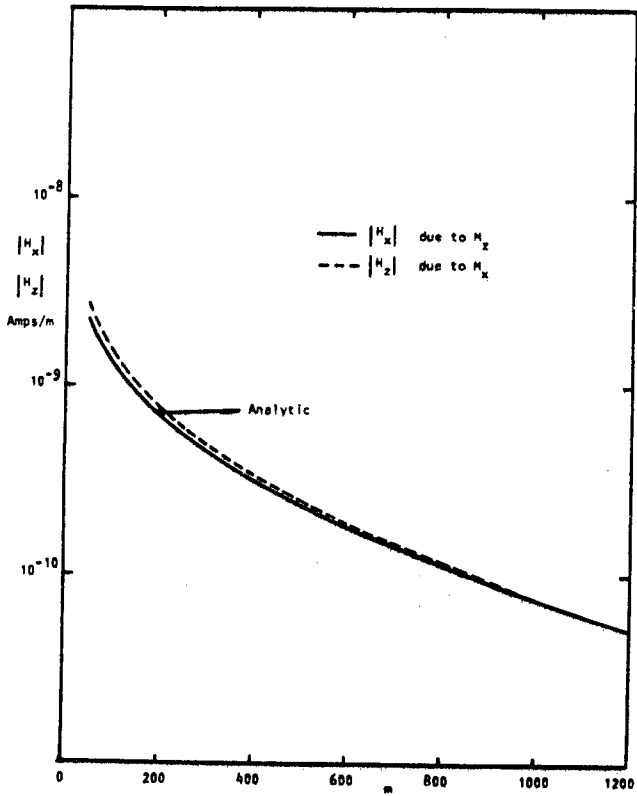
Figure 3.

Reciprocity in magnitude.
Frequency = 100 cycles/sec
Half space resistivity = 100 ohm-meters
Source; M_z and M_x located on the surface
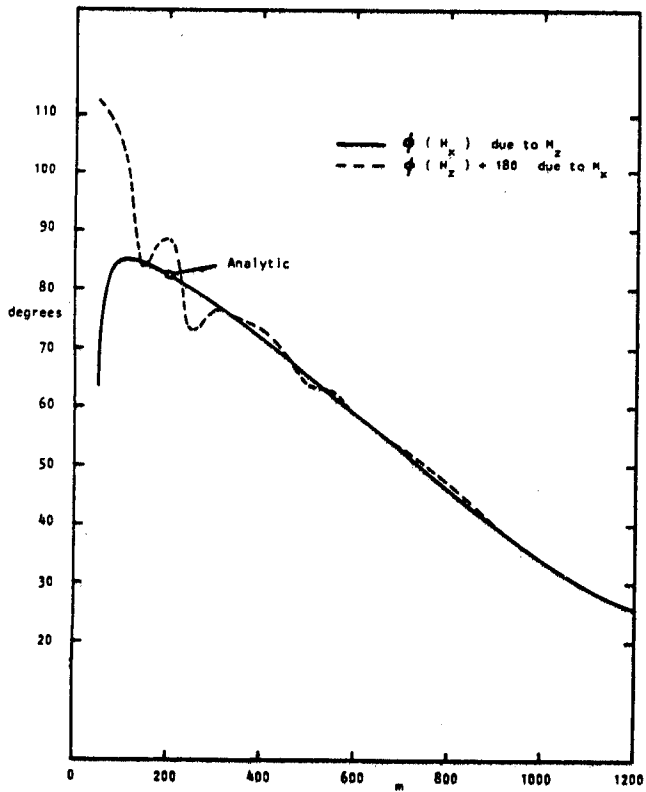
Figure 4.   Reciprocity in phase.
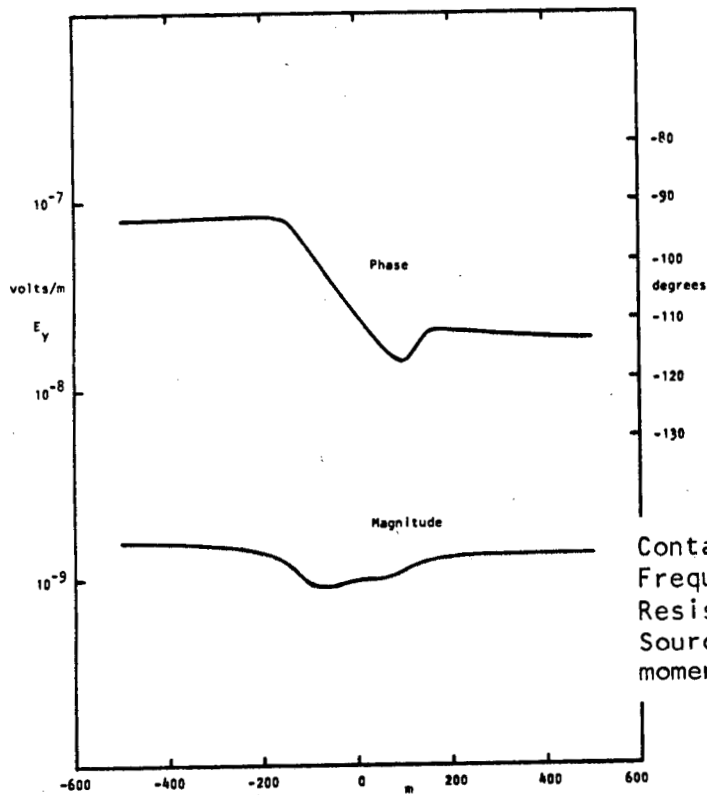
Figure 5.

Contact response on E_y.
Frequency = 100 cycles/sec
Resistivities of quarter spaces; 100 and 10
Source; A vertical magnetic dipole of unit moment

Figure 7.

Contact response on H_z.

Long tick marks on both axes indicate analytic solutions.

Figure 6.   Contact response on H_x.

Long tick marks on both axes indicate analytic solutions.

3D FINITE ELEMENT MODELING OF ELECTRIC AND ELECTROMAGNETIC DATA

D. Pridmore
Engineering Geoscience
University of California
Berkeley, California 94720

Introduction

A finite element code was written to solve three dimensional resistivity and electromagnetic problems. In both cases, the minimum theorem (Stakgold, 1968, p. 338) was used to give a variational statement. Results from this code were in satisfactory agreement with those obtained from Hohmann's 3D integral equation algorithm (Hohmann, 1977, personal communication) for resistivity modeling, and for electromagnetic modeling where the conductivity contrasts between the body and the half space were less than two orders of magnitude. The details of the finite element technique and the comparison between the different results are given by Pridmore (1978).

The finite element is well suited for the modeling of earths with a complex distribution of conductivity, although the flexibility of the method is achieved at the price of significant computational effort. Since many realistic earths are characterized by complex distributions of conductivity the method definitely deserved further attention. The purpose of this contribution is to outline the problems encountered in the work by Pridmore (1978) and to offer some general suggestions for future endeavors. The important problem of implementing a three dimensional finite element code on presently available computer hardware is not addressed.

Long, Thin Elements

The most severe problems encountered were the loss of accuracy and increase in computer time caused by long, thin elements in the mesh. A typical mesh is illustrated in Fig. 1. The fundamental unit was chosen to be a brick--either a single hexahedral element, or a brick assembled from tetrahedral elements. The corresponding interpolating functions were tri-linear and linear respectively. It may be seen from Fig. 1 that long thin elements are found where a mesh contains both large and small spacings between the nodes. Small spacings are needed around inhomogeneities where the field variation is rapid, and large spacings are desirable near the edges of the mesh to minimize the total number of nodes.

The presence of a significant number of long thin elements, with their very poor interpolating properties, degrades the accuracy of the result throughout the entire region, and increases the spectral radius of the associted iteration matrix causing an iterative solution to the system of equations to converge less quickly and, in some cases, to diverge. However, a mesh assembled in the fashion illustrated in Fig. 1 has the following advantages: a) it is easy to define the mesh and conductivity distribution to the finite element algorithm; and b) the non-zero elements in the resultant matrix are always in the same columns, relative to the diagonal (see Fig. 2). This means that for an iterative solution it is straightforward to calculate the position of the non-zero entries in the matrix, and for a direct solution the bandwidth of the matrix is constant.

Mesh designs that would alleviate the long, thin element problem include:

a) using more nodes, so that large variations in mesh size can be avoided. Although this treats the symptoms rather than the cause, it may be the most effective solution.

b) using non-conforming elements. Here, continuity of the unknowns across element boundaries is not enforced, violating one of the conditions that guarantees the convergence of a finite element solution (e.g., Zienkiewicz, 1971). However, the solution may still converge. A mesh assembled from non-conforming elements may be easily graded as illustrated in two dimensions in Fig. 3, where each of the rectangular elements is a bi-linear element. There is some evidence to suggest that this scheme does not improve, significantly, the accuracy of the result (Gregory and Whiteman, 1974), although it should improve the convergence of an iterative solution. However, the book keeping for the alternative (a) is easier.

c) grading node density but not element density. Such a mesh, again in 2D, is illustrated in Fig. 4. The outer elements have a different number of nodes on different sides of the element. This assembly has good interpolating properties (Gregory and Whiteman, 1974), and presumably the iteration solution is well behaved. The structure of the resulting matrix is sparse, but quite irregular-- requiring, again, significantly more book keeping than alternative (a).

d) using a hybrid technique in which only the central part of the problem is meshed. Discretization is stopped before the behavior

of the field variables is known, and either Green's functions (W.

Scheen, in this proceedings) or eigen functions (S. Chang, in this

proceedings) are used to get the correct values at the mesh boundary.

Hybrid techniques present a fertile field for research. At the moment

they accommodate the same class of models as do the integral equation

techniques; namely, relatively localized inhomogeneities within a

one-dimensional conductivity distribution. However, accurate solutions

for a large range of simple models are not yet available.

3D Finite Element--Finite Difference

The finite element method, implemented with the mesh shown in

Fig. 1, offers no apparent advantage over the finite difference technique.

The bandwidth of the resultant matrices is almost identical for the

same number of unknowns, and several authors have shown that in simple

one- and two-dimensional problems the accuracies of the techniques

are similar (e.g., Harrington, 1968; Finlayson, 1972; Rijo, 1977).

Finite difference techniques lead to fewer non-zero elements in the

system matrix than does a finite element approximation, and thus require

fewer computations per iteration of an iterative solution. However,

iterative solutions appear to converge more slowly (Dorn, 1978, personal

communication).

Neither the present finite element scheme nor the usual finite

difference method can define a sloping conductivity interface exactly.

Results from D modeling experiments (Rijo, 1977, personal communication)

suggest that, for most applications, the ability to model sloping

interfaces below the earth's surface is not important. Results over

a sloping interface are almost the same whether the interface is defined

exactly by triangular elements, or approximated by a stair-step of rectangular elements, as would be necessary with a finite difference technique. Results are not the same for topographic effects, however, where fewer nodes are required to get an accurate solution with sloping elements, than with the step approximations of a finite difference scheme.

The finite element method has an advantage over finite difference methods for the approximation of topography in three dimensions if isoparametric elements are used (see, for example, Zienkiewicz, 1971 for a description of isoparametric elements). For instance, the 8-node brick element illustrated in Fig. 1, as an isoparametric element, could model sloping interfaces in 3 dimensions.

Very Low Frequency Results

The finite element solution for the electric field problem proceeds by finding a stationary point of the functional:

$$\int_V \nabla \times \underline{E} \cdot \nabla \times E \quad -k^2 \underline{E} \cdot E \quad dv,$$

where E is the electric field, $k^2 = \hat{z}\hat{y}$, $\hat{z} = i\omega\mu$, $\hat{y} = \sigma + i\omega\varepsilon$, ω is the angular frequency, σ is the conductivity, ε is the permittivity, and μ is the permeability. The dimensions of the $\nabla \times \underline{E} \cdot \nabla \times \underline{E}$ term is $\underline{E}^2[L]$ while the dimension of the $k^2 \underline{E} \cdot \underline{E}$ term is $\underline{E}^2 k^2 [L]^3$.

If the earth is discretized an approximately 1/6th of a skin depth, then the curl term is approximately two orders of magnitude larger than the $\underline{E} \cdot \underline{E}$ term. On increasing the density of elements the ratio becomes larger. In the 3D problem it is not sufficient to have

the element size tied to the skin depth of the fields, since surface charges perturb the field behavior irrespective of strict induction phenomena. The problem at very low frequencies may be illustrated by considering a model in which discretization density must be strongly related to charge fields (such as in the static problem). As the frequency is lowered, the contribution of the $\underline{E}\cdot\underline{E}$ term becomes arbitrarily small until it is lost in the roundoff error of the computations. Lajoie and West (1976) believed a similar effect to be a significant source of error in their integral equation solution. However, in the finite element approach, it appears that a roundoff error is not important for frequencies above 0.1 Hz. The contributions from charge terms could be carried explicitly by modifying the differential equation from:

$$\nabla \times \nabla \times \underline{E} - k^2 \underline{E} = 0$$

to

$$-\nabla^2 \underline{E} + \nabla \frac{-\nabla\hat{y} \cdot \underline{E}}{\hat{y}} - k^2 \underline{E} = 0 \quad .$$

Again, the $\nabla\hat{y}$ term requires special attention in the computer code.

REFERENCES

Finlayson, B. A., 1972, The method of weighted residuals and variational principles, New York, Academic Press.

Gregory, J. A., and Whiteman, J. R., Local mesh refinement with finite elements for elliptic problems, Report TR/24, Brunel University, Dept. of Mathematics.

Harrington, R. F., 1968, Field computation by moment methods, New York, MacMillan.

Heubner, K. H., 1975, The finite element method for engineers, New York, Wiley.

Lajoie, J. J., and West, G. F., 1976, The electromagnetic response of a conductive inhomogeneity in a layered earth, Geophysics, v. 41, pp. 1133-1156.

Pridmore, D. F., Three dimensional modeling of electrical and electromagnetic data using the finite element method, Ph.D. Dissertation, University of Utah, 1978.

Rijo, L., Modeling of electric and electromagnetic data, Ph.D. Dissertation, University of Utah, 1977.

Stakgold, I., 1968, Boundary value problems of mathematical physics, Vol. 2, New York, MacMillan.

Zienkiewicz, O. C., 1971, The finite element method in engineering science, New York, McGraw-Hill.

(a) TETRAHEDRAL ELEMENTS

10 x 7 x 6 = 420 NODES

(b) HEXAHEDRAL ELEMENTS
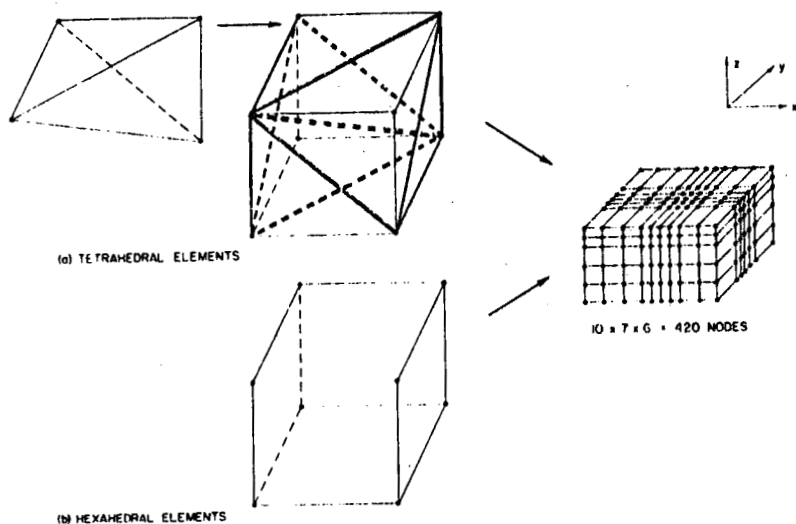
Fig. 1. A three dimensional mesh assembled from a) tetrahedral elements, and b) hexahedral elements.
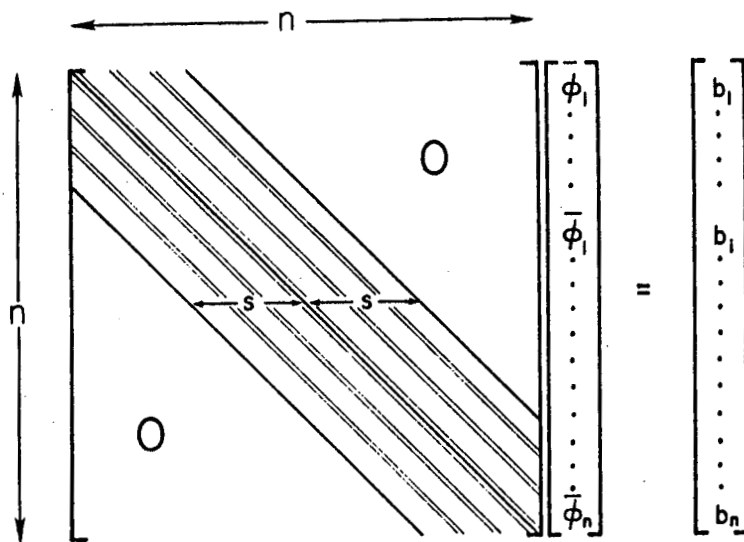
Fig. 2. Schematic structure of the linear system of equations
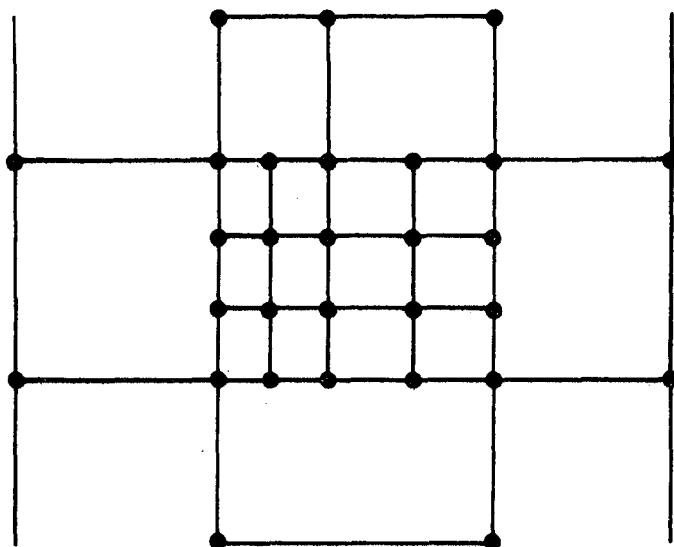
XBL 788-1508

Fig. 3. A mesh constructed from non-conforming elements.
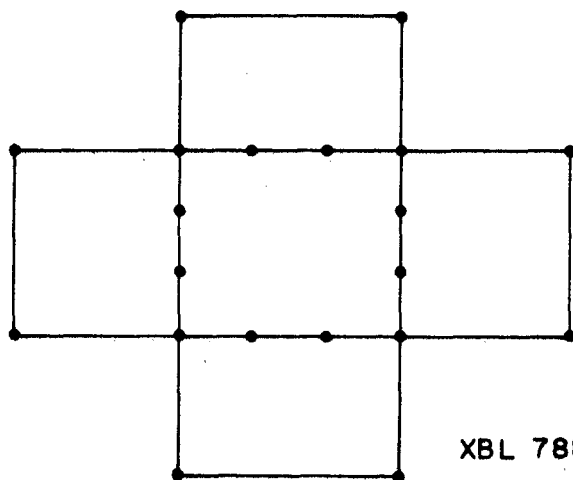
XBL 788-1509

Fig. 4. Mesh grading keeping the number of elements constant.

TRANSIENT TIME DOMAIN ELECTROMAGNETICS*

John T. Kuo and Dong-Heng Cho
Aldridge Laboratory of Applied Geophysics
Henry Krumb School of Mines
Columbia University, New York, New York 10027

With externally impressed electric and magnetic sources, the electric and magnetic field equations may be derived from the symmetrical Maxwell's equations. Two variational principles for the initial boundary value problem of electromagnetics are derived. The first one of the Gurtin type is deduced from the integro-differential equations equivalent to the electromagnetic field equations, while the second one is a simplified version of the first variational principle.

The variational field equations are casted into the form suitable for a finite element formulation in space. An explicit central-differences scheme in time is then applied to the finite element variational equation to yield a recursive relation for time integration.

The results of the Newmont Electromagnetic Pulse (EMP) survey done in the Mutooroo prospect in Australia is numerically verified by a Turam approximation.

INTRODUCTION

Considerable advances have been made in recent years towards the improvement of transient electromagnetic survey for mineral exploration, notably the Newmont Electromagnetic Pulse (EMP) system (see the Newmont EMP System, 1976, presented at the Workshop on Mining Geophysics). For example, the newest Newmont version, Mark VI, is fully digital and has been in production use in Australia since the middle of 1976. It is timely to investigate the transient time domain electromagnetic problem, particularly in three dimensions.

A. Variational Principles for Time-domain Electromagnetics

The numerical scheme we developed is derived from variational principle for electromagnetics which is directly obtained from the field equations derived from the Maxwell's equations.

On the basis of the following differential EM field equations:

$$-\nabla \times \nabla \times \begin{Bmatrix} E \\ H \end{Bmatrix} - \mu\varepsilon \frac{\partial^2}{\partial t^2} \begin{Bmatrix} E \\ H \end{Bmatrix} - \mu\sigma \frac{\partial}{\partial t} \begin{Bmatrix} E \\ H \end{Bmatrix}$$

$$= \begin{cases} \mu \dfrac{\partial J'}{\partial t} + \mu\nabla \times \dfrac{\partial M'}{\partial t} + \nabla \dfrac{\rho'_e}{\varepsilon} \\[4mm] \mu\varepsilon \dfrac{\partial^2 M'}{\partial t^2} + \mu\sigma \dfrac{\partial M'}{\partial t} - \nabla \times J' + \nabla\rho'_m \end{cases} \tag{1}$$

where

$\underset{\sim}{E}$ = electric field (Volt/m)

$\underset{\sim}{H}$ = magnetic field (Ampere-turn/m)

$\underset{\sim}{J}'$ = impressed electric current (Ampere/m^2)

$\underset{\sim}{M}'$ = impressed magnetic dipole moment per unit volume (Ampere-turn/m)

ρ_e' = impressed electrical charge (Coulomb/m^3)

ρ_m' = impressed magnetic charge (Ampere-turn/m^2)

μ = magnetic permeability (Henry/m)

ε = electrical permittivity (Farad/m)

σ = electrical conductivity (mho/m)

and the initial and boundary conditions, we derive the variational integral Λ of the Gurtin type as

$$\Lambda = \int_R \{t * \underset{\sim}{\nabla} \underset{\sim}{F} * \underset{\sim}{\nabla} \underset{\sim}{F} + \varepsilon\mu \underset{\sim}{F} * \underset{\sim}{F}$$

$$+ \sigma\mu \underset{\sim}{F} * \underset{\sim}{F} + 2\underset{\sim}{G} * \underset{\sim}{F}\} dV \tag{2}$$

where

$\underset{\sim}{F} = \underset{\sim}{E}$ or $\underset{\sim}{H}$

$\underset{\sim}{G} = t * \underset{\sim}{Q} - (\varepsilon\mu + \sigma\mu t)\underset{\sim}{F}^O - \sigma\mu t \dot{\underset{\sim}{F}}^O$

$\underset{\sim}{Q}$ = source vector; $\underset{\sim}{Q} = \begin{cases} Q^e \text{ for electric source} \\ Q^m \text{ for magnetic source} \end{cases}$

$\underset{\sim}{F}^O \quad \dot{\underset{\sim}{F}}^O$ = initial conditions: $\dot{\underset{\sim}{F}}^O = \dfrac{\partial \underset{\sim}{F}^O}{\partial t} \Big| \quad t = t_o$

* = the convolution

t = time

Furthermore, introducing $\Lambda = t*\Omega$, we obtain that the new functional Ω is the equivalent variational integral given as,

$$\Omega = \int_R \{\nabla F * \nabla F + \varepsilon\mu F * \frac{\partial^2 F}{\partial t^2}$$

$$+ \sigma\mu F * \frac{\partial F}{\partial t} + 2F * Q\}dV \qquad (3)$$

The initial conditions can now be conveniently incorporated into the formulation. Taking a variation of Ω with respect to the nodal values, we obtain $\delta\Omega = 0$.

B. **The Finite Element Formulation for the Three Dimensional Time-domain Electromagnetics:**

The finite element discretization of the above variation equation yields the corresponding matrix equation,

$$[M]\{\ddot{\phi}\} + [D]\{\dot{\phi}\} + [K]\{\phi\} = \{\ell\} \qquad (4)$$

where

$$[M] = \int_R \varepsilon\mu [N]^T [N] dV \qquad \left(\begin{matrix} \text{Mass} \\ \text{Matrix} \end{matrix}\right)$$

$$[D] = \int_R \sigma\mu [N]^T [N] dV \qquad \left(\begin{matrix} \text{Damping} \\ \text{Matrix} \end{matrix}\right)$$

$$[K] = \int_R \{[N,x]^T [N,x] + [N,y]^T [N,y]$$
$$+ [N,z]^T [N,z]\}dV \qquad \left(\begin{matrix} \text{Stiffness} \\ \text{Matrix} \end{matrix}\right)$$

$$\{\ell\} = -\int_R [N]^T \{Q\} dV \qquad \left(\begin{matrix} \text{Source} \\ \text{Matrix} \end{matrix}\right)$$

[N] = shape function matrix

$\{\phi\}$ $\{\dot\phi\}$ $\{\ddot\phi\}$ = unknown electrical or magnetic field and
its first and second time derivatives at nodes.

The matrix equation (4) is solved at each discrete time step by means of the explicit central differences scheme, avoiding cumbersome inversions of the global stiffness matrix.

C. Numerical Verification of the Newmont Mutooroo Survey

The finite element formulation for the three-dimensional time-domain electromagnetics has been computer coded. The computer program is successfully tested for an excitation of an electrical line source in a conductive, dielectric and permeable wholespace. The source function is assumed to be bell-shaped. The electromagnetic parameters are so chosen to test the sensitivity of each parameter. The numerical solutions to all these test problems are found to be stable.

Figure 1 shows the electric field strength that might be observed at a distance of 50 meters from the source position. In case 1 of the conductive whole-space, the conductivity plays a major role, giving a highly attenuated received signal; the same is true for Case 2 except the

the phase difference. Therefore the magnetic permeability plays essentially as damping as does the conductivity. Undesired undulating noises are introduced in Case 2 at about 0.3 time unit, possibly due to inappropriate finite-element sizes. Case 3 of a medium of common rock shows a markedly different signal, which is less attenuated and the shape of the original signal is fairly well preserved. This is attributed to the dielectric constant. The optimum grid size is a function of the wavelength, therefore, the skin-depth of the highest frequency contained in the spectral density of the original signal; in turn it is a function of the conductivity, permittivity and permeability of the medium.

Up to date, the most important result has been the verification of the Newmont EMP results performed in Australia by a two-dimensional Turam approximation along the line AA' as shown in Figures 2 and 3, which show the geologic and the field configuration and the EMP result of the Newmont Exploration Ltd. The present numerical verification is important in the sense that the Newmont system is perhaps one of the best EMP systems now in existence. In the present verification, the source is fixed and the data are taken along the lines perpendicular to the larger dimension of the rectangular current loop laid on the surface. The physical and geometrical parameters of the finite element model is given in Figure 4 together with the geometrical layout. All the parameters are also given in dimensionless numbers for

a matter of generality. Figure 4 shows the secondary
electric field strength scattered by the overlying layer and
the dike together, calculated at successive time intervals
at the receiving stations located on the surface across
the electrical line source. The positions A and B are the
position of the dike and that of the source, respectively.
Almost immediately after the initiation of the transient
signal, the secondary field due to the overlying layer
reaches the stations near the source. As the time elapses,
it is built up around the source region but splits into two
parts at about 0.6 time unit. The split signals thereafter
tend to migrate away from the source. The signal scattered
by the dike is expected to show up around the region just above
the dike but it is not explicitly seen in Figure 4. In order
to examine the response of the overburden effect, the response
of the electric field strengths due to the overlying layer and
the half space without the dike is calculated as shown in Figure
5. Visually, it is very difficult to distinguish between
the layered medium with the dike of Figure 4 and the layer
medium without the dike of Figure 5. This is because the
signal due to the dike is much smaller than that of the
overburden.

Figure 6 gives the electric field strength scattered
by the dike only, obtained by subtracting the values for
the layered medium with the dike of Figure 4 from the layer

medium without the dike of Figure 5. The anomaly peak occurs above the dike. The arrival of the signal, about 1.1 time unit, is considerably later than that of the over-burden. Therefore it is recognized that the signal due to the dike begins to appear while the overburden effect is migrating away. This remarkable fact indeed confirms the field work results. Our results of Figures 7 and 8 correspond to the result of the Mutooroo EMP Survey of Figure 3, Y and Z components, respectively. The response of the X component is zero for the Turam approximation, in fact, the X component of the Mutooroo EMP result is indeed also small in comparison with the Y and Z components.

In field practice, the response of the electrical field strengths is rarely measured. Substantial information can be derived from the response of the electrical field strength as shown in Figure 6, which possesses a symmetrical response to the dike.
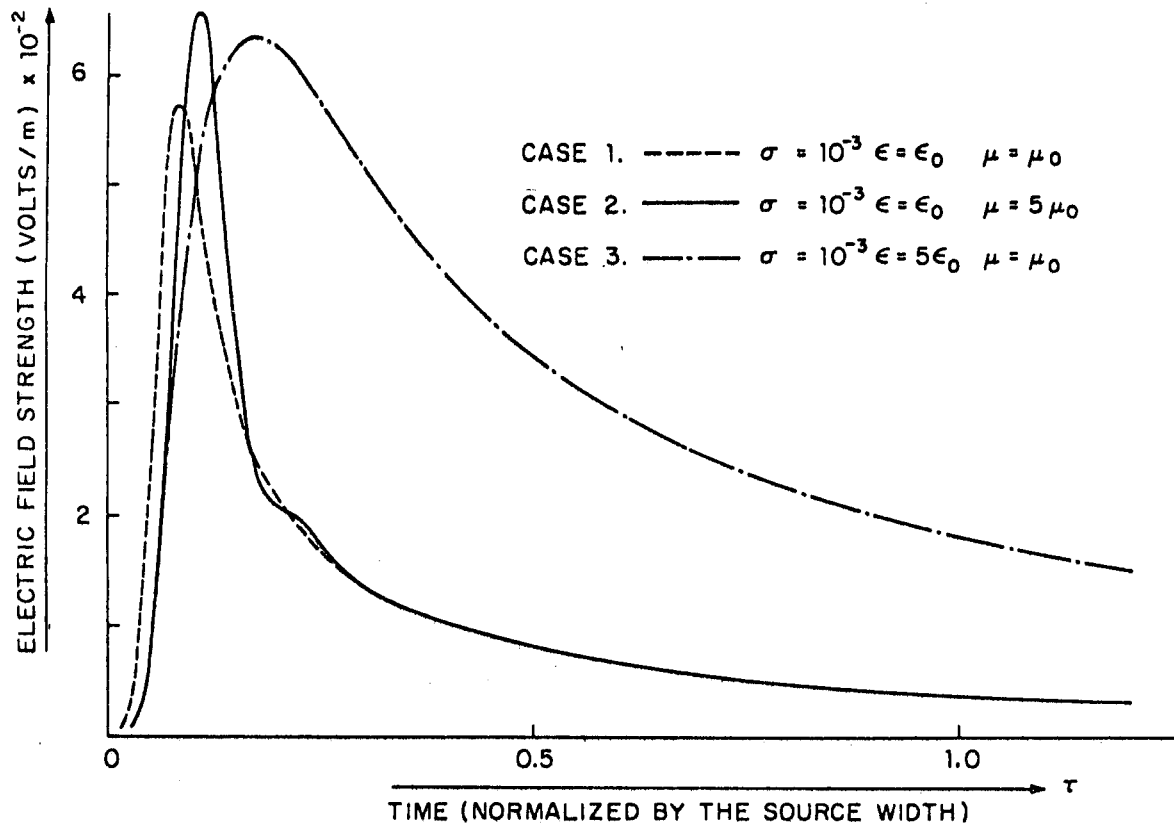
Fig. 1. Electric Field Strengths at a Distance of

50 Meters from the Source.
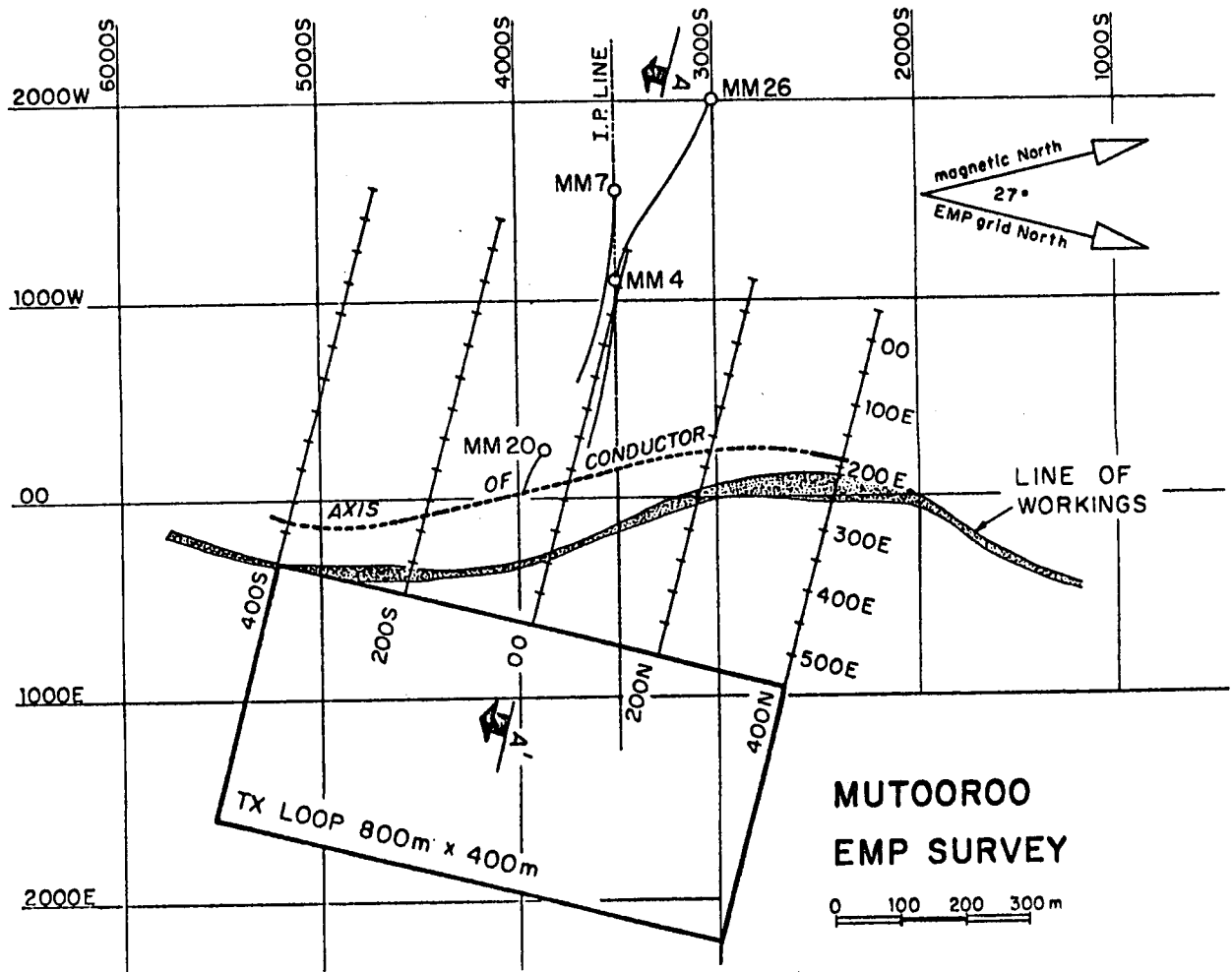
Fig. 2.

The Geological and EMP Setting of the Newmont Mutooroo EMP
(taken from Newmont, 1976)

47
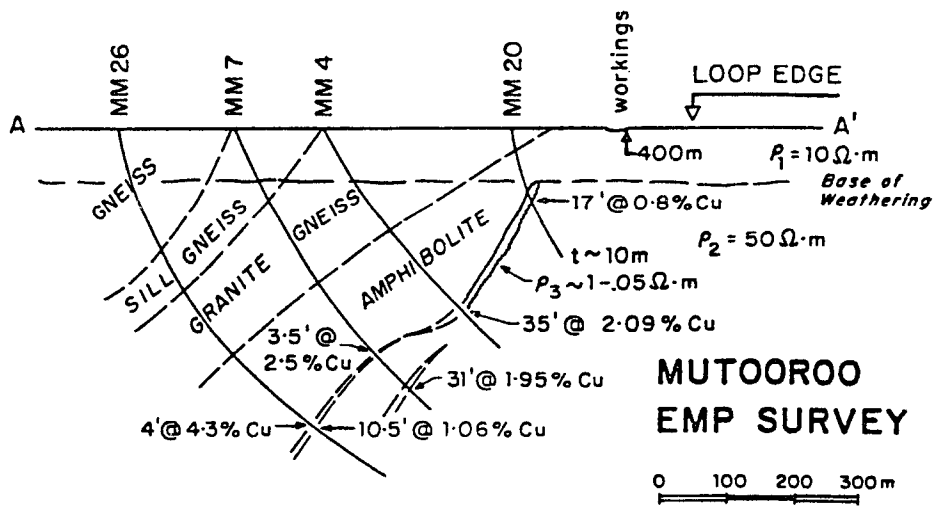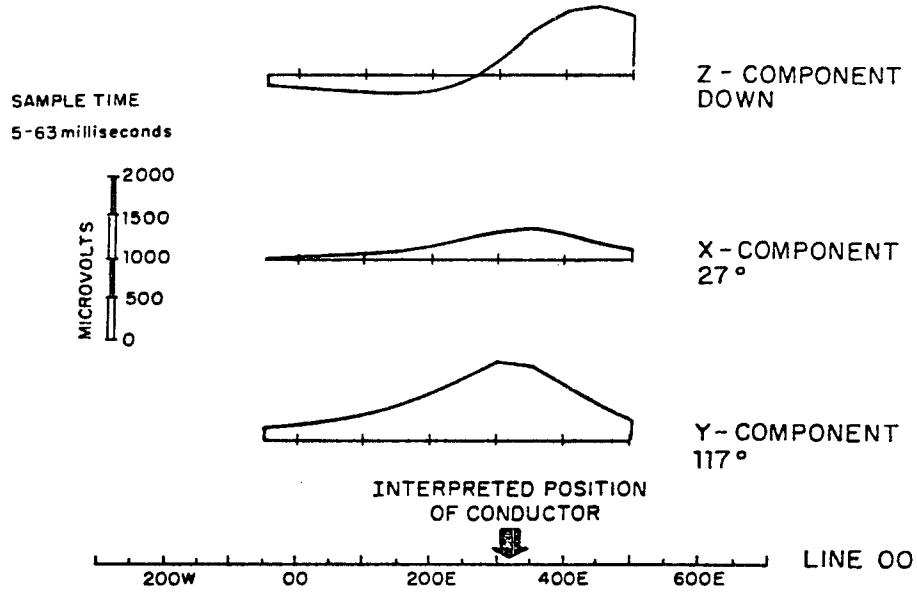
Fig. 3.   Newmont Mutooroo EMP Survey Results
           (taken from Newmont, 1976)
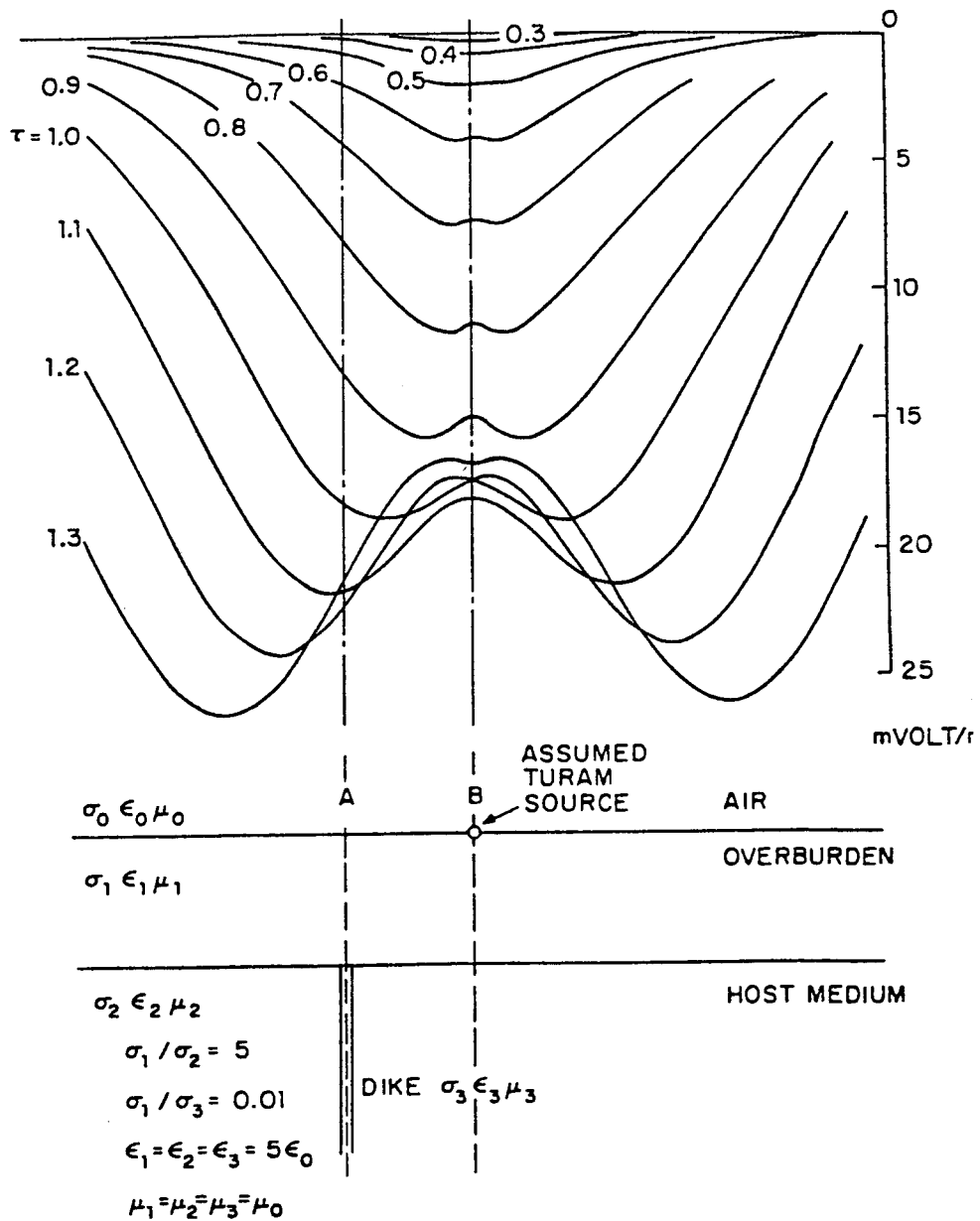
Fig. 4. Electric Field
Strength Anomaly due to
the Overburden and the
Dike.
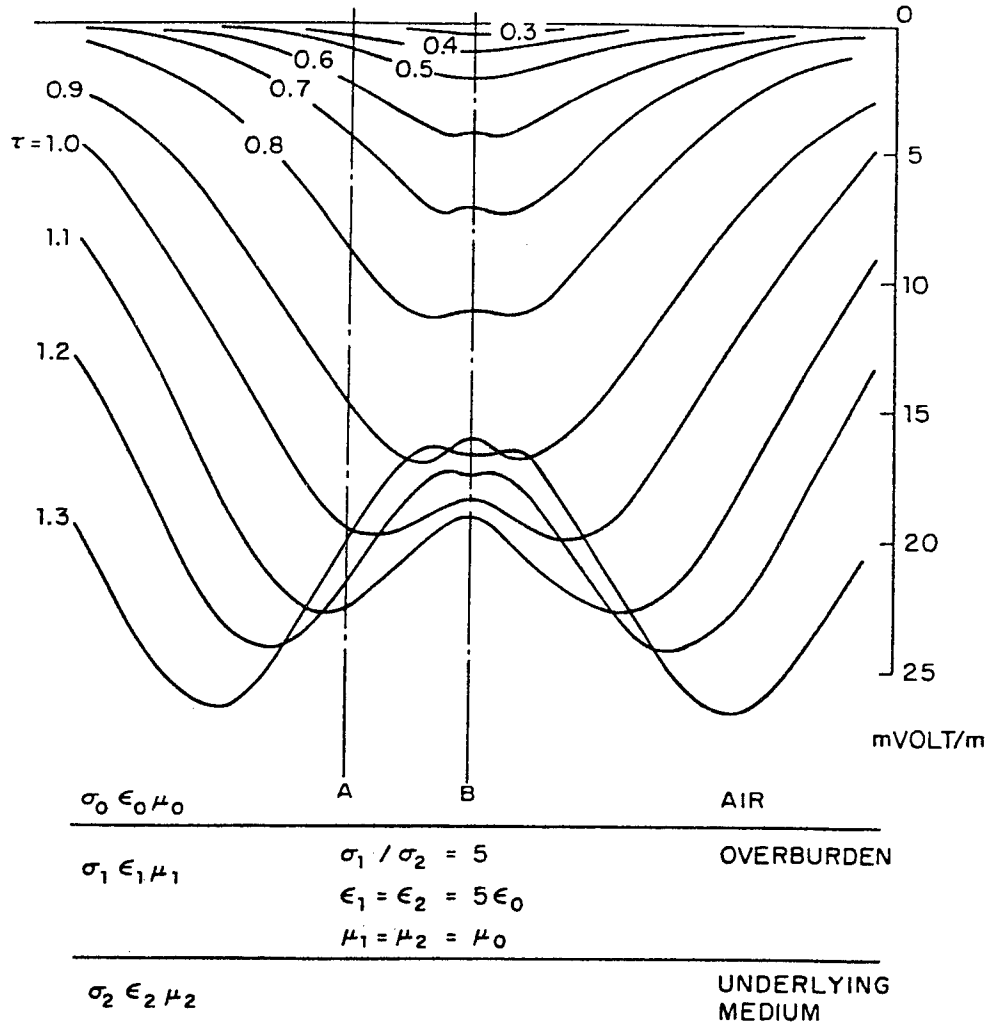
Fig. 5. Electric Field Strength Anomaly due to a layered half-space.
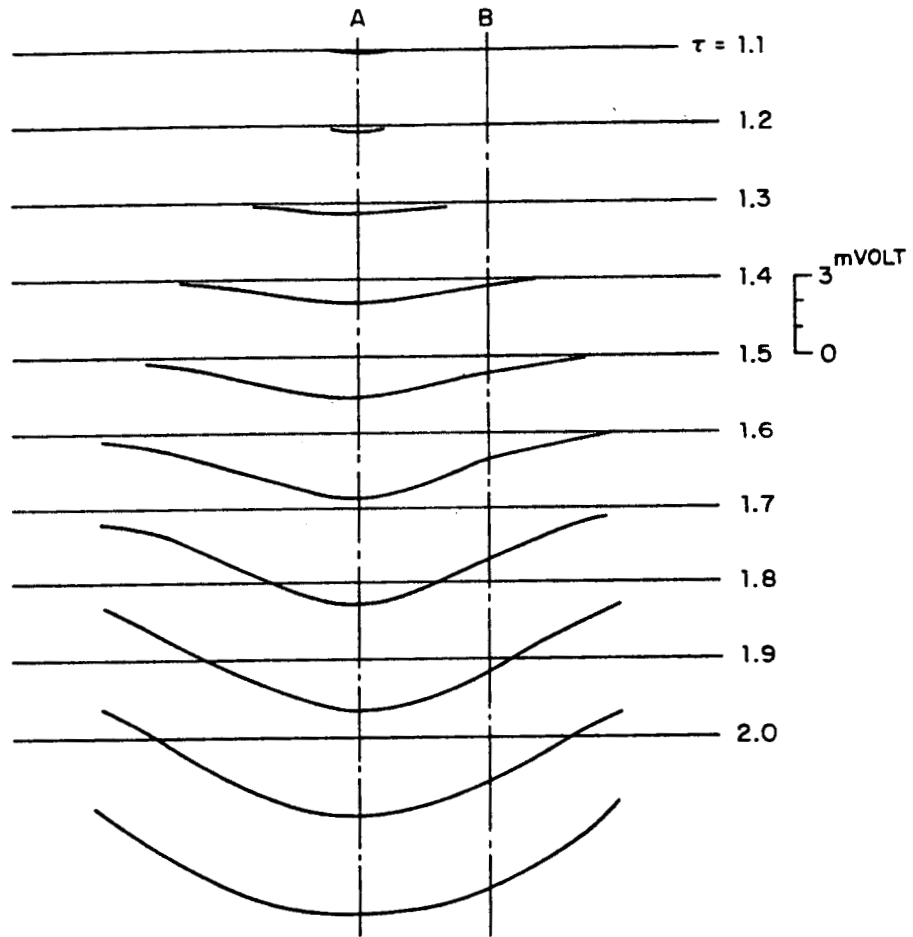
Fig. 6. Electric Field Strength Anomaly due to the Dike
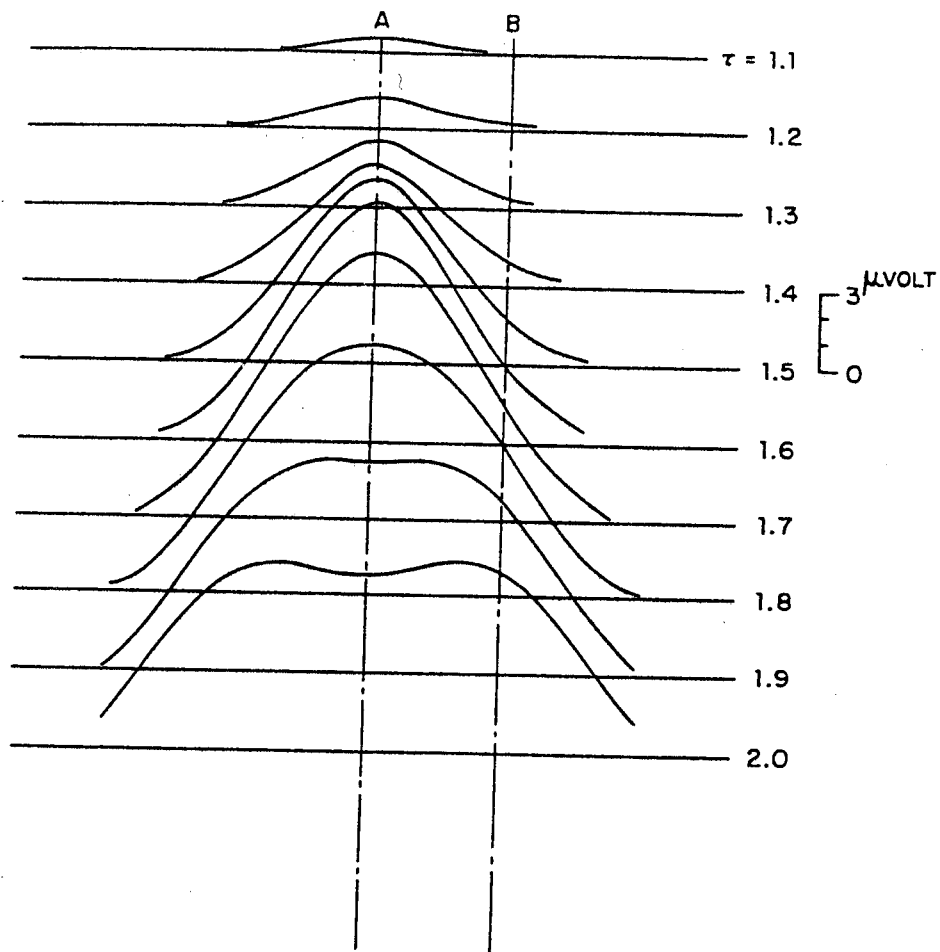
Fig. 7.   Horizontal Magnetic Anomaly due to the Dike.
(Corresponding to Newmont Y-Component).
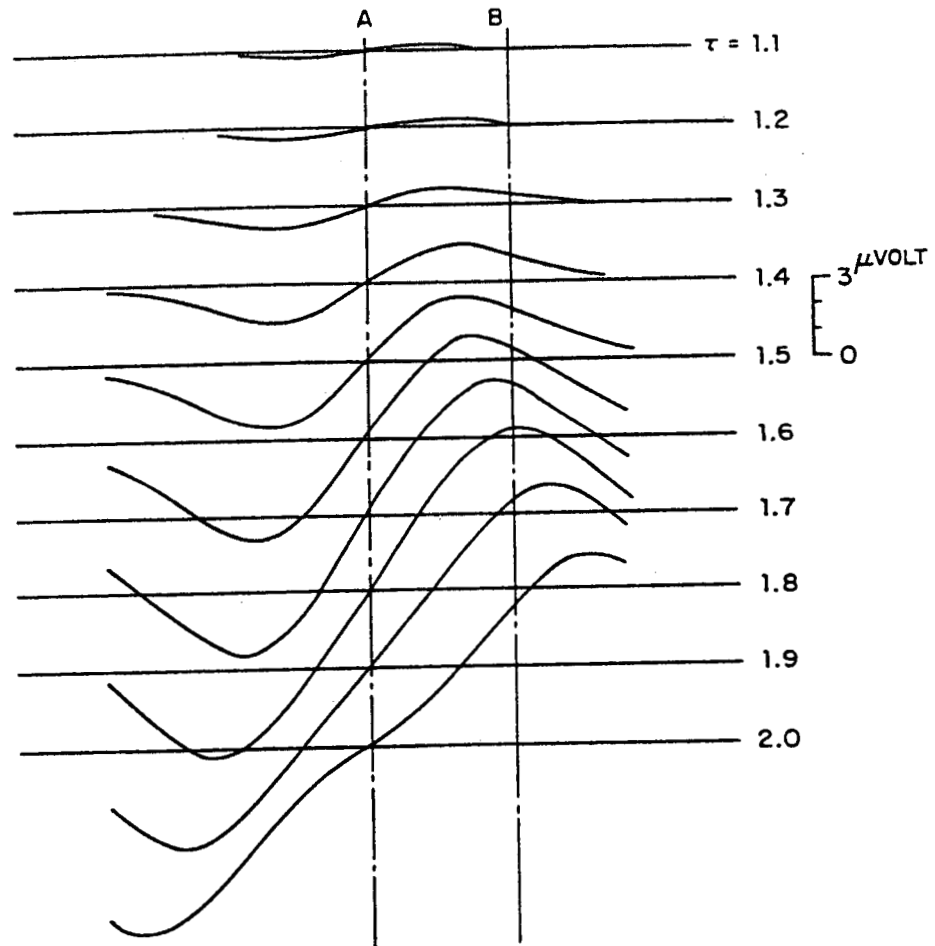
Fig. 8. Vertical Magnetic Field Anomaly due to the Dike.

EMMMMA, A COMPUTER PROGRAM FOR THREE DIMENSIONAL MODELING
OF AIRBORNE ELECTROMAGNETIC SURVEYS

W.L. Scheen

Kon/Shell Exploratie en Produktie Laboratorium

Rijswijk, Holland

Abstract

EMMMMA stands for Electromagnetic Mathematical Model Mixed Algorithm. The program calculates the response observed in airborne dipole-dipole e.m. surveys caused by conductive bodies within a horizontally stratified earth. Working with a certain mesh consisting of tetrahedrons, the program uses a variational principle for setting up a set of finite element equations for the magnetic field. A second set of equations, based in integral relations, expresses the fields at the boundary nodes of the mesh in terms of those at the interior nodes. The same integral relation is used to compute the field at the receiver.

Some results with simple models are shown and problems encountered are discussed. Two versions of this program are being tested.

Introduction

EMMMMA is a three-dimensional modeling program. It has been designed to compute the effect of a conductive body (or conductive bodies) on the response measured in an airborne electromagnetic survey. The body is (bodies are) supposed to be embedded in a horizontally stratified earth, consisting of a substratum overlain by at most six horizontal layers. (It would require very little effort to change the maximum of six layers into say twelve or more.)

The type of e.m. survey that can be modeled by EMMMMA is a magnetic dipole-dipole survey. Three different orientations of the dipole axes are taken into account--vertical, horizontal in the flight direction, and horizontal normal to the direction of flight. This means that nine possible combinations of transmitter and receiver orientations are considered.

Conductivity and dielectric constant may be specified for each layer, each conductive body, and the air and the substratum. The magnetic permeability, however, is assumed constant and equal to μ_0 over the whole space.

A mesh consisting of tetrahedrons is generated; it covers the conductive bodies completely. The boundary of this mesh must lie in the regularly layered part of the earth (+ air).

On the basis of the variational principle:[1]

$$\delta \int \left[H_x^2 + H_y^2 + H_z^2 + \frac{1}{2\pi i f \mu_0 \delta x} \left\{ (\delta H_z/\delta y - \delta H_y/\delta z)^2 + (\delta H_x/\delta z - \delta H_z/\delta x)^2 + \right. \right.$$

$$\left. \left. + (\delta H_y/\delta x - \delta H_z/\delta y)^2 \right\} \right] dV = 0 , \tag{1}$$

a set of finite element equations is constructed allowing us to solve for the magnetic field at the interior nodes of the mesh given the field at the boundary nodes. If we know the magnetic field, we can also compute the electric field by the relation:

$$E = \frac{1}{\sigma^x} \left[\nabla \times H \right] . \qquad (2)$$

In eqs. (1) and (2) σ^x stands for $\delta + 2\pi i f \epsilon$.

An integral relation similar to the one used by Hohmann (1975) provides a second set of equations:[2]

The magnetic (or electric) field at any point of our space is the same as we would find in the regularly layered earth without the conductive bodies, if to the primary dipole sources secondary current sources were added with a source density equal to

$$\nabla \sigma^* \cdot E_{actual}, \text{ where } \nabla \sigma^* = \sigma^*_{body} - \sigma^*_{regular} . \qquad (3)$$

Here $\nabla \sigma^*$ is the conductivity difference between the conductive bodies and the regularly layered earth, and E_{actual} is the actual electric fields in the conductive bodies, which we can derive from the actual magnetic field, H_{actual}, by

$$E_{actual} = \frac{1}{\sigma^*} \left[\nabla \times H_{actual} \right] . \qquad (4)$$

The required set of equations is obtained from this integral relation by replacing the integrals over the conductive bodies by products of the corresponding Greens functions, and expressions of the type (3) by sums of the contributions of the various tetrahedrons in the mesh.

The same procedure is followed for computing the field at the receiver location.

EMMMMA, First Version

We shall use the following notations:

N_{int} = number of interior nodes in the mesh

N_{bnd} = number of boundary nodes

X_{int} = vector composed of the magnetic field components at the
    interior nodes

X_{bnd} = vector composed of the magnetic field components at the
    boundary nodes

Note that X_{int} has $3 \times N_{int}$ and X_{bnd} has $3 \times N_{bnd}$ complex components.

From the variational principle a set of equations is obtained of the type:

$$AX_{int} + BX_{bnd} = 0 , \qquad (5)$$

where A is a symmetric $(3N_{int}) \times (3N_{int})$ matrix and B is a $(3N_{int}) \times (3N_{bnd})$ matrix.

Both matrices are sparse, i.e., they contain many zeros.

The integral relation gives the second set of equations:

$$X_{bnd} = X_{bnd}^{(0)} + CX_{int} , \qquad (6)$$

where

$X_{bnd}^{(0)}$ = Field at the boundary nodes for a regularly layered earth with
    the primary sources only, and

C is a $(3N_{bnd}) \times (3N_{int})$ matrix.

Finally, we have the equations expressing H_{anom}, the anomalous field at
the receiver in terms of the field in the conductive bodies:

$$H_{anom} = DX_{int} \qquad (7)$$

Method of Solution

1. Compute A,B,C. Also compute matrix D for the various receiver positions.

2. Decompose matrix A by

$$A = LU ,$$

where L is a lower and U is an upper triangular matrix, and compute

$$L^{-1}B \ .$$

This step is carired out by a Gaussian elimination procedure without back substitution and with $(3N_{bnd})$ right hand sides corresponding to the columns of matrix B.

3. Compute X_{int} by carrying out the back substitution, taking $X_{bnd}^{(0)}$ for the value of X_{bnd}.

4. Compute new X_{bnd} by eq. (6), using the X_{int} just found in the right hand side of these equations. Update X_{int} with this new X_{bnd}, etc. etc., until the changes in the solution have become sufficiently small.

5. Compute H_{anom} by eq. (7).

Tests carried out on models involving spheres in empty space, for which numerical values acquired by an analytical algorithm were available,[3] showed that the accuracy was poor when the transmitter was close to the conductive body. Comparisons with experimental results for models with conductive dykes were still worse, even with large numbers of nodes and CPU-times of 14 hours on a UNIVAC 1106.

Error Estimation

The finite element equations derived from the variational principle (1) provide a basis for solving the vectorial differential equation

$$\nabla \times \left[\frac{1}{\sigma^*} \nabla \times H \right] = -2\pi i \mu f H \ . \tag{8}$$

When we consider a limited part of space, the differential equation has a unique solution in that part, provided the tangential components of H are given at the boundary (or, alternatively the tangential components of E or, even more general, tangential components of H on one part and tangential components of E on the other part of the boundary).

The above statement is valid as long as $f \neq 0$. If on the contrary $f = 0$,

we have to satisfy the additional equation

$$\nabla(\mu H) = 0 \ . \tag{9}$$

Equation (9) follows from eq. (8) if $f \neq 0$, but it offers an additional condition when $f = 0$. If we do not impose this condition in this case, any gradient field with non-zero divergence, having zero value at the boundary, can be added to the solution without invalidating it.

In our numerical method it means that for low frequencies, i.e., when the important parts of the mesh lie in the nearby field, the set of equations becomes unstable. This leads to the superimposition of a spurious gradient field on top of the desired solution.

This has little effect on the electric field

$$E = \frac{1}{\sigma^*} \left[\nabla x H \right] \ ,$$

as the gradient field is removed by the ∇x operator.

Thus it looks as though everything is all right, because from the finite element solutions only the electric field E is used for the final computation of the field at the receiver location.

To inspect the situation in more detail, mathematical investigations were carried out regarding convergence properties in the proper Sobolew space. They lead to a result that can be summarized as follows:

For the finite element approach the errors ε_H and ε_E in H and E at low frequencies are of the orders

$$\varepsilon_H^2 \approx c_1^2 / f$$
$$\varepsilon_E^2 \approx c_2^2 \quad , \tag{10}$$

where C_1 and C_2 are geometry-dependent (a.o., they decrease with decreasing mesh-width) and do not vanish when $f \to 0$.

This confirms our previous opinion that though the error in H increases

out of proportion when $f \to 0$, the error in E remains reasonable.

However, we are considering <u>magnetic</u> dipole sources, and therefore E will tend to zero when $f \to 0$. Thus we see that the relative error in E will be very big, if f is small.

What has just been said about the error estimates still holds true when we consider the F.E.M. solution of the differential equation

$$\nabla \times \left[\frac{1}{\sigma^*} \nabla \times H \right] = -2\pi i f \mu (H + M_s) \tag{11}$$

with smoothly distributed sources M_s in the area covered by the mesh.

The factors C_1 and C_2 that we obtain in these cases are more or less proportional to H; i.e., if H is small on the whole, C_1 and C_2 will also be small.

This now offers us the following way out of our problem:

Introduce

$$H^{stat} = \text{the field for zero frequency.}$$

Since μ does not vary, H^{stat} is simply the field of a dipole in homogeneous space.

We have $\left[\nabla \times H^{stat} \right] = 0$. $\tag{12}$

Further, we define $\Delta H = H - H^{stat}$. $\tag{13}$

Then $\Delta H = 0(f)$ for $f \to 0$. $\tag{14}$

Moreover ΔH satisfies the equation

$$\nabla \left[\frac{1}{\sigma^*} \nabla \times \Delta H \right] = -2\pi i f \mu (\Delta H + H^{stat}) . \tag{15}$$

This is eq. (11) with ΔH for H and H^{stat} for M_s.

As H is of the order f, C_1 and C_2 will also be and

$$E = \frac{1}{\sigma^*} \left[\nabla \times H \right] = \frac{1}{\sigma^*} \left[\nabla \times \Delta H \right] \tag{16}$$

will be approximated with a relative error that remains finite when $f \to 0$.

EMMMMA, Second Version

The second version of EMMMMA applies the stratagem explained at the end of the previous section. It also avoids the iterative algorithm described by steps (3) and (4) of section 2.

The notations in this section are the same as those of section 2, but X_{int} and X_{bnd} now refer to ΔH instead of H itself. X_{int}^{stat} and X_{bnd}^{stat} will be used for the corresponding vectors formed with H^{stat}.

The variational principle now leads to the set of equations

$$AX_{int} + BX_{bnd} + S = 0 , \tag{17}$$

where

$$S = A_2 X_{int}^{stat} + B_2 X_{bnd}^{stat} . \tag{18}$$

A_2 and B_2 are $(3N_{int}) \times (3N_{bnd})$ resp. $(3N_{int}) \times (3N_{bnd})$ matrices. They are part of matrices A and B, in the sense that these matrices can be written as

$$A = A_1/f + A_2$$
$$B = B_1/f + B_2 . \tag{19}$$

In these latter equations A_1, A_2, B_1, B_2 are independent of f.

The integral equations (6) and (7) remain valid, with the same C and D as before.

Method of Solution

0. Compute X_{int}^{stat} and X_{bnd}^{stat} .

1. As in section 2, but also computing S.

2. As in section 2, but also computing $L^{-1}S$.

3. Compute $A^{-1}B$ and $A^{-1}S$ by back substitution.

4. Compute $I + CA^{-1}B$ (I represents the identity matrix) and $X_{bnd}^{(0)} - CA^{-1}S$.

We will then have computed the matrix and right hand sides of the equation

$$(I + CA^{-1}B)X_{bnd} = X_{bnd}^{(0)} - CA^{-1}S \ . \tag{20}$$

that follows from eqs. (17) and (6).

5. Solve eq. (20) by straightforward Gaussian elimination.

6. Compute X_{int} by

$$X_{int} = -A^{-1}BX_{bnd} - A^{-1}S \ . \tag{21}$$

7. Compute H_{anom} by eq. (7).

Testing is in progress; results look promising so far.

Acknowledgment

The author expresses his thanks to Dr. F.J. Jacobs for carrying out the mathematical analysis of the convergence of the F.E.M. procedure.

References

1. Compare Goggon, Geophysics, Vol. 36, 1971.

2. Compare Hohmann, Geophysics, Vol. 40, 1975.

3. Best & Shammas, submitted to Geophysics.

SCALE MODEL OF THE TEM METHOD

B.R. Spies
Macquarie University
Sydney, Australia
on study leave from
The Bureau of Mineral Resources

Abstract

Scale model studies of the TEM method are being conducted at
Macquarie University, Sydney, using an interactive mini-computer for
timing of waveforms, data acquisition and processing.

In order to construct realistic geological models, it is necessary
to simulate host rock, overburden and mineralization. With TEM modelling
it is not possible to scale time by a factor in excess of about 10. For
these reasons the conventional salt or acid tank is not satisfactory,
and other techniques have had to be developed.

Models used in the Macquarie University facility consist of low-
and medium-melting point alloys (typemetal, Wood's metal, etc.) graphite,
and conductive epoxy resins.

The main difficulty experienced with this modelling setup are:

(1) when time is scaled, sampled times need to be known to
     a very high precision. Wide time windows are
     unsatisfactory.

(2) It is difficult to determine the electrical continuity
     between adjacent materials.

Summary of Paper

Scale Model Facility

The scale model facility at Macquarie University consists of a 35 K word Interdata mini-computer which controls the timing and waveform of the transmitted pulse as well as subsequent data collection and processing. A wide-band amplifier provides an interface between the computer and small multi-turn loops used for model studies. Input and output data are fed via the computer to a teletypewriter. Final results are stored on magnetic tape for subsequent plotting. The use of an interactive technique between the computer and operator enables optimum timing and amplifier settings to be easily determined for each model.

A schematic diagram of the computer equipment is given in Figure 1.

Model Materials

Some materials used for constructing models are listed in Table 1. High-conducting materials are used so that models can be kept relatively small. For example a block of typemetal 10 cm thick can simulate a homogeneous halfspace for times up to 5 ms. By consideration of the electromagnetic modelling relation it can be shown that to simulate a halfspace with salt water over the same time range would require a tank 35 m deep.

TABLE 1 MODEL MATERIALS

Material	Conductivity (S/m)
Copper	$3 - 5.5 \times 10^7$
Brass	$1 - 2 \times 10^7$
Aluminium	$1.6 - 3.7 \times 10^7$
Typemetal (M.P. 230°C)	$2 - 4 \times 10^6$
Low-Melt Alloys (M.P. ~ 70°C)	$10^5 - 5 \times 10^6$
Graphite	$0.3 - 2 \times 10^5$
Conductive Epoxy Resins	$10^3 - 10^5$
Sat^d Salt Water	20

Problems of Electrical Continuity

A major consideration in using the above materials for model studies is the problem of electrical continuity between the various materials.

Two metal sheets pushed together will in fact only be touching in a few places, and the lateral electrical conductivity will be greatly different from the bulk conductivity. For this reason materials such as typemetal and Wood's metal are used, since they have a positive coefficient of expansion upon solidification. They therefore form a very close bond with other model materials they are in contact with.

Conductive epoxy resins can also be used to join materials. The most conductive resin on the market has a conductivity of 10^5 S/m, and thus forms an ideal interface between graphite and other materials.

Note that the problem of electrical continuity may arise with tank modelling, for example where aluminium is used as the one model. Resistive oxides of aluminium on the surface of the model can have a large effect on the modelled response.

Amplifier Requirements

The major problem in designing an amplifier is the requirement of wide bandwidth and high gain. With small models, gains of up to 100,000 are desirable. The effect of a band-limited amplifier on the shape of an exponential decaying waveform can be analysed by the use of the Laplace Transform. It can be shown that for a low-pass filter with a single real pole, the requirement for a 1% error is:

$$\omega_0 \tau = 100$$

where ω_0 is the 3 db point, and

            τ is the time constant of the exponential decay.

For example, if it is desired to measure a transient with a time constant of 0.1 ms the 3 db point of the amplifier would need to be at 150 kHz.

The amplifier used in the Macquarie University facility has a variable gain of 10, 100, 1000, 10000 and a 3 db point of 500 kHz.

Errors in Measurement

In addition to errors introduced by a frequency-limited amplifier, there are also errors introduced from other sources. These are particularly troublesome for conditions of early times, large conductivity, and large loop size. For example, a 1% error in the measured voltage or sample time could cause a 40% error in apparent conductivity. At later sample times the error is greatly reduced.

Model Results - TEM One-loop Configuration

It will be assumed that the reader has a basic knowledge of the TEM method. Descriptions of field equipment, field results and early model stuides are given by Velikin and Bulgakov (1967), Spies (1976 a and b).

2-layered earth response and depth of penetration

Models of a 2-layered earth have been studied with different loop sizes. Results for several cases are shown in Figures 2 and 3. As the thickness of the top layer increases, the departure from the homogeneous ground response of the top layer occurs later in time. The departure time depends on the conductivity and thickness of the layer and the loop size. A feature of the curves is an overshoot effect, which is greatest for thin layers and large loops. This effect is ascribed as being due to interference or resonance effects between layers.

An interesting results is the effect of loop size on depth of penetration. For many years it was assumed that the depth of penetration increased with the size of the loop. However, it can be seen from Figure 4 that at a given sample time, the apparent conductivity derived for the smaller loop is generally closer to the true conductivity of the lower layer, than for the larger loop. Thus, over a 2-layered ground, smaller loops would appear to have a greater depth of penetration than larger loops.

In practice, the depth of penetration is often controlled by the signal/noise ratio and the sensitivity of the TEM instrument. An example of this is given in Figure 5, which shows the TEM response at 1.1 ms of a graphite model of the Woodlawn orebody (New South Wales), as a function of depth of burial. If the noise level is assumed to be proportional to loop area, it can be seen that a larger loop will be able to detect the orebody at a greater depth than with a smaller loop.

Effect of Host Rock

The presence of a conducting host rock was simulated by embedding a copper, and brass, cylinder in typemetal. The resultant transient decay curves (shown in Figure 6) show that at early times the response is due solely to the host rock. In the medium time range the effect of the cylinder is seen, and at very late times the halfspace response again predominates.

Two-loop TEM response of a Homogeneous Ground

In order to examine the response of a homogeneous half-space with a two-loop TEM system a model was constructed out of typemetal. The response of a 1 ohm-m uniform ground with varying loop separations is shown in Figure 7. The curves change sign at a time which depends on their separation and the conductivity of the ground. It can be seen that one-loop response is simply the "late time" assymptote of the two-loop response as the loop-separation goes to zero.

By varying the loop separation, loop size and model conductivity it was possible to empirically derive an expression for the 2-loop homogeneous ground response. This result is shown in Figure 8. Several features of the transient curve are worth noting. Firstly, the fact that the curve changes sign with ground conductivity means that field results of 2-loop data will be much more complex than for the one-loop

configuration. Secondly, for later parts of the transient it can be seen that the response-conductivity relationship is no longer unique. This means that it would be difficult to calculate apparent conductivities.

<u>Future Modelling Work</u>

Model studies are currently being conducted to examine the effect of magnetic permeability and anisotropy on TEM response. It is planned to construct several models of specific field targets with conductive overburden and host rock, with the aim of determining the limits of detectability of various targets.

<u>References</u>

Spies, B.R., 1976a - The transient electromagnetic method in Australia. <u>BMR.Journal of Australian Geology & Geophysics</u>, vol. 1(1), p.23-32.

Spies, B.R., 1976b - The derivation of absolute units in electromagnetic scale modelling. <u>Geophysics</u>, vol. 41(5), p.1042-104

Velikin, A.B., & Bulgakov, Yu. I., 1967 - Transient method of electrical prospecting (one-loop version) : International seminar on geophysical methods of prospecting for ore minerals. Moscow, 1967.

MINI COMPUTER
(Interdata Model 70)

AMPLIFIER UNIT

C.R.O

THERMAL
PRINTER

DAC 1-3

ADC 1

LOOP

(Texas instruments)
700ASR

Schematic diagram of computer equipment

Coil former

Reciever windings (36 B&S)

Transmitter windings (40 B&S)

Diagram of loop windings (cross section)

DAC 1 — Transmitted current pulse

DAC 2 — Receiver amplifier gating pulse

DAC 3 — Amplifier gain

ADC 1 — Digitized samples

0   10   20 ms

Waveforms

Fig. 1.   Scale model facility computer equipment

27 m dia Loop
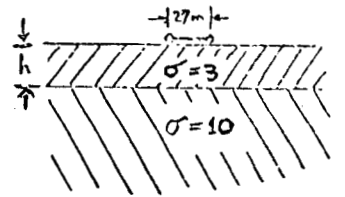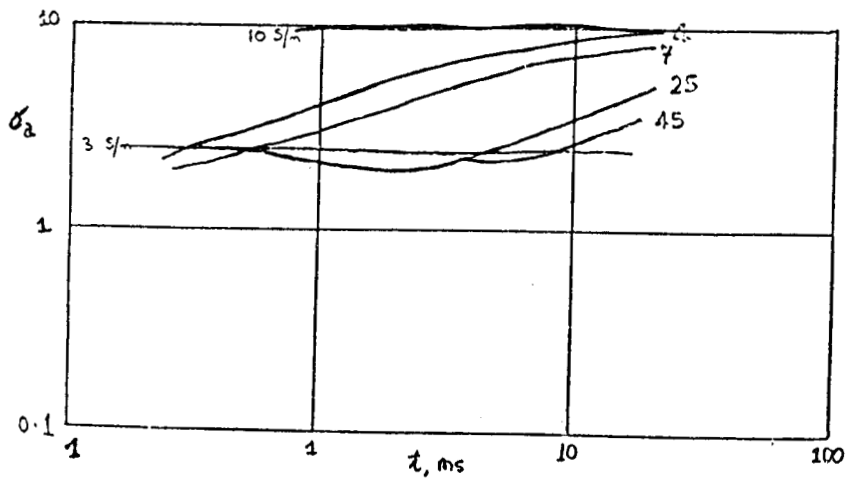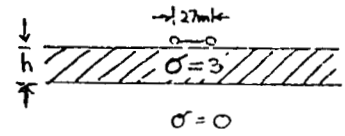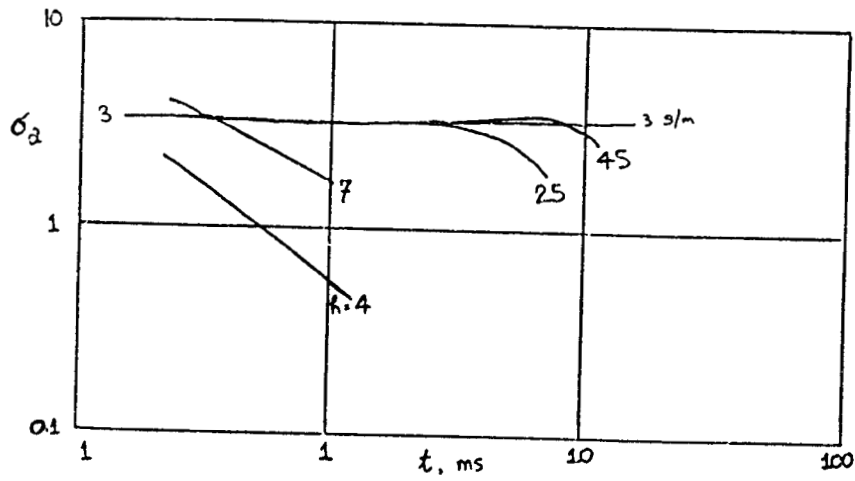
Fig. 2.   One-loop response -- small loop

Fig. 3.   Large loop

CHANGE LOOP SIZE
(18 - 100 m dia.)
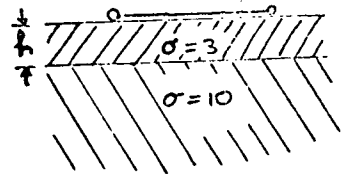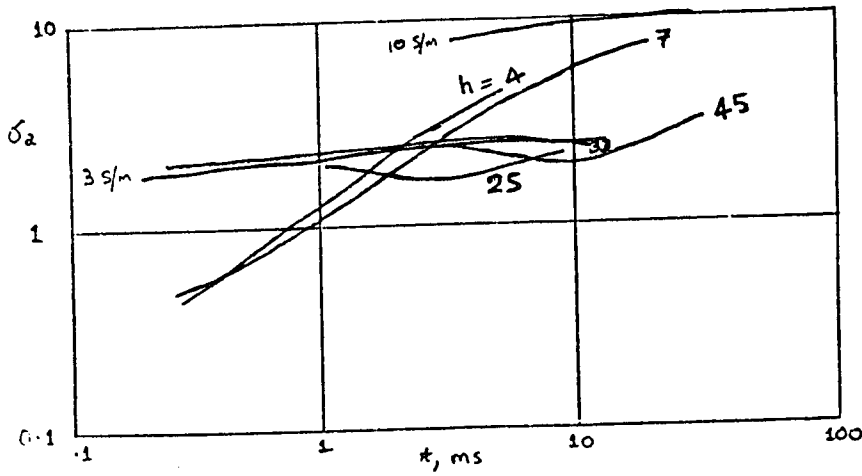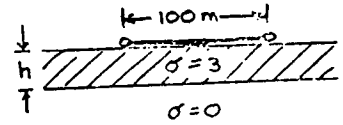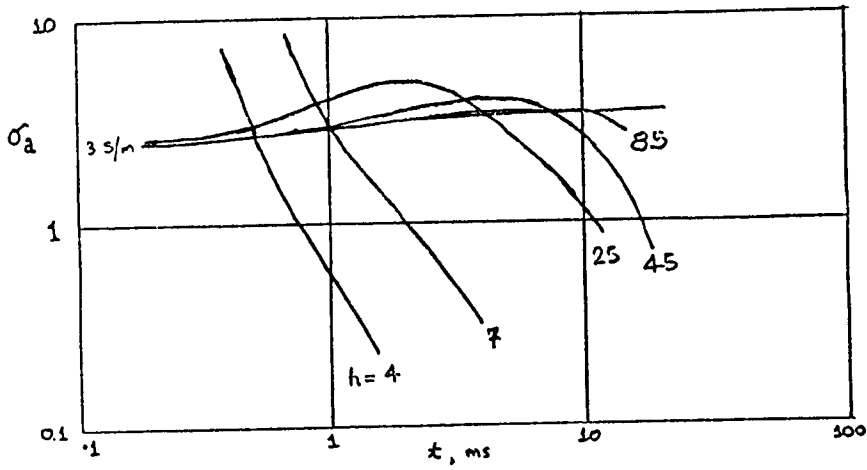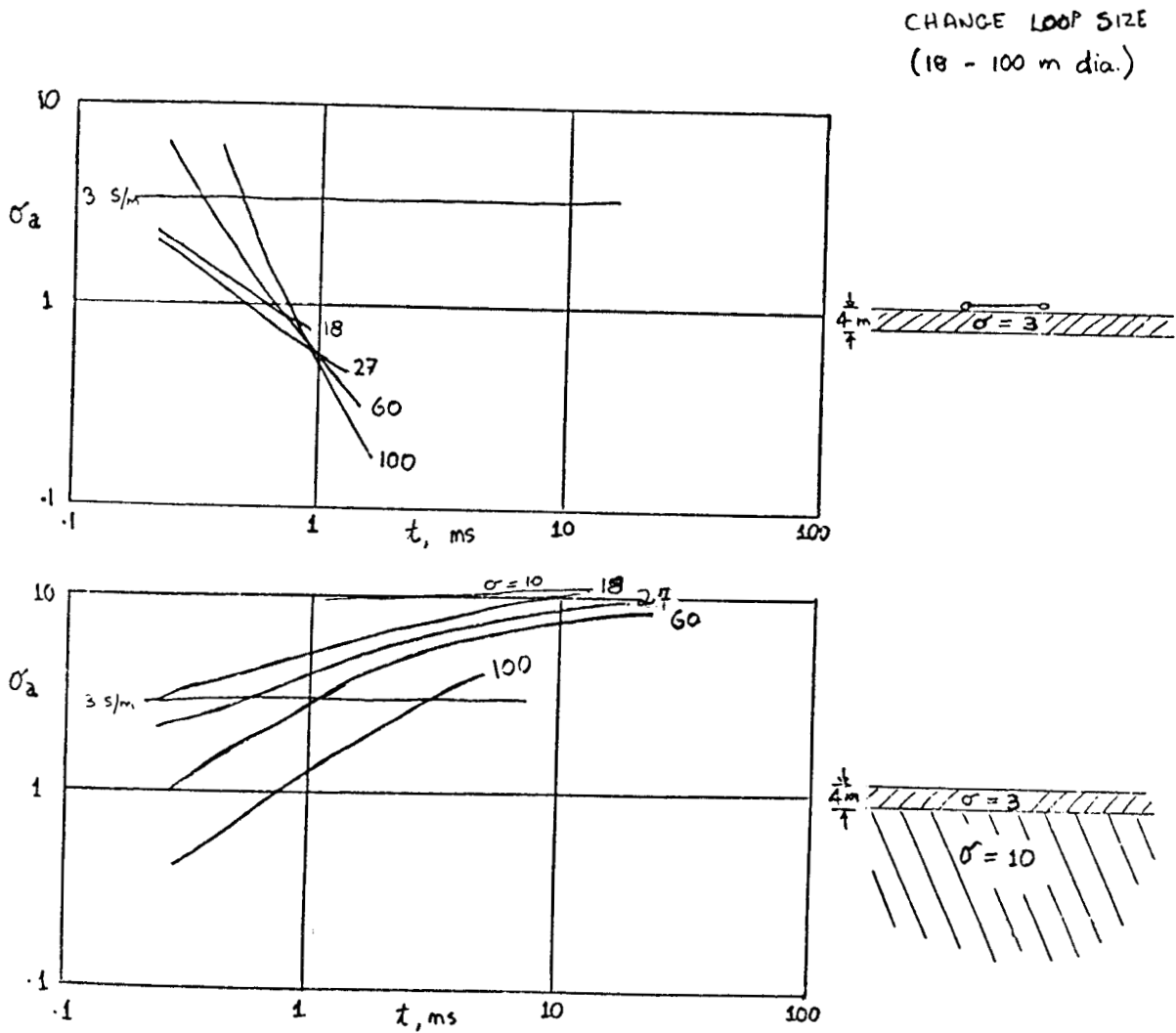
Fig. 4. Conductivity derived for smaller and larger loop at a

given sample time
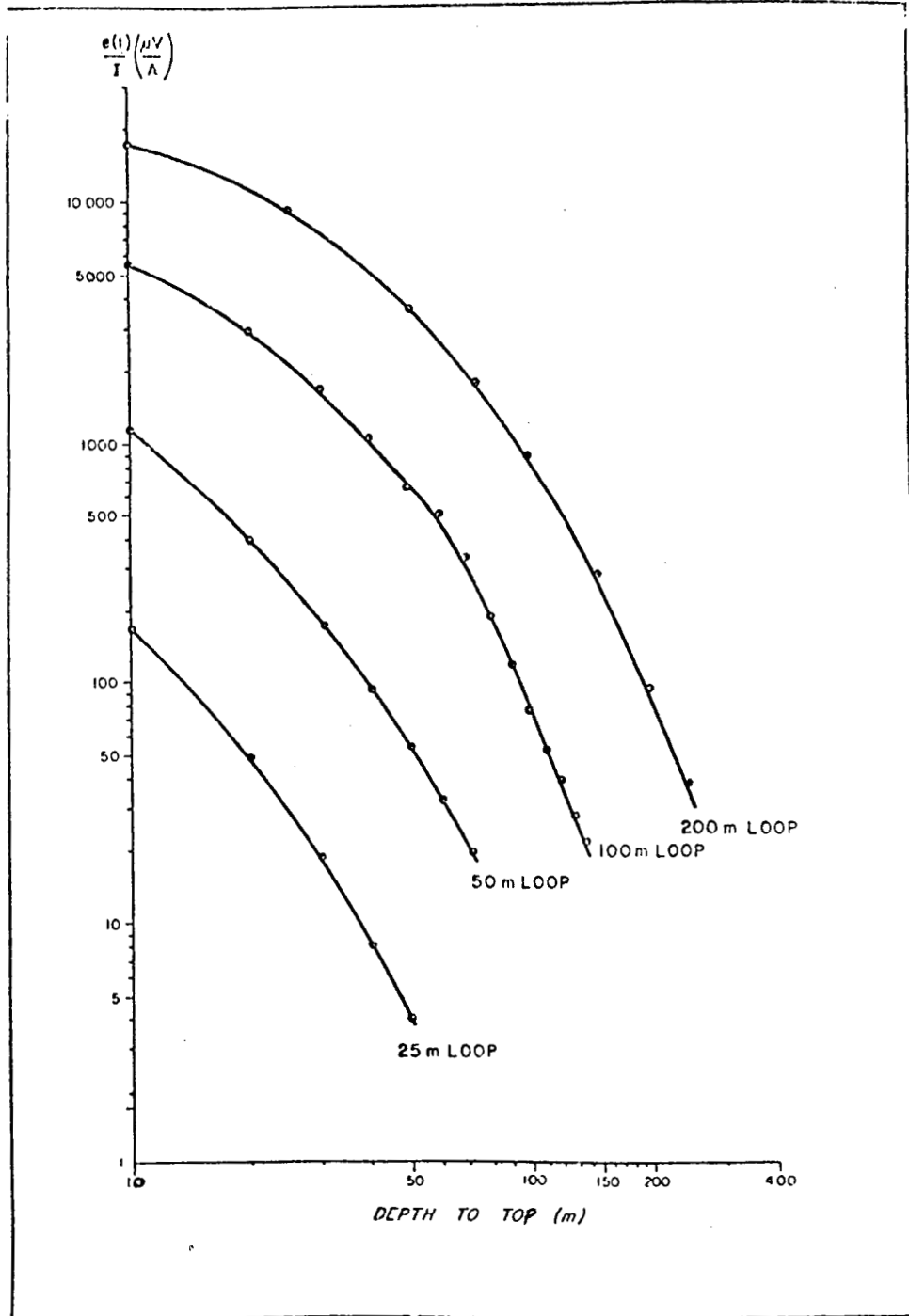
Fig. 5. Woodlawn model: response for different depths of

orebody   t = 1.1ms
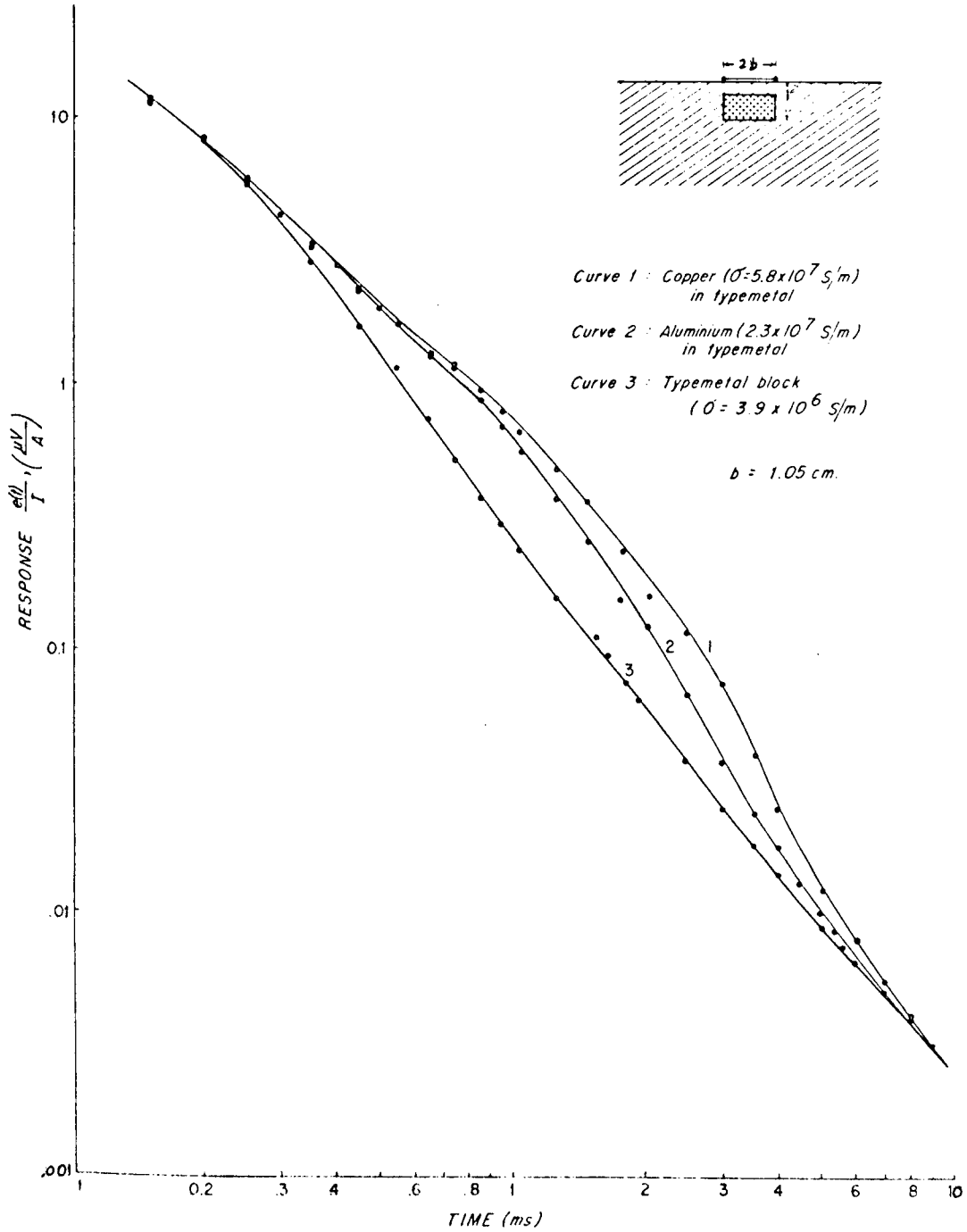
Fig. 6. Decay curves measured over host with and without orebody
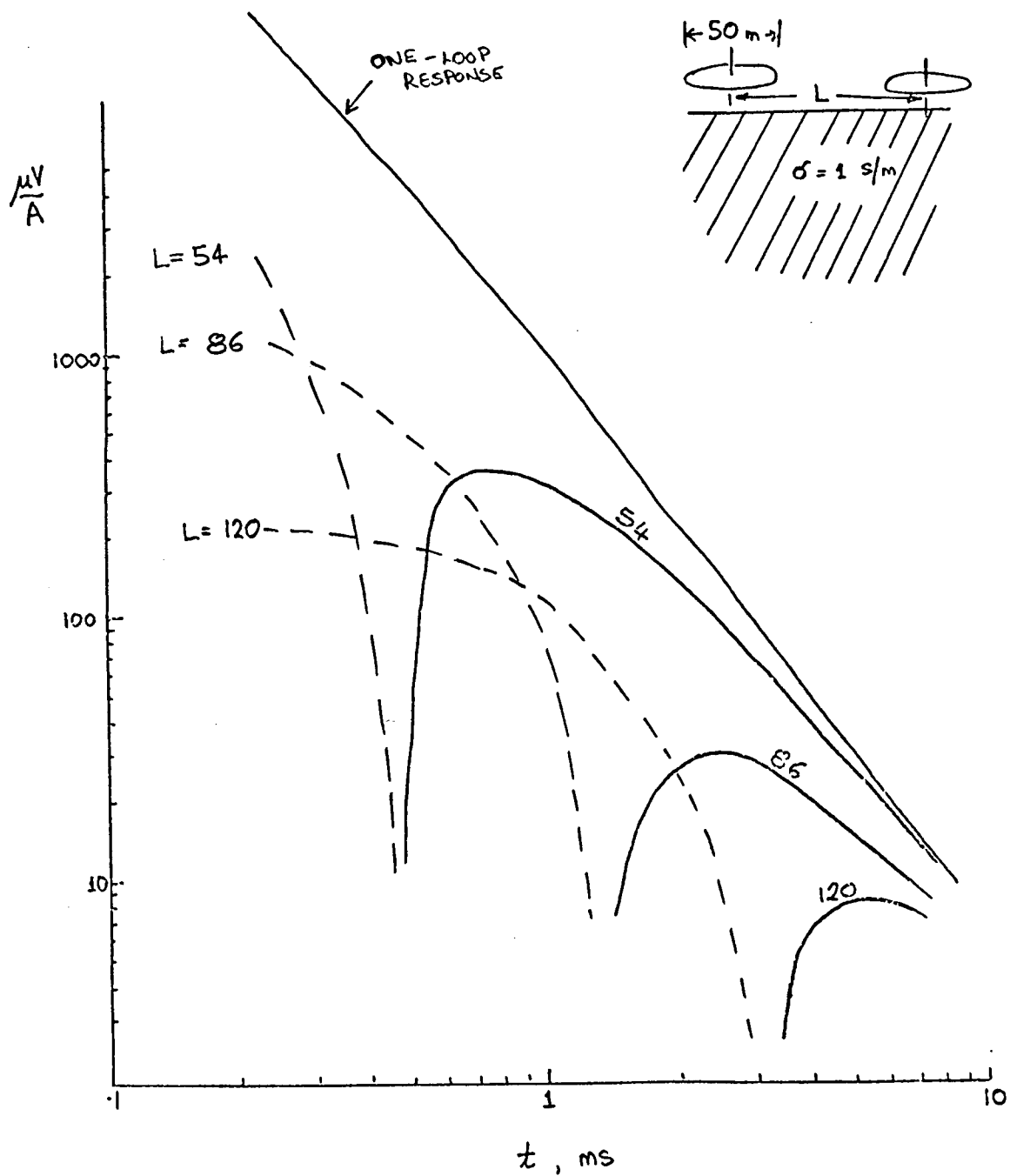
Fig. 7. Response of a 1 ohm-m uniform ground with varying
loop separations

$$\frac{e(t)}{I} \approx \frac{\mu a^4}{t\, d_1^3} \cdot F\left(\frac{\sigma \mu d^2}{t}\right)$$

Fig. 8. Two-loop halfspace response (empirical)
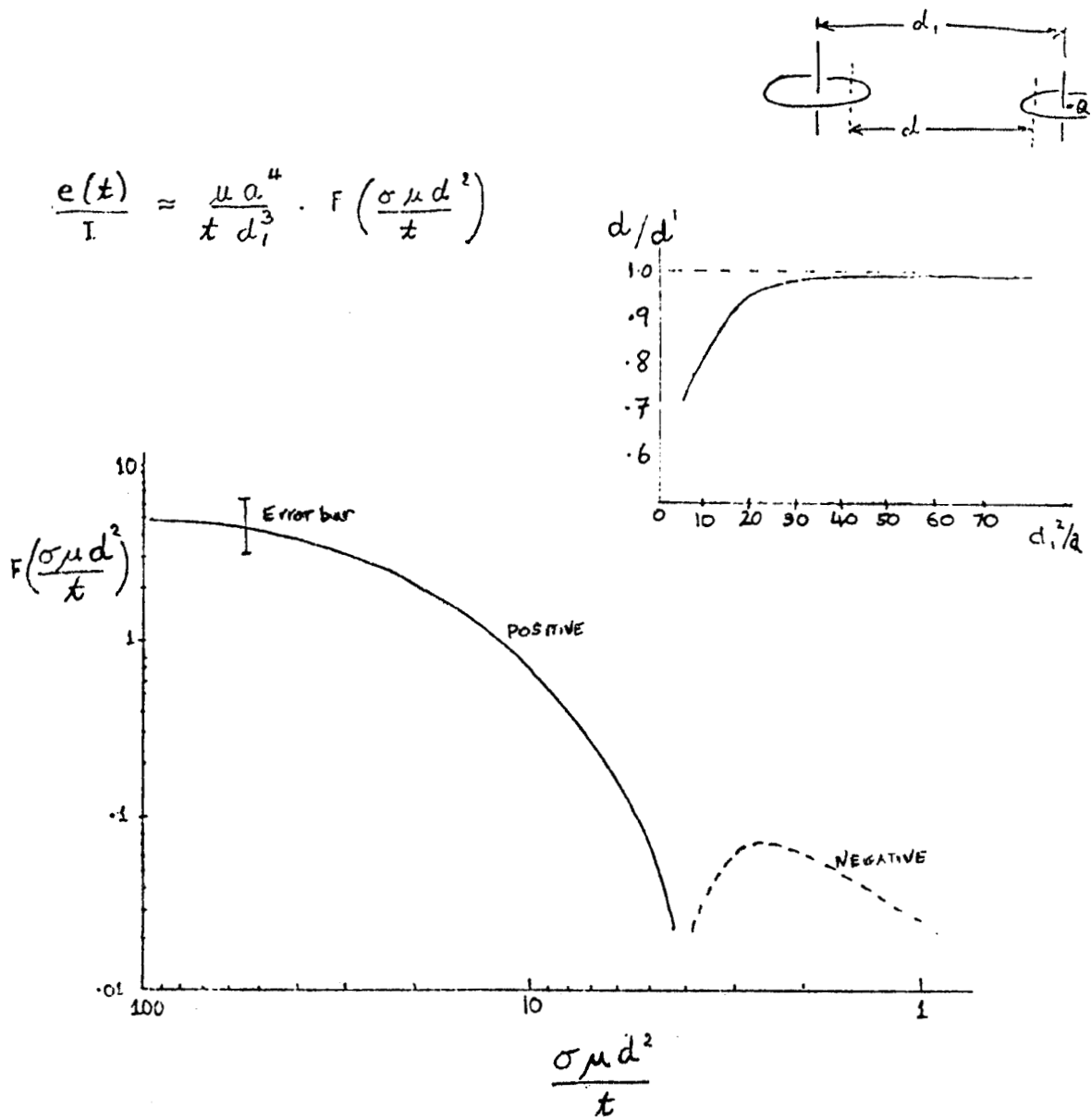
a = Loop radius (m) = square loop side/$\sqrt{\pi}$

$\mu = \mu_0 = 4\pi \times 10^{-7}$

t = time, sec

σ = halfspace conductivity, S/m

d_1 = distance between loop centers

d = effective distance between loop centers, $\approx d_1$ for large d/a

A GENERALIZED IMAGE METHOD FOR QUASI-STRATIFIED MODELS

G.F. West

Department of Physics
University of Toronto
Toronto, Ontario M5S1A7, Canada

We have been looking for a method of computing the EM response of a quasi-stratified earth, i.e., one in which one or more of the layers has a somewhat irregular shape. To our surprise, we discovered that two members of the U. of T. Computer Science Department worked on this problem a few years ago and developed a numerical method which might best be described as a generalized image method*.

The field inside any uniform bounded region can always be described as the summation of fields generated by an array of point sources in an infinite medium of similar properties, where all these point sources (with the possible exception of the true source) lie outside the boundary of the region. (Fig. 1). In a number of simple cases, such as where the boundary is a plane or a sphere, the fields can be represented exactly by one or a finite number of such sources. However, in most cases, an infinite distribution of point sources is required. In the numerical method, one attempts to find a small set of "image" sources (position and strength) for the fields in each region such that the fields on the boundary approximately satisfy the required boundary conditions on a network of test points. The number of test points is taken considerably larger than the number of unknown in the image series and the method of least squares is used to obtain the parameters of the image series. The minimization problem is non-linear in the image position coordinates and the Marquhardt algorithm is used to iterate to the best fit.

We have not tried the method yet, but it looks interesting and we plan to test it this summer. It is unlikely that very complicated shapes can be handled, since this would require many images and the iterative least squares method usually gets into trouble if the number of free parameters is large. However, it may be a simple method for handling some important cases.

* Johnston, R.L. and R. Mathon, 1977. The Computation of Electric Dipole Fields in Conducting Media. Technical Report No. 110, Department of Computer Science, University of Toronto.

Mathon, R. and R.L. Johnston, 1977. The approximate solution of elliptic boundary value problems by fundamental solutions. SIAM J. Numer. Anal. vol. 14, no. 4, pp. 638-650.

XBL 787-1401
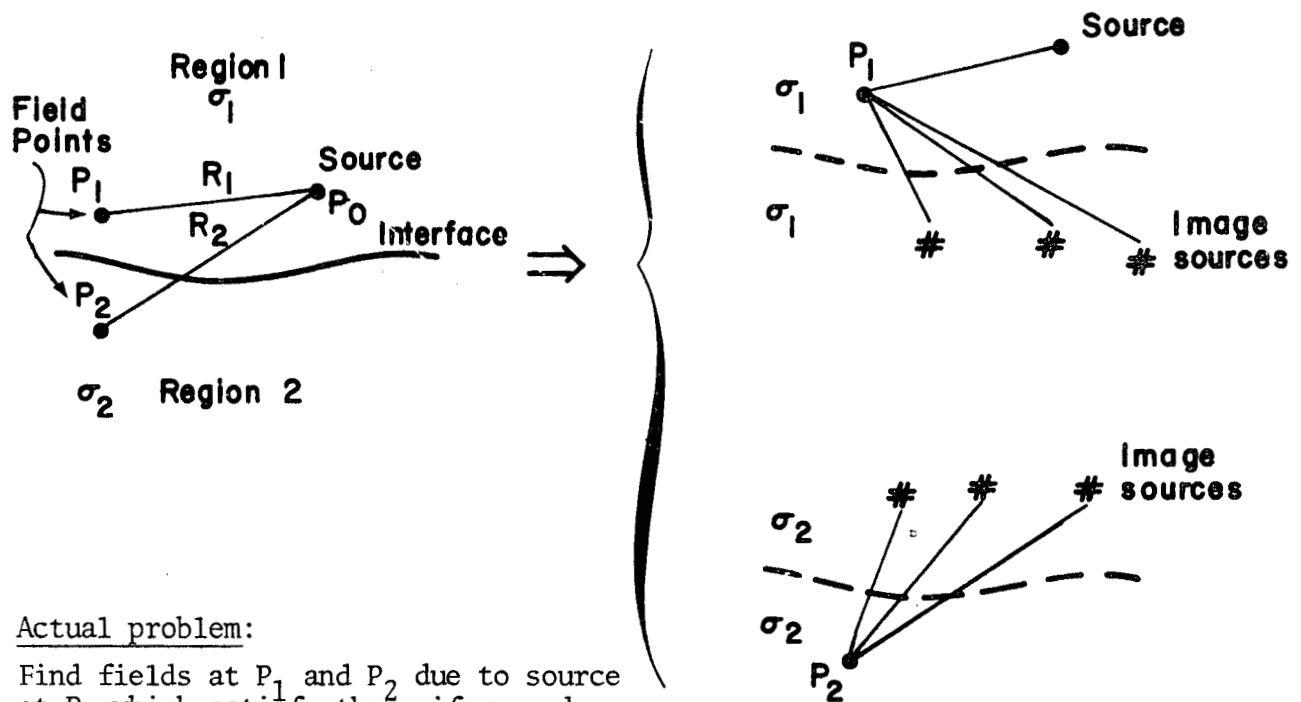
Actual problem:

Find fields at P_1 and P_2 due to source at P_0 which satisfy the uniform medium differential equations with appropriate parameter values in each region, and the boundary conditions on the interface.

Approach:

Write the general solution for the field in each region as the sum of a series of point singularity solutions, where the singularities lie outside the region of interest.

Fig. 1. A generalized image method.

FINITE DIFFERENCE SOLUTIONS FOR

AXISYMMETRIC PROBLEMS

Roy J. Greenfield and Gordon D. Kraft
Geosciences Dept., Penn State University

The finite element method is applied to modeling D.C. electrical resistivity surveys on conductivity structures which are symmetric about an axis. A large class of structures of geophysical interest can be modeled in this geometry: ore bodies which are spherical in shape, flat lying ore bodies of eliptical or disk shape, such ore bodies in areas having layered overburden, complicated well loging geometries, and axially symmetric conductivity changes associated with water flooding or coal gasification. The usual approach can give extension for I.P. modeling. Preliminary indications are that finite element results can also be obtained for electromagnetic sources in this geometry.

The results discussed are from a recent M.S. Thesis at Penn State (Kraft, 1976). This thesis work, which is being continued, outlines the method for the general axially symmetric case and obtains a variety of numerical results for the case when the source is on the symmetry axis. Recently this problem was also addressed by Bibby (1978).

The potential field for an axially symmetric structure may be expressed as

$$\Phi(r,z,\theta) = V_0(r,z) + \sum_{N=1}^{\infty} \{ V_N(r,z) \cdot \cos N\theta + U_N(r,z) \cdot \sin N\theta \}$$

where r, z, and θ are the cylendrical coordinates. The $V_N(r,z)$ and $U_N(r,z)$ are solved as a series of two dimensional problems. This technique, analogous to the method used by Jepsen (1969), Coggon (1971), and Madden (1967) for two dimensional structures, requires less computation than the full three dimensional solution.

Present results are for sources on the axis. Then only the $V_0(r,z)$ term is required, hence the subscript will be dropped. The finite element method requires minimization of the function

$$\chi = \iint\limits_{R} \tfrac{1}{2}\, r\, \sigma\{(\tfrac{\partial V}{\partial r})^2 + (\tfrac{\partial V}{\partial z})^2\}\, drdz + \int\limits_{c} (\tfrac{1}{2}\,\alpha\, V^2 - \beta V)\, dl + \iint\limits_{R} \frac{I_0}{2\pi} V\, \frac{\delta(r-r_0)\delta(z-z_0)}{r}\, rdrdz$$

The α and β come from general linear boundary conditions of the form

$$r\sigma\, \frac{\partial V}{\partial n} + \alpha V - \beta = 0$$

where $\frac{\partial}{\partial n}$ indicates the derivative normal to the boundary. The boundary conditions and resulting α and β used are shown on Figure 1. The conditions on the right side and bottom of the grid result from the assumption that the direction of current flow on the boundary is radially outward from the source. The grids used for the numerical work are formed by dividing the solution region into rectangles by a series of vertical and horizontal grid lines, which are placed at the discretion of the user. Full details of the method are given by Kraft (1976). The program used to obtain results incorporated several subroutines developed by Rodi (1976) for magnetic-telluric modeling. The direct method described by Greenfield (1965) was used to solve the finite difference equations. Typical runs for a 30 x 30 mesh took 15 seconds on the Penn State University IBM 370/175 computer.
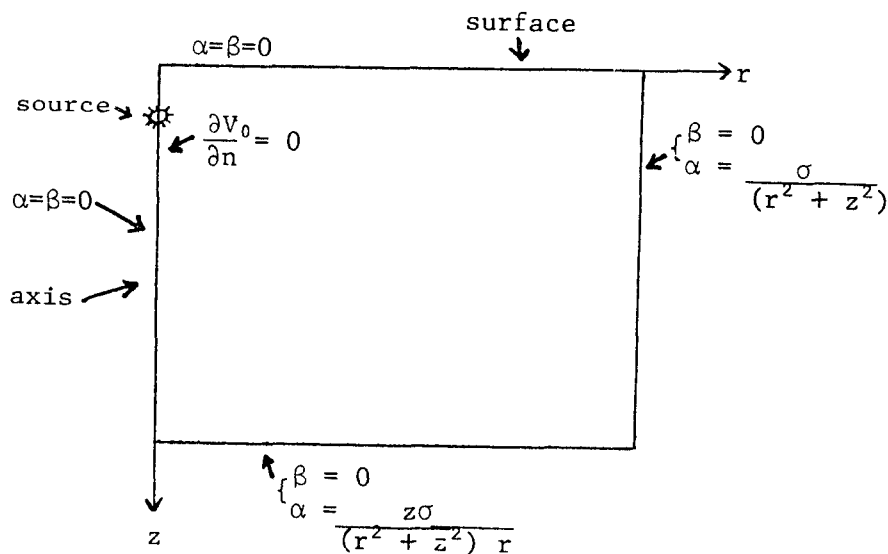
Figure 1. Geometry and outer boundary of mesh shown with boundary conditions indicated for each side of the mesh.

A variety of tests were made of the accuracy of the method by comparison of finite element results to analytic model results. Figure 2 shows the geometry and Figure 3 a comparison of present apparent resistivity results to those of Snyder and Merkel (1973) for the buried conductive sphere (conductivity contrast of 5.). Also shown are additional results for source positions in the sphere. Comparison of results for the resistive sphere gave comparable accuracy. The only appreciable errors are for the surface source ($\eta = 0$) when n is small so that the close electrode is near the source. The grid used had the same uniform spacing (spacing = a/4) in both the horizontal and vertical. Additional accuracy tests were made for a uniform halfspace model and for the model of a layer over a halfspace, with both a conductive and a resistive layer. In all cases accuracies of a few percent or better were obtained, except when a potential electrode was within 4 grid points of either the source electrode or the mesh boundary.

Results were calculated for the series of models shown in Figure 4. This series of models shows the effect, on apparent resistivity, of the horizontal extent of the burried conductive body, A series of curves, not included in this summary, shows apparent resistivity versus potential electrode distance, r, for each body. In Figure 5 a composite curve, for fixed potential electrode distance, is given for all the bodies.

Results were run to analyze the possibility of monitoring water flooding of a layer with a conductive fluid. The model is shown in Figure 6; the conductivity model included a steel well casing. The apparent resistivity results for several values of D, the raduis of the flooded zone, are shown in Figure 7.

These water flooding calculations were done using a mesh that had very small radial spacing ($\Delta r = 0.06$ mm) at the axis (location of pipe) with the spacing increasing by approximately 50% at each node until the node spacing at the outer boundary was $\Delta r = 944$ m. The vertical mesh spacing was uniformly 60 m except for a spacing of 30 m at the layer. Accuracy tests were made using this mesh for the problem of a layer over a halfspace (no pipe) and for the finite length infinitely conductive pipe in a uniform halfspace (compared to the solution of Van Nostrand and Cook, 1966, pp. 28-29). The results showed that this mesh gives results that were accurate to better than a few percent.

References

Bibby, H. M., 1978, Direct current modeling for axially symmetric bodies
    using the finite element method, Geophysics, v.43, pp. 550-562.

Coggon, J. H., 1971b, Induced polarization anomalies: Ph.D. dissertation
    University of California, Berkeley.

Greenfield, R. J., 1965, Two-dimensional calculations of magnetic micro-
    pulsation resonances, Ph.D. thesis, Massachusetts Institute of Technology.

Jepsen, A. F., 1969, Numerical modeling in resistivity prospecting: API
    rep., project 77.

Kraft, G. D., 1976, Two-dimensional finite element direct current electrical
    resistivity modeling of axially symmetric structures, Master's Paper,
    The Pennsylvania State University.

Madden, T. R., 1967, Induced polarization and its application to mineral
    prospecting: Presented at UNO Seminar on new methods for mineral
    exploration, Moscow.

Rodi, W. L., 1976, A technique for improving the accuracy of finite element
    solutions for magnetotelluric data, Geophys. J.R. astr Soc., v.44,
    pp. 483-506.

Snyder, D. D., and R. H. Merkel, 1973, Analytic Models for the interpretation
    of electrical surveys using buried current electrodes, Geophysics, v.38,
    pp. 513-529.

Van Nostrand, R. C. and K. L. Cook, 1967, Interpretation of resistivity data,
    U. S. Geol. Survey Prof. Paper 499.
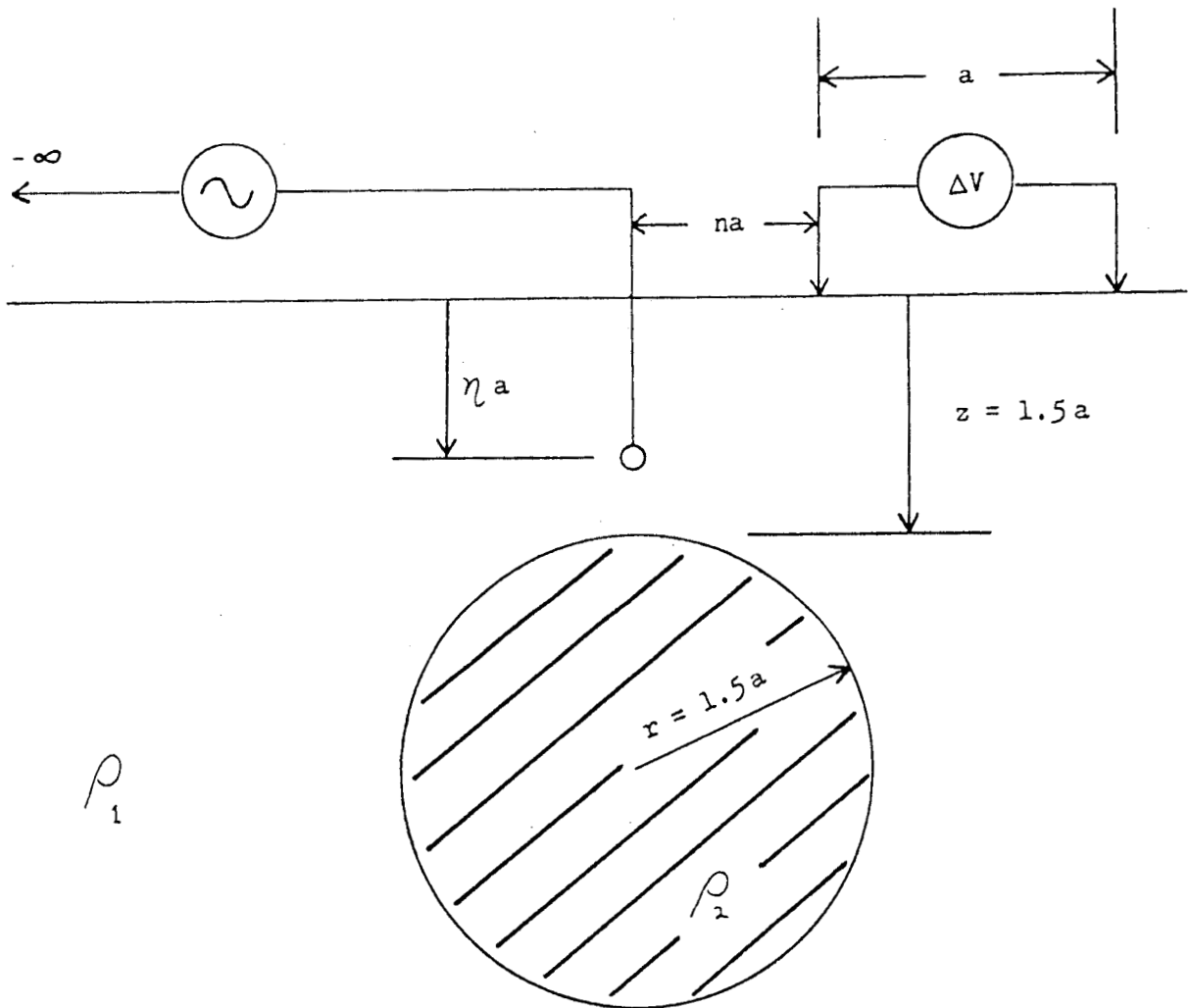
Figure 2. Electrode array geometry of the buried sphere target.
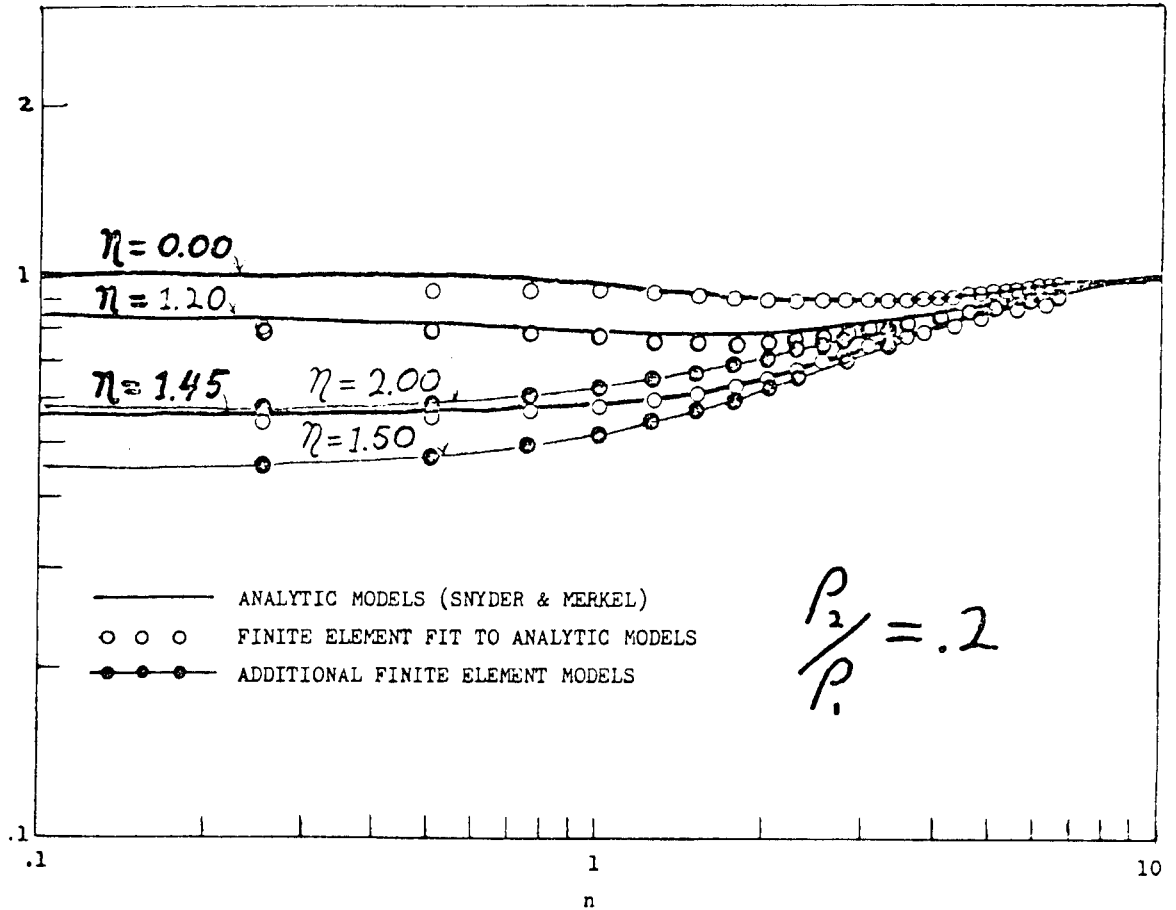
Figure 3 .   Test of finite element calculation using known analytic solution
to apparent resistivity over a conductive sphere in a half-space.
Parameters are specified in Figure 2.

$-\infty$

SURFACE

r

ΔV

h

Variable
source
depth

120 m

Resistivity of sphere, ellipsoids, and layer = .2 ohm-m

Resistivity elsewhere = 1.0 ohm-m

ρ_1

SPHERE   ELLIPSOID 1   ELLIPSOID 2   ELLIPSOID 3   LAYER

ρ_2

ρ_1

60 m

150 m

309 m

502 m
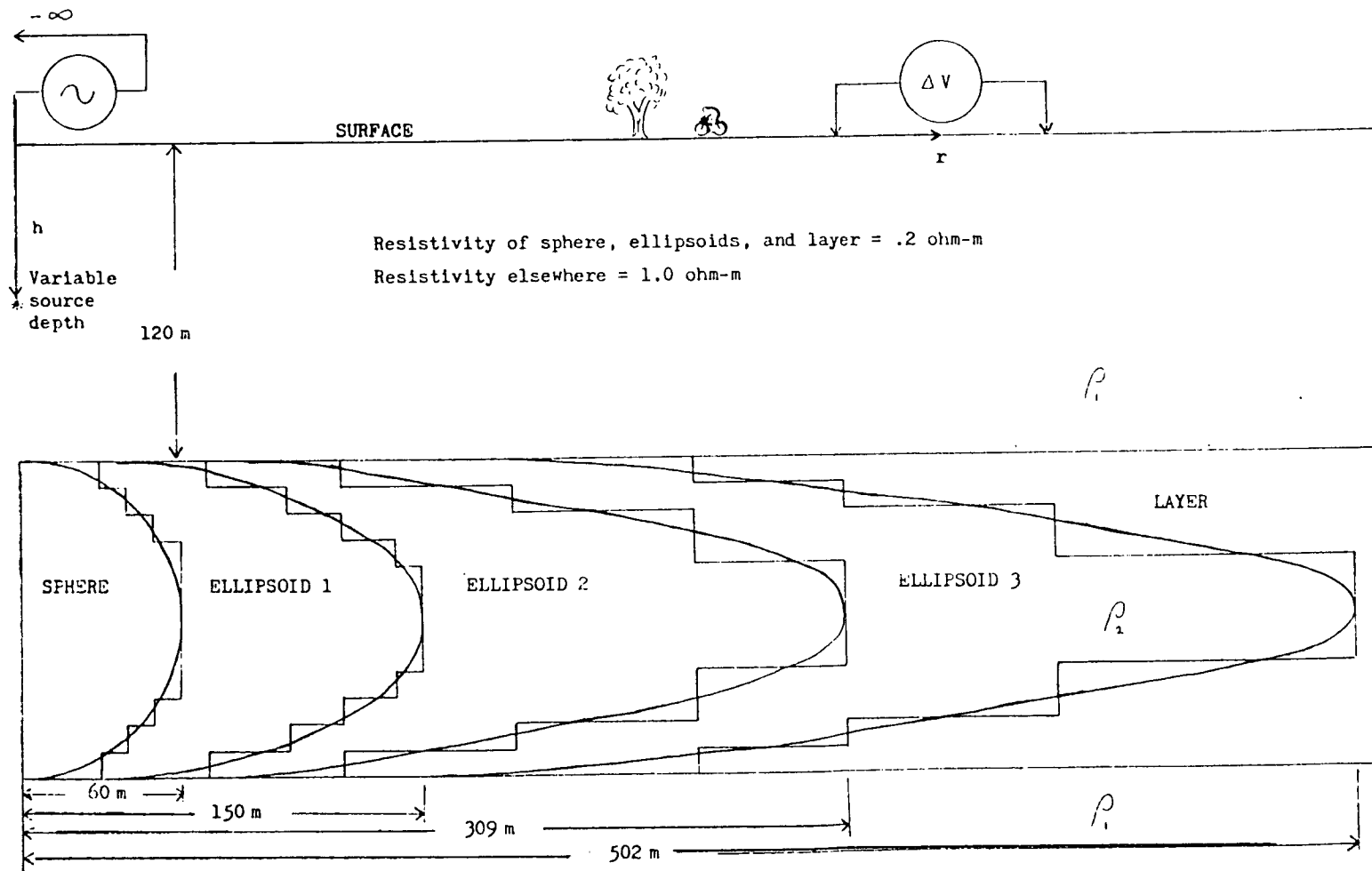
Figure 4. Electrode array geometry and illustration of sphere, ellipsoids, and layer models.
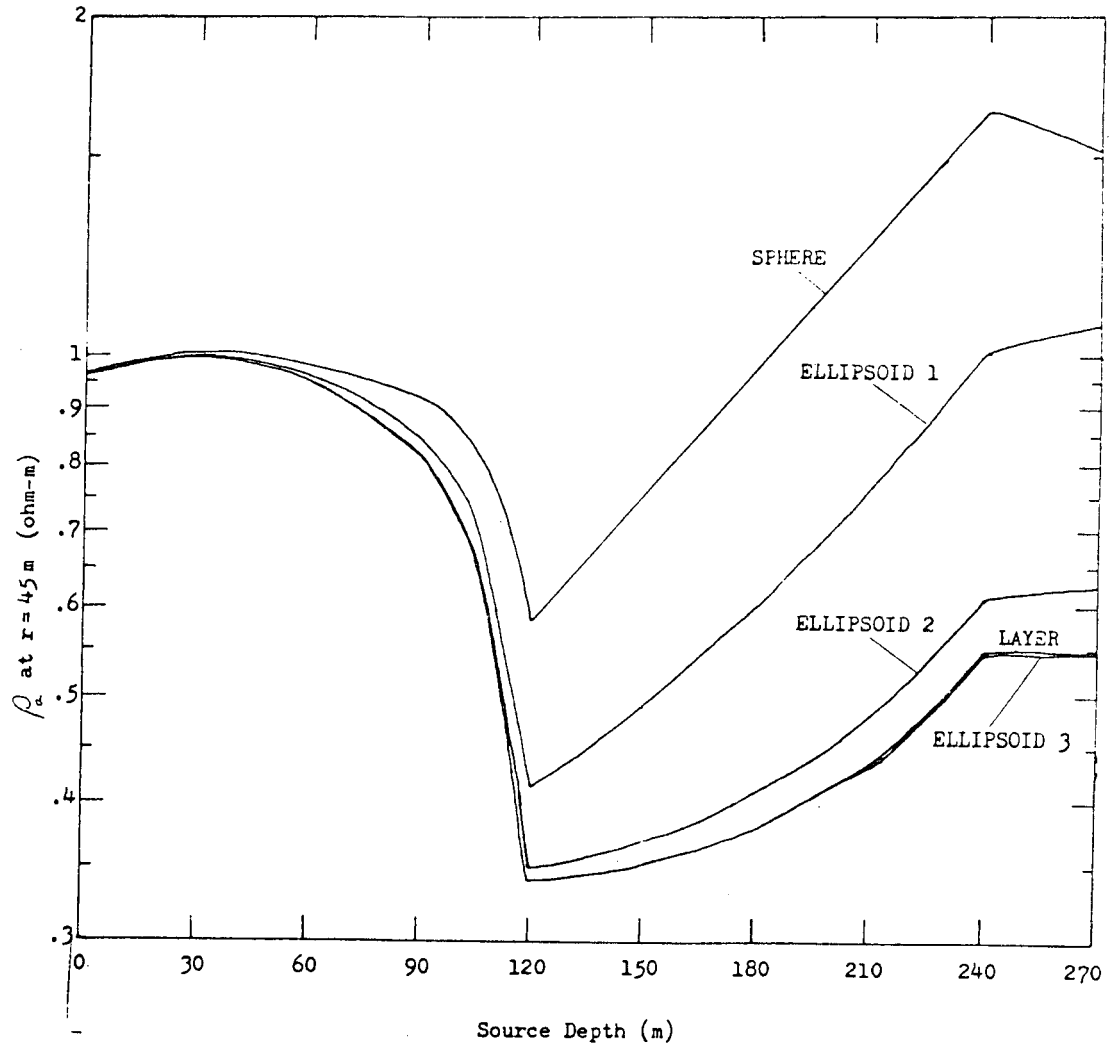
Figure 5. Apparent resistivity at a point 45 m from the axis versus source depth, presented for the sphere, ellipsoids, and layer of Figure 4.
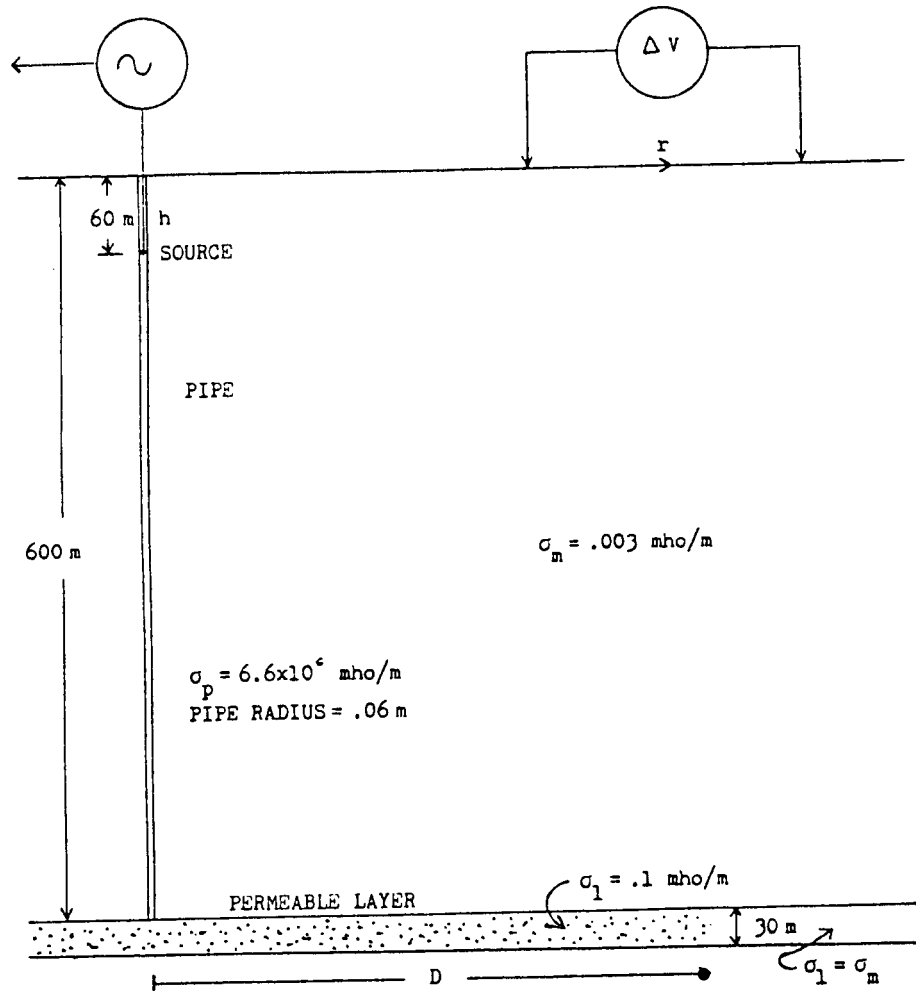
Figure 6. Electrode array geometry and illustration of waterflooding model.
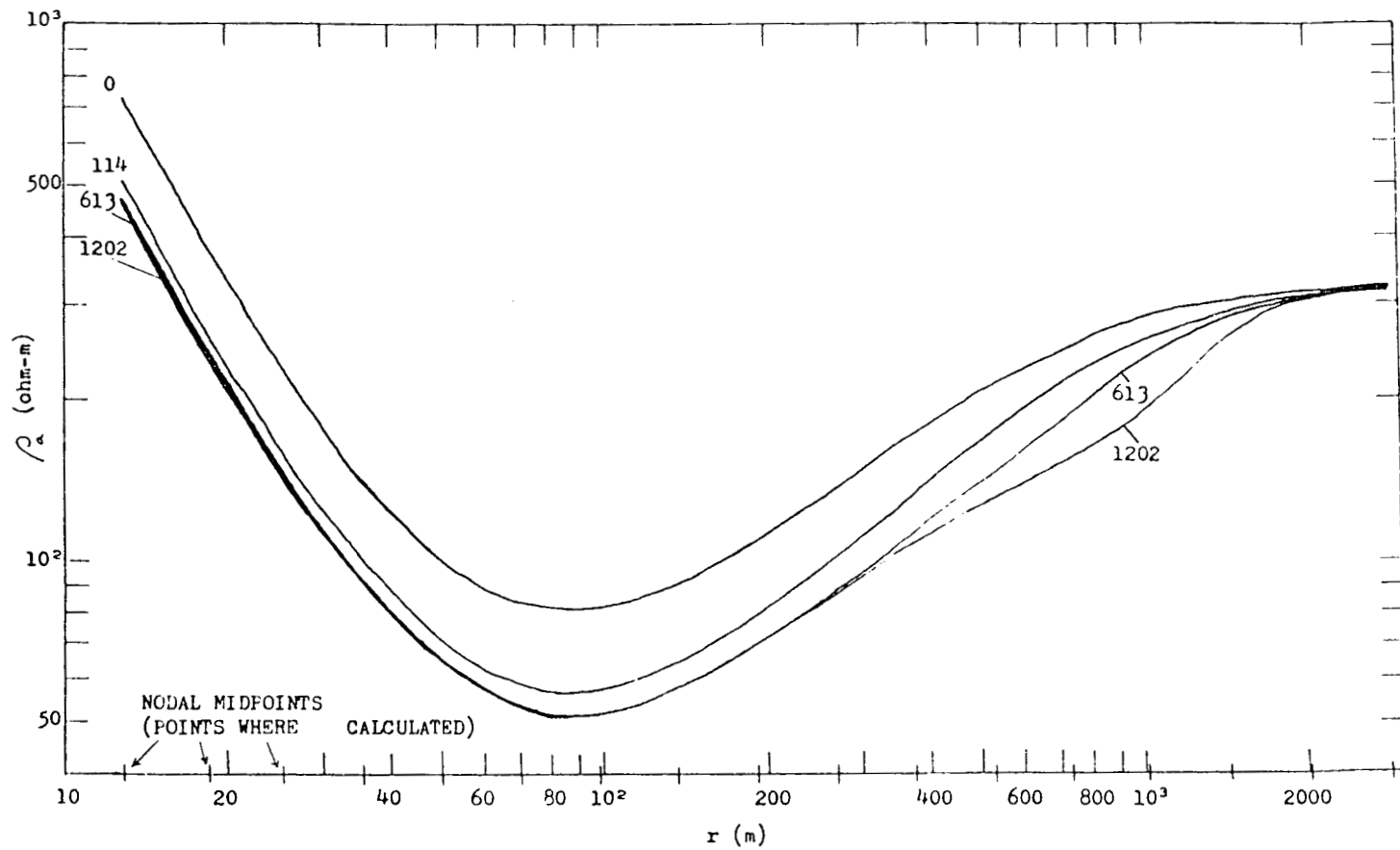
Figure 7. Apparent resistivity versus r, presented for several values of D, the radius of saturation. *D* is given in meters. Other parameters including source depth of 60 m are specified in Figure 6.

FINITE DIFFERENCE SOLUTIONS TO THE THREE-DIMENSIONAL-SOURCE AND TWO-DIMENSIONAL-EARTH ELECTROMAGNETIC PROBLEM

Charles H. Stoyer
Geophysics Department
Colorado School of Mines

Introduction

The numerical solution of the problem concerning geophysical prospecting over structures of infinite strike length with point sources has held the author's interest since about 1972. Following the work of Swift (1967, 1971), the method and software have been developed to extend Swift's purely two-dimensional approach to one which allows the electromagnetic fields to be three dimensional in character.

Since virtually all of these results have been previously published elsewhere (Stoyer, 1974; Stoyer and Greenfield, 1976; Greenfield and Stoyer, 1976; Stoyer and Wait, 1976; Stoyer, 1976) this summary will be a literature review.

The Method

The basis for the method is straightforward. The strike direction is parallel to the x-axis (z is positive downward) and the field components are written as an un-normalized Fourier integral. Substitution of this into Maxwell's equations produces a set of equations in which the x-dependence of the fields is specified as exp (jkx). Since the y- and z-components can be expressed in terms of derivatives of Ex and Hx (in the k-domain), these two components are used as potentials. Two coupled equations in Ex and Hx are then developed; these are coupled only at material boundaries. The finite-difference approximation of these two equations can be easily developed, and both magnetic and current dipole sources are allowed.

Boundary conditions at contacts between media of different electrical properties are automatically taken care of since the equations for inhomogeneous media are used. At the edges of the finite-difference grid, the magnetotelluric terminal impedance, similar to that used by Swift (1967) at the grid bottom, is used for the boundary condition at _all_ grid edges.

The finite difference equations are solved (presently for the total field) for several values of k, logarithmically spaced and spanning about two orders of magnitude, and the inverse transform is carried out by integrating the Lagrange interpolation of the fields in the Fourier integral. The specific values of k are determined from tests with simpler structures, such as a homogeneous or plane-layered earth. Note that the required k values are different for electric and magnetic sources. Solutions cost between $20 and $200, depending on the machine and rate structure used.

Validity of Results

Unfortunately, no absolute test of validity for two-dimensional structures using truly electromagnetic fields has been carried out as yet. This is because a "standard" result (such as scale-model) does not seem to exist. However, comparisons have been made with homogeneous half-spaces, three-dimensional scale models, the perfectly conducting half-plane, field data taken by the author, and direct-current two-dimensional results. There has never been any reason to suspect the validity of the results, except in cases where obvious mistakes, such as using too coarse a grid or the wrong k values, have been made.

Summary of Published Results

Full details of the method are described by Stoyer (1974). These results are strictly for magnetic dipole sources, and the measurement of tilt angle

and ellipticity (for the magnetic polarization ellipse) is considered almost exclusively. Results include the response of buried bodies in layered structures (generated for field data interpretation), comparison of the two-dimensional results with a three-dimensional scale model and with the half-plane solution, and the surface fields of a buried dipole source. Comparisons with field data, taken by the author using equipment designed and constructed by the author, are also presented and resulting interpretations are discussed. A condensed version of Stoyer (1974) is presented in the more accessible Stoyer and Greenfield (1976).

Publications that describe the surface fields of a buried vertical magnetic dipole (for trapped-miner applications) include Greenfield and Stoyer, 1976; Stoyer and Wait, 1976; and Stoyer, 1976. The first of these is a condensed version of the material from Stoyer (1974). The second and third show contour maps on the surface of various field components. Some of the more interesting of these show contour maps of vertical and horizontal ellipticities. These seem to be quite indicative of the position of the more conductive portions of the subsurface.

Recently, results have been generated for the electromagnetic fields of a current dipole over a two-dimensional structure. These results are not yet compiled, as they require the combination of two sources in order to match the field situation for which data interpretations are to be made. Also, they involve fields along a line which is oblique to strike. The results should appear in the future literature.

Final Remarks

The finite-difference solution to the three-dimensional source and two-dimensional earth electromagnetic prospecting problem has been obtained. In order to do this, several approximations must be made, including finite grid size (15x50 nodes),

incorrect grid boundary conditions, numerical differentiation to obtain auxil-
liary field components, and a finite number of k values for the inverse Fourier
transform. Solutions in the vicinity of the source and solutions near grid
boundaries are not valid for several reasons. With a little care, however,
valid and viable solutions to the geophysical prospecting problem can be
obtained; the cost is not negligible, but it is reasonable.

Certainly, improvements can be made which promise to improve the accuracy
and/or decrease the cost of the computations. These include solutions for
secondary fields only, direct computation of all desired field components in
a specified region (such as the air-earth interface), and improved methods of
calculating the inverse transform using fewer k values. However, even the
relatively crude approach which was introduced in the referenced publications
gives results which are generally useful for model studies and geophysical
interpretations. For inversion applications, however, much faster methods of
computation, such as interpolation into data from a curve catalog, are
definitely necessary.

References

Greenfield, R.J., and Stoyer, C.H., 1976, Errors in the location of a buried
    electromagnetic source resulting from lateral change in earth conductivity:
    IEEE Trans. Geosc. Elec.,GE-14, p. 115-117.

Stoyer, C.H., 1974, Numerical solutions of the response of a two-dimensional
    earth to an oscillating magnetic dipole source with application to a
    groundwater field study: Ph.D. Thesis, The Pennsylvania State University.

Stoyer, C.H., 1976, Numerical study of two-dimensional conductors on the
    surface fields of a buried vertical magnetic dipole: Radio Science,
    v. 11, p. 343-349.

Stoyer, C.H., and Greenfield, R.J., 1976, Numerical solutions of the response
    of a two-dimensional earth to an oscillating magnetic dipole: Geophysics,
    v. 41, p. 519-530.

Stoyer, C.H., and Wait, J.R., 1976, Analysis of source location errors for a
    magnetic dipole buried in a laterally inhomogeneous conducting earth:
    PAGEOPH, v. 114, p. 39-51.

Swift, C.M., 1967, A magnetotelluric investigation of an electrical conductiv-
    ity anomaly in the Southwestern United States: Ph.D. Thesis, M.I.T.

Swift, C.M., 1971, Theoretical magnetotelluric and TURAM response from two-
    dimensional inhomogeneities: Geophysics, v. 36, p. 38-52.

2-D INVERSION OF D.C. RESISTIVITY

Alan C. Tripp
Department of Geology and Geophysics
University of Utah
Salt Lake City, Utah 84112

We will first briefly discuss the two dimensional
D.C. resistivity forward problem, following Madden (1971)
and C.M. Swift, Jr. (pers.comm.)

Let's assume that the strike direction is along the
y - axis. If we Fourier transform out the y-direction, the
potential equations

$$\nabla \bar{\phi} = - \rho(x,\mathfrak{z}) \bar{J} \qquad (1)$$

and

$$\nabla \cdot \bar{J} = I \qquad (2)$$

where I represents the current sources, become the transmission
surface equations

$$\frac{\partial \bar{\phi}_\lambda(x,\mathfrak{z})}{\partial x} = - \rho(x,\mathfrak{z}) J_{\lambda x}(x,\mathfrak{z}) \qquad (3)$$

$$\frac{\partial \bar{\phi}_\lambda(x,\mathfrak{z})}{\partial \mathfrak{z}} = - \rho(x,\mathfrak{z}) J_{\lambda \mathfrak{z}}(x,\mathfrak{z}) \qquad (4)$$

$$\frac{\partial J_{\lambda x}(x,\mathfrak{z})}{\partial x} + \frac{\partial J_{\lambda \mathfrak{z}}(x,\mathfrak{z})}{\partial \mathfrak{z}} = - \left(\frac{\lambda^2}{\rho(x,\mathfrak{z})} \right) \bar{\phi}_\lambda(x,\mathfrak{z}) + I_\lambda(x,\mathfrak{z}) \qquad (5)$$

where the λ subscripted variables are defined by the cosine transforms:

$$\Phi(x,y,z) = \int_0^\infty \Phi_\lambda(x,z)\cos(\lambda y)\, d\lambda \qquad (6)$$

$$J_x(x,y,z) = \int_0^\infty J_{\lambda x}(x,z)\cos(\lambda y)\, d\lambda \qquad (7)$$

$$J_z(x,y,z) = \int_0^\infty J_{\lambda z}(x,z)\cos(\lambda y)\, d\lambda \qquad (8)$$

$$I(x,y,z) = \int_0^\infty I_\lambda(x,z)\cos(\lambda y)\, d\lambda \qquad (9)$$

The standard forms for the transmission surface equations are

$$\frac{\partial V}{\partial x} = -Z I_x \qquad (10)$$

$$\frac{\partial V}{\partial z} = -Z I_z \qquad (11)$$

$$\frac{\partial I_x}{\partial x} + \frac{\partial I_z}{\partial z} = -Y V \qquad (12)$$

Comparing equations (3) - (5) with equations (10) - (12) we note the equivalences

$$Z \equiv \rho(x, \zeta) \tag{13}$$

$$Y \equiv \frac{\lambda^2}{\rho(x, \zeta)} \tag{14}$$

$$V \equiv \Phi_\lambda(x, \zeta) \tag{15}$$

$$I \equiv J_\lambda(x, \zeta) \tag{16}$$

Now we wish to approximate the transmission surface by a network. To do this we must approximate the distributed impedance and admittance to ground, Z and Y, by lumped circuit elements.

We will follow this computation through for the resistivity cell (I, J) shown in Figure 1. The network admittance element YV or YH may be viewed as equivalent to two lumped impedance elements in parallel. For example $YV(I, J)$ is the parallel combination of the two lumped impedance elements formed from half of the neighboring $(I, J+1)$ and (I, J) cells:

$$Z(I, J+1) = \frac{\rho(I, J+1) \Delta V(I)}{.5 \Delta H(J+1)} \tag{17}$$

and

$$Z(I, J) = \frac{\rho(I, J) \Delta V(I)}{.5 \Delta H(J)} \tag{18}$$

Thus

$$YV(I,J) = \frac{.5}{\Delta V(I)} \left(\frac{\Delta H(J)}{\rho(I,J)} + \frac{\Delta H(J+1)}{\rho(I,J+1)} \right) \qquad (19)$$

Similarly

$$YH(I,J) = \frac{.5}{\Delta H(J)} \left(\frac{\Delta V(I)}{\rho(I,J)} + \frac{\Delta V(I+1)}{\rho(I+1,J)} \right) \qquad (20)$$

The admittance element $Y(I,J)$ from the node (I,J) to ground is found by adding the lumped admittance of $\frac{1}{4}$ of each of the 4 cells surrounding the (I,J)-the node. Thus

$$Y(I,J) = .25 \lambda^2 \left(\frac{\Delta H(J)\Delta V(I)}{\rho(I,J)} + \frac{\Delta H(J+1)\Delta V(I)}{\rho(I,J+1)} \right.$$

$$\left. + \frac{\Delta H(J)\Delta V(I+1)}{\rho(I+1,J)} + \frac{\Delta H(J+1)\Delta V(I+1)}{\rho(I+1,J+1)} \right) \qquad (21)$$

We may solve for the values of the potentials in the λ domain for the final equivalent network of Figure 1 by invoking Kirchoff's current law at each node and then combining the resultant equations into a matrix equation.

We will now formulate an inversion algorithm using the linearized least squares technique. Utilization of this technique requires that we find $\frac{\partial \rho_a}{\partial \rho(I,J)}$ for a given transmitter-receiver geometry. Now if we specify unit current we have

$$\frac{\partial \rho_a}{\partial \rho(I,J)} = k \frac{\partial \Delta \Phi(i,j)}{\partial \rho(I,J)} \qquad (22)$$

where $\Delta \bar{\Phi}(i,j)$ is the drop in voltage at port i due to unit current at port j , and K is the geometric factor. But we may define a current drop in the λ domain, $\Delta \bar{\Phi}_\lambda(i,j)$. Then

$$\Delta \bar{\Phi}(i,j) = \int_0^\infty \Delta \bar{\Phi}_\lambda(i,j) \cos(\lambda_y) \, d\lambda \qquad (23)$$

The partial derivative becomes

$$\frac{\partial \Delta \bar{\Phi}(i,j)}{\partial \rho(I,J)} = \int_0^\infty \frac{\partial \Delta \bar{\Phi}_\lambda(i,j)}{\partial \rho(I,J)} \cos(\lambda_y) \, d\lambda \qquad (24)$$

Now we want to find an expression for $\dfrac{\partial \Delta \bar{\Phi}_\lambda(i,j)}{\partial \rho(I,J)}$ The chain rule gives:

$$\frac{\partial \Delta \bar{\Phi}_\lambda(i,j)}{\partial \rho(I,J)} = \sum_{\ell=1}^{8} \frac{\partial \Delta \bar{\Phi}_\lambda(i,j)}{\partial Y_\ell} \cdot \frac{\partial Y_\ell}{\partial \rho(I,J)} \qquad (25)$$

where ℓ indexes the network branches that are connected to nodes $(I-1,J-1), (I-1,J), (I,J-1),$ or (I,J) and Y_ℓ is the admittance of the ℓ-th branch. Since for each ℓ the functional dependence of Y_ℓ on $\rho(I,J)$ is given by equations (19), (20), or (21), $\partial Y_\ell / \partial \rho(I,J)$ may be found analytically. To evaluate $\partial \Delta \bar{\Phi}_\lambda(i,j) / \partial Y_\ell$ we need to cite Cohn's sensitivity theorem (Nadden, 1972; Penfield, Spence, and Duinker, 1970). The theorem states that

$$\frac{\partial \Delta \bar{\Phi}_\lambda(i,j)}{\partial z_\ell} = (\Lambda^i I_\ell) \, \Lambda^j I_\ell$$

where z_ℓ is the impedance for the ℓ-th branch of the network, $\Lambda^i I_\ell$ is the current induced in the ℓ-th branch by unit current in the i-th port, and $\Lambda^j I_\ell$ is the current induced in the ℓ-th branch by unit current in the j-th port.

Since $\frac{1}{Y_\ell} = Z_\ell$, we may write

$$\frac{\partial \Delta \Phi_\lambda(i,j)}{\partial Y_\ell} = \frac{\partial \Delta \Phi_\lambda(i,j)}{\partial Z_\ell} \frac{\partial Z_\ell}{\partial Y_\ell}$$

$$= -\Lambda^i V_\ell \, \Lambda^j V_\ell$$

where $\Lambda^i V_\ell$ is the voltage in the ℓ-th branch induced by unit current in the i-th port and $\Lambda^j V_\ell$ is defined similarly. But we have these quantities from the solution of the forward problem.

We now have the equations necessary to derive the derivatives of the potential differences with respect to a cell resistivity. Computational details should be available soon.

Bibliography

1) Madden, T.R., The resolving power of geoelectric measurements for delineating resistive zones within the crust, in "The Structure and Physical Properties of the Earth's Crust," Geophys. Monogr. Ser.,,, vol. 14, edited by J.G. Heacock, AGU, Washington, D.C.

2) Madden, T.R., Transmission systems and network analogies to geophysical forward and inverse problems, Report no. 72-3, Dept. Geol. and Geophys., M.I.T., Cambridge, Mass., 1972.

3) Penfield, P. Jr., R. Spence, and S. Duinker; Tellegen's Theorem and Electrical Networks, M.I.T. Press, Cambridge, Mass., 1970.
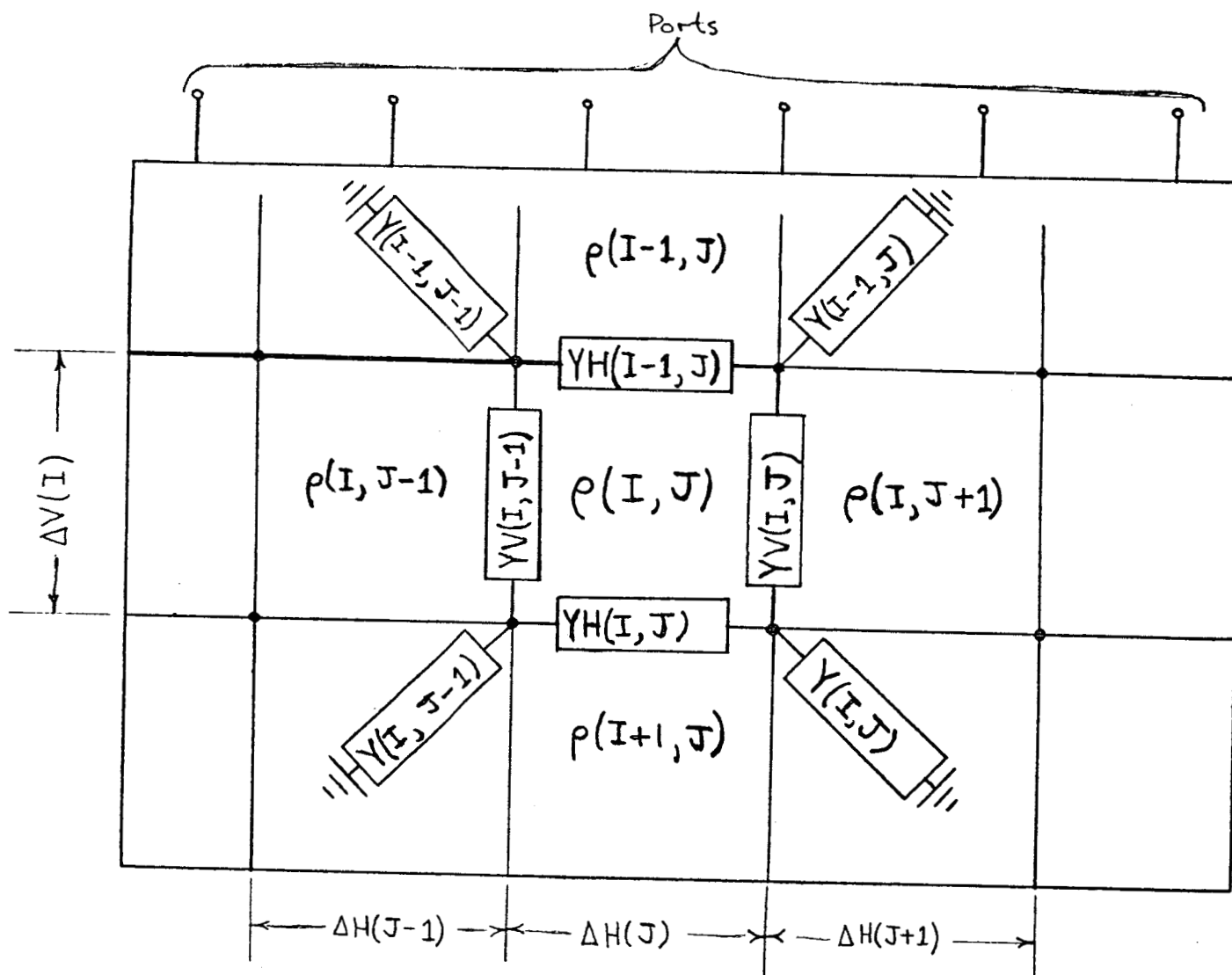
Figure 1

THREE-DIMENSIONAL ELECTROMAGNETIC SCATTERING

F.W. Jones

Department of Physics, University of Alberta
Edmonton, Alberta, Canada   T6G 2J1

During the past few years a numerical method has been used to obtain solutions for the three-dimensional electromagnetic perturbation problem. Maxwell's equations have been solved in terms of the electric field, and the associated magnetic field is then determined. This approach leads to restrictions on the orientation of the source field for models in which conductivity discontinuities extend to the boundaries of the region being considered. In order to make the numerical method more general it would be useful to be able to solve the equations in terms of the magnetic field initially as well.

If we consider electromagnetic fields with a time variation $\exp(i\omega t)$ which is sufficiently slow so that displacement currents may be ignored, we can write Maxwell's equations

$$\nabla \times \underline{H} = \sigma \underline{E} \tag{1}$$

$$\nabla \times \underline{E} = -i\omega \underline{H} \ . \tag{2}$$

Combining these two equations by taking the curl of (2) and substituting from (1) we have an equation in $\underline{E}$:

$$\nabla^2 \underline{E} - \nabla(\nabla \cdot \underline{E}) = i\omega\mu_o \sigma \underline{E} \ . \tag{3}$$

This vector equation may be written as three scalar equations in Cartesian coordinates:

$$\frac{\partial^2 E_x}{\partial y^2} + \frac{\partial^2 E_x}{\partial z^2} - \frac{\partial}{\partial x}\left(\frac{\partial E_y}{\partial y} + \frac{\partial E_z}{\partial z}\right) = i\eta^2 E_x \tag{4}$$

$$\frac{\partial^2 E_y}{\partial x^2} + \frac{\partial^2 E_y}{\partial z^2} - \frac{\partial}{\partial y}\left(\frac{\partial E_x}{\partial x} + \frac{\partial E_z}{\partial z}\right) = i\eta^2 E_y \tag{5}$$

$$\frac{\partial^2 E_z}{\partial x^2} + \frac{\partial^2 E_z}{\partial y^2} - \frac{\partial}{\partial z}\left(\frac{\partial E_x}{\partial x} + \frac{\partial E_y}{\partial y}\right) = i\eta^2 E_z \tag{6}$$

where $\eta^2 = \mu_o \sigma \omega$. These equations may be written in finite difference form and solved simultaneously for E_x, E_y and E_z by the Gauss-Seidel iterative technique over a grid of mesh points which encloses the region of interest. In the finite difference equations used to represent the scalar equations (4), (5) and (6) η^2 is replaced by $\overline{\eta^2}$, the weighted average of η^2 for all the regions surrounding the point being considered (see Brewitt-Taylor and Weaver, 1976). This implies that changes in conductivity are made through transition zones from one conductivity to another and there are gradients in conductivity in these zones.

The method is straightforward and may be applied to models with general conductivity distribution. After the electric fields are determined, the magnetic fields may be approximated using equation (2).

The boundary and initial values may be obtained from a one-dimensional solution when a uniform or layered medium extends to the external boundaries in all directions. However, when lateral discontinuities extend to the boundaries, a two-dimensional model must be employed to obtain the boundary and initial conditions. For the above $\underline{E}$-field approach this implies that the two-dimensional $\underline{E}$-polarization case (Jones and Price, 1970) must be used. However, this restricts the orientation of the source field that can be used for the model.

In an effort to overcome this limitation on the orientation of the source field, and thus make the method of solution more general, we have attempted to solve the equations in $\underline{H}$ rather than $\underline{E}$.

From equations (1) and (2) we can obtain an equation in $\underline{H}$,

$$\nabla^2 \underline{H} - \nabla(\nabla \cdot \underline{H}) - i\omega\mu_o \sigma H + \frac{1}{\sigma} (\nabla\sigma) \times (\nabla\times\underline{H}) = 0 . \tag{7}$$

This equation is similar to equation (3) in $\underline{E}$, except for the last term. This term contains $\nabla\sigma$ and will be zero in all regions of uniform conductivity but non-zero in the transition zones between the different conductive regions.

In the same manner as before we can write equation (7) as three scalar equations in Cartesian coordinates:

$$\frac{\partial^2 H_x}{\partial y^2} + \frac{\partial^2 H_x}{\partial z^2} - \frac{\partial}{\partial x}\left(\frac{\partial H_y}{\partial y} + \frac{\partial H_z}{\partial z}\right) - i\omega\mu_o\sigma H_x + \frac{1}{\sigma}\left[\frac{\partial \sigma}{\partial y}\left(\frac{\partial H_y}{\partial x} - \frac{\partial H_x}{\partial y}\right)\right.$$

$$\left. - \frac{\partial \sigma}{\partial z}\left(-\frac{\partial H_z}{\partial x} + \frac{\partial H_x}{\partial z}\right)\right] = 0 \qquad (8)$$

$$\frac{\partial^2 H_y}{\partial x^2} + \frac{\partial^2 H_y}{\partial z^2} - \frac{\partial}{\partial y}\left(\frac{\partial H_x}{\partial x} + \frac{\partial H_z}{\partial z}\right) - i\omega\mu_o\sigma H_y + \frac{1}{\sigma}\left[-\frac{\partial \sigma}{\partial x}\left(\frac{\partial H_x}{\partial x} - \frac{\partial H_x}{\partial y}\right)\right.$$

$$\left. + \frac{\partial \sigma}{\partial z}\left(\frac{\partial H_z}{\partial y} - \frac{\partial H_y}{\partial z}\right)\right] = 0 \qquad (9)$$

$$\frac{\partial^2 H_z}{\partial x^2} + \frac{\partial^2 H_z}{\partial y^2} - \frac{\partial}{\partial z}\left(\frac{\partial H_x}{\partial x} + \frac{\partial H_y}{\partial y}\right) - i\omega\mu_o\sigma H_z + \frac{1}{\sigma}\left[\frac{\partial \sigma}{\partial x}\left(-\frac{\partial H_z}{\partial x} + \frac{\partial H_x}{\partial z}\right)\right.$$

$$\left. - \frac{\partial \sigma}{\partial y}\left(\frac{\partial H_z}{\partial y} - \frac{\partial H_y}{\partial z}\right)\right] = 0 \qquad (10)$$

These equations may be written in finite difference form and solved simultaneously for H_x, H_y and H_z over the mesh, and the associated electric fields may be obtained from equation (1). In this case the two-dimensional H-polarization case (Jones and Price, 1970) may be used to obtain the boundary and initial values for the general case.

The solution of these H-field equations is not as straightforward as in the E-field case. The last term is very sensitive to conductivity contrasts, and to grid sizes. Also, this term gives rise to difficulties just above the surface of the conducting region where $\sigma = 0$ and $\frac{\partial \sigma}{\partial z}$ is non-zero.

To try and determine how some of these difficulties might be overcome and to see if we might expect to obtain sensible results from calculations of this kind, we have tried a very ad hoc approach. In this, we have assigned a conductivity value to the level of nodes immediately above our original surface level. This then produces non-zero σ and $\frac{\partial \sigma}{\partial z}$ in the last terms of the equation (also, this σ should be included in the fourth term as well). The problem then arises in the next higher level. We must at some point choose $\frac{\partial \sigma}{\partial z} = 0$. The effect is to smear the boundary even more. There may be some alternative approach such as one-sided differences at the surface (and perhaps at internal boundaries as well), or some method using a double mesh, though this may be difficult in practise.

We have computed and compared E-field and H-field solutions for both symmetric and non-symmetric models, though we have found that so far we must use low conductivity contrasts in order to obtain reasonable convergence in the H-field case.

In the symmetric model the two methods give H-fields and E-fields which are comparable. In the more complicated non-symmetric irregular models, one finds that, as expected, the forms of the fields differ. It is clear from the results that it is important to consider both cases, and that results from measurements made in non-uniform regions depend greatly on the orientation of the source field.

References

Jones, F.W. and A.T. Price (1970) Geophys. J.R. astr. Soc.
20, 317-334.

Brewitt-Taylor, C.R. and J.T. Weaver (1976) Geophys. J.R. astr.
Soc. 47, 375-396.

ELECTROMAGNETIC WAVE SCATTERING BY BURIED OBJECTS

Shu-Kong Chang
EMtec Engineering, Inc., and LuTech, Inc.
. Berkeley, CA 94701

SUMMARY

A numerical technique is introduced to solve the electromagnetic wave scattering by localized inhomogeneities buried underground. The basic idea of the technique is to draw an artificial sphere which encloses the entire volume of the scatterer. The fields in the interior of the sphere are solved by the Finite Element Method using the Dirichlet boundary conditions. A new type of multipole expansion which satisfies the boundary conditions of the air-ground interface has been discovered to represent the field outside the artificial sphere. The expansion coefficients are solved by matching the boundary conditions on the sphere.

The multipole expansions include a complete series of vertical electric and magnetic multipoles plus a set of rotating horizontal multipoles. The purpose of adding the rotating multipoles is to ensure the convergence of the expansions. The complete multipole fields satisfying the boundary conditions are derived in terms of the generalized Sommerfeld integrals.

One advantage of the technique is the use of analytical expressions of solutions in the entire space outside an artificial sphere. This enables us to limit the effort of the finite element method only to the interior of the sphere. It is also more efficient than the integral equation approach for material bodies other than thin wire structures, because the latter approach usually involves a time-consuming process of generating the elements of a full matrix which has to be inverted.

REFERENCES

1. S.K. Chang, "On Electromagnetic Wave Scattering by Buried Obstacles", Ph.D. dissertation, University of California at Berkeley, June 1977.

2. K.K. Mei, "Unimoment Method of Solving Antenna and Scattering Problems", _IEEE Transactions on Antennas and Propagation_, AP-22, pp. 760-766, November 1974.

MODELING OF THREE-DIMENSIONAL D.C. ELECTRICAL PROBLEMS USING INTEGRAL EQUATION SOLUTIONS*

L. C. Bartel
Thermal Processes Division
Sandia Laboratories
Albuquerque, New Mexico 87185

SUMMARY

A Green's function integral equation technique has been developed to calculate the electrical potentials and apparent resistivities resulting from three-dimensional structures. The so-called half-space Green's function is used to take into account the earth's surface, and is given by

$$G(\vec{x},\vec{x}') = \frac{1}{4\pi} \left[g_+(\vec{x},\vec{x}') + g_-(\vec{x},\vec{x}') \right] ,$$

where

$$g_{\pm}(\vec{x},\vec{x}') = \left[(x-x')^2 + (y-y')^2 + (z\mp z')^2 \right]^{-1/2} .$$

$G(\vec{x},\vec{x}')$ satisfies the equation

$$\nabla^2 G(\vec{x},\vec{x}') = - \delta(x-x')\, \delta(y-y') \left[\delta(z-z') + \delta(z+z') \right] .$$

Using Green's theorem, the potential throughout the earth half-space is given by

$$\phi(\vec{x}) = \phi_o(\vec{x}) + \int_S dS' \; G(\vec{x},\vec{x}') \, \frac{\sigma(\vec{x}')}{\varepsilon_o} \; ,$$

where ϕ_o is the potential resulting from a source, the surface integral is over all surfaces of resistivity contrasts (excluding the earth's surface), and σ is the induced surface charge density on these surfaces. The integral equation for this charge density is

$$\frac{\sigma(\vec{x})}{\varepsilon_o} = 2K_s \left\{ \frac{\partial \phi_o(\vec{x})}{\partial n} \bigg|_S + \int_S' dS' \; \frac{\partial G(\vec{x},\vec{x}')}{\partial n} \bigg|_S \frac{\sigma(\vec{x}')}{\varepsilon_o} \right\} \; ,$$

where

$$K_s = \frac{\rho_{in} - \rho_{out}}{\rho_{in} + \rho_{out}} \; .$$

The normal derivative of G is an outward normal, the surface integral leaves out the point $\vec{x} = \vec{x}'$, and "in" and "out" refer to inside and outside the surfaces of resistivity contrast, respectively. Only time independent (d.c.) solutions have been addressed to date for both point and three-dimensional current sources.

For the computer solutions to the integral equation, the surfaces of resistivity contrast are divided into finite elements where the normal derivative of the Green's function is integrated over these elements to improve the accuracy of the calculation. The resulting equations for the charge density at point i and the potential at point k become

$$\bar{\sigma}_i = 2K_i \left\{ \left\langle \frac{\partial \phi_o}{\partial n_i} \right\rangle_i + \sum_{j \neq i} \frac{1}{S_j} \left\langle \left\langle \frac{\partial G(i,j)}{\partial n_i} \right\rangle_i \right\rangle_j \bar{\sigma}_j \right\}$$

and

$$\phi_k = \phi_{o_k} + \sum_{j \neq k} \frac{1}{S_j} <G(i,j)>_j \; \bar{\sigma}_j \; ,$$

where $<>_i = \int_{S_i} dSi$, $\bar{\sigma}_i = \frac{1}{\varepsilon_o} <\sigma>_i$, and S_i is the surface area of the i-th element. The solution for the charge density $\bar{\sigma}$, along with any constraint conditions, is obtained by solving a set of linear algebraic equations.

To illustrate the integral equation technique, the results of an illustrative model calculation are shown in the figure. Shown are responses for a half-Schlumberger survey over both an insulating and a conducting buried, finite-sized, dike-like structure.

The emphasis on the modeling work has been to describe field results from using electrical methods to monitor the in situ gasification of coal and re-torting of oil shale and to map hydraulic fractures in the oil shale and natural gas stimulation programs.

B remains fixed at ~500 m

Host medium 200 ohm-m

Apparent Resistivity (ohm-m)

Distance in metres

INSULATOR

Host medium 200 ohm-m

Apparent Resistivity (ohm-m)

Distance in metres
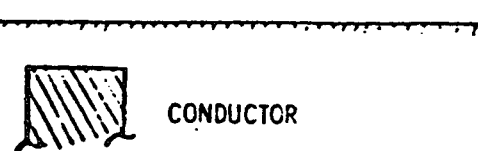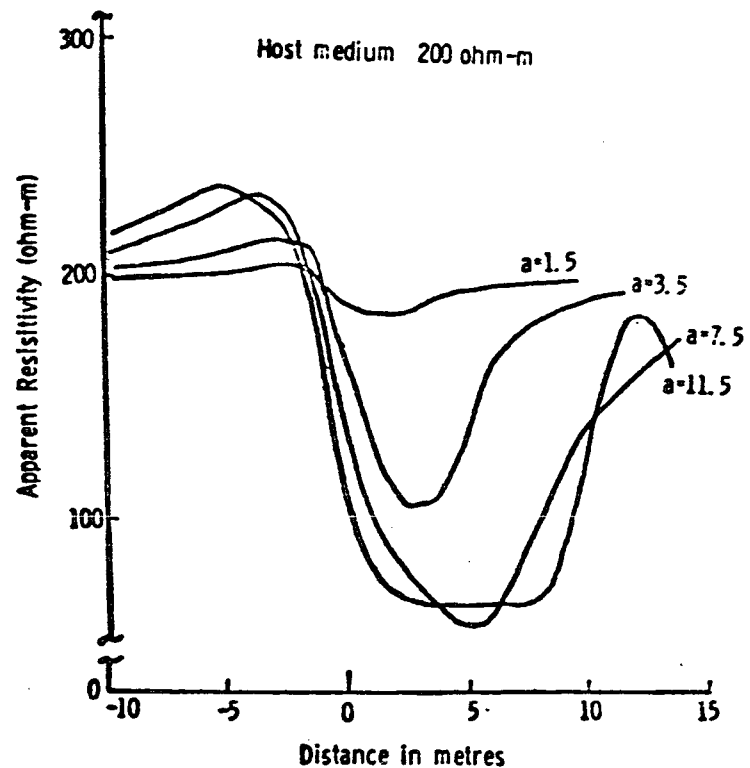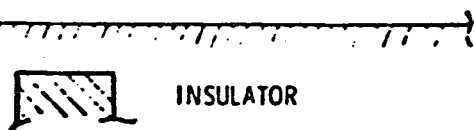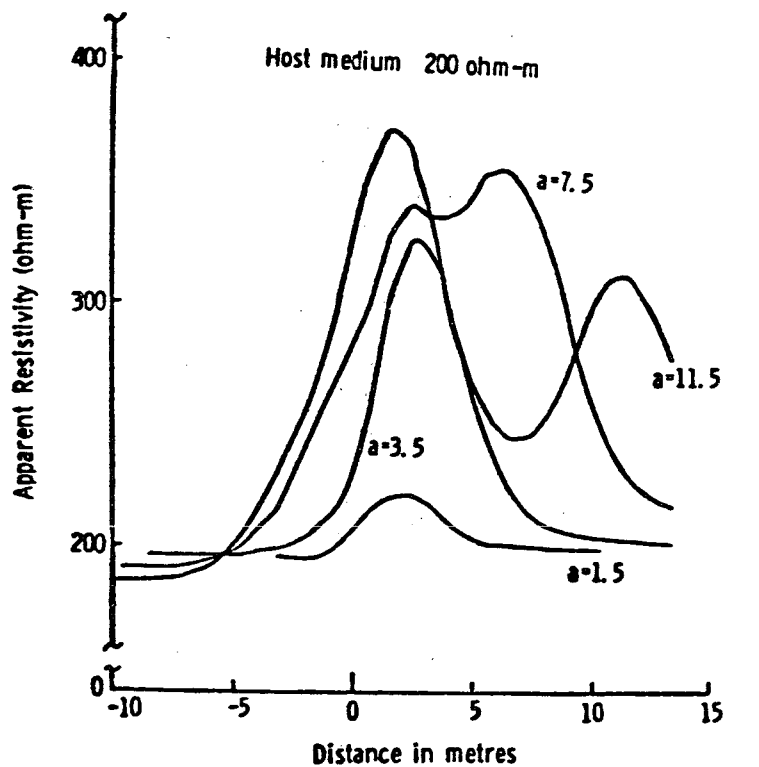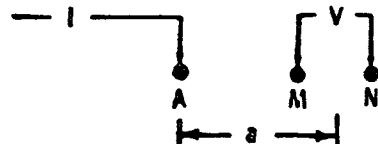
CONDUCTOR

Responses for a half-Schlumberger survey over an insulator and over a conductor.

THE THEORY OF THE MAGNETOMETRIC RESISTIVITY METHOD

R. N. Edwards
Department of Physics
University of Toronto
Toronto, Canada

The Magnetometric Resistivity (MMR) method is based on the measurement of the low level, low frequency magnetic fields associated with non-inductive current flow in the earth. A component of the magnetic field is measured in the vicinity of one or more grounded electrodes. The experimental aspects of the method are described in Edwards (1974) and Edwards and Howell (1976), including the apparatus, the field procedure, the factors which influence the location of the current electrodes, the reduction and normalization of the observations and the interpretation of the 'MMR anomalies'.

The mathematical aspects of the method are presented in a review paper by Edwards, Lee and Nabighian (1978). A horizontal-layered earth yields no MMR anomaly. At first, this seems strange for clearly the current flow in the ground is perturbed and may even be restricted to a thin layer at the earth's surface. However, the perturbation or anomalous currents set up are poloidal and totally enclose the toroidal anomalous magnetic field caused by them. This toroidal field can only be detected by lowering a magnetic field detector through the layers.

The contours of the magnetic field amplitude about a single electrode embedded at the surface of a uniform earth are circles. They are distorted into elliptical shapes if the earth is laterally anisotropic, the ratio of the semi-axes of the elliptical figures being the ratio of two complete elliptic integrals $K(k)/E(k)$, where k is the coefficient of anisotropy. The characteristic anomalies for vertical and dipping contacts, for thin and thick dikes and semi-cylindrical and hemispherical depressions as well as 'alpha' media are described in this paper in some detail.

Gomez-Trevino and Edwards (1978) describe an inexpensive rapid method for computing all three components of the magnetic field due to current flow from a point electrode in the vicinity of a conductive anomaly of infinite strike length and arbitrary cross-section.

For any three-dimensional structure, the magnetic field may be written as a sum of surface integrals over boundaries defining changes in conductivity by a direct modification of the Biot-Savart law. The integrand of each surface integral includes components of the electric field tangential to the boundary, viz.

$$\underline{B}(r) = k_m \int_V \frac{\underline{\nabla}' U \times \underline{\nabla}' \sigma}{|\underline{r} - \underline{r}'|} \, dv'$$

where Ohm's law, in the form $\underline{J} = -\sigma\underline{\nabla}U$, is obeyed in the volume V.

In the case of a two-dimensional, cylindrical structure, a reformulation of the theory by taking a one-dimensional Fourier Transform along the strike (y-direction), results in the reduction of the surface integrals necessary to solve the integral equation for the free charge, and in those used to compute the potential and subsequently the magnetic field, to line integrals in wavenumber domain.

The numerical solution closely follows the work of Barnett (1972) and is described fully in Gomez-Trevino (1977). The final integral for the anomalous horizontal x-component of the magnetic field at the surface of the earth $Z = 0$ looks like

$$Bx^a (x,\lambda) = -\left(\frac{\sigma_1 - \sigma_2}{\sigma_1}\right) \left(\frac{i2k_m I\lambda}{\pi}\right) \sum_{i=1}^{N} n_{zi} V_i H_i(x) - \left(\frac{i2k_m \lambda I}{\pi}\right) \sum_{K=1}^{M} V_K^a H_K(x)$$

where

$$H_i(x) = \int_{\text{element } i} K_0(\lambda \{ (x-x')^2 + Z'^2 \}^{\frac{1}{2}}) \, dc' \quad ;$$

σ_1 is the conductivity of the host medium;

σ_2 is the conductivity of a cylindrical inhomogeneity;

n_{zi} is the direction cosine to the vertical of the local normal to the cylinder;

$V_i = \sigma_1 \pi U_i / I$;

$V_K^a = \sigma_1 \pi U_K^a / I$, where U_K^a is the difference between the true potential U and the potential due to the source in a medium of constant conductivity σ_1 ;

and I is the current from the electrode located at the origin of coordinates.

The summations i and K are respectively over the contour of the cylinder, divided into N straight line segments, and the contour of the surface of the earth, divided into M straight line segments.

There are corresponding expressions for the y and z components of the field.

About ten wavenumbers, strategically chosen, are sufficient to define $\underline{B}(\lambda)$ for most models. The final step in the numerical procedure is to interpolate $\underline{B}(\lambda)$ in the form $\ln (\underline{B}(\lambda)/\lambda)$ and then take the numerical inverse Fourier transform to obtain $\underline{B}(y)$.

Gomez-Trevino and Edwards compute type curves and characteristic curves for the model of a circular cylinder buried beneath a thin conductive overburden. They show that in the presence of overburden, the form of the MMR anomaly may be predicted in a simple manner from the corresponding anomaly in the absence of overburden.

References

Barnett, C.T., 1972, Theoretical modelling of IP effects due to arbitrarily shaped bodies: Ph.D. thesis, Colorado School of Mines.

Edwards, R.N., 1974, The magnetometric resistivity method and its application in the mapping of a fault: Can. J. Earth Sci. v.11, p. 1136-1156.

Edwards, R.N. and Howell, E.C., 1976, A field test of the magnetometric resistivity method: Geophysics, v. 41, p. 1170-1183.

Edwards, R.N., Lee, H. and Nabighian. M.N.. 1978, On the theory of magnetometric resistivity methods: Geophysics, 8v. 43, 48 pages.

Gomez-Trevino, E., 1977, The magnetometric resistivity response of two-dimensional structures: M.Sc. thesis, University of Toronto.

Gomez-Trevino, E. and Edwards, R.N., Magnetometric resistivity anomalies of two-dimensional structures: Geophysics, submitted for publication, May 1978.

A PLATE CONDUCTOR IN A STRATIFIED SPACE

G.F. West

Department of Physics
University of Toronto
Toronto, Ontario M5S1A7,Canada

J. J. Lajoie and G. F. West have published numerical
model results for the Turam EM method for the case of a vertical,
rectangular, thin plate conductor in a half space of different conduct-
ivities and in a half space under a conductive overburden layer (1).
The computation was done by the integral equation method and the scattering
current in the plate was represented by separate scalar potentials for its
solenoidal and irrotational parts. The Green's functions were computed by
the FFT method (2). The model results were well tested and are thought to
be very reliable in form and dependence on induction numbers   although
not necessarily very accurate as to anomaly amplitude.

The work was the Ph.D. thesis of J. Lajoie (3) and the
programs were never developed into general purpose form so they are not
available for distribution. Considerable hand tuning was required for some
of the electric modes as the edge representation was critical.

Since Lajoie's work, we have been using a numerical method
developed by P. Annan (4) for routine calculation of plate models in free
space. This uses the Galerkin method with continuous basis functions for
solving the integral equation. As an intermediate step, a set of eigencurrents
(non-interacting induced current systems i.e. normal modes) is computed, each
of which has a simple, single pole, frequency response. Thus it has some
important advantages in transforming easily between frequency and time.

We expect to reconstruct the full plate model this year using ideas from both these methods. The separation of irrotational and solenoidal components will be retained, but the choice of potentials may be altered. The Galerkin method with continuous basis functions will be employed, but the full orthogonalization procedure used by Annan will not likely be used as it would have to be redone for each change in host medium.

1. Lajoie, J.J. and G.F. West, 1976. Electromagnetic response of a conductive inhomogeneity in a layered earth, Geophysics, vol. 41, no.6A, pp.1133-1156.

2. Lajoie, J.J., J. Alfonso-Roche and G.F. West, 1975. Response of an arbitrary source on a layered earth; a new computational approach, Geophysics, vol. 40, no. 5, pp. 773-789.

3. Lajoie, J.J. The Electromagnetic Response of a Conductive Inhomogeneity in a Layered Earth. Ph.D. Thesis, University of Toronto, October 1973. (Also issued as Research in Applied Geophysics, U. of T., Report No. 6).

4. Annan, A.P. The Equivalent Source Method for Electromagnetic Scattering Analysis and Geophysical Application, Ph.D. Thesis,Memorial University of Newfoundland. 1974.

THREE-DIMENSIONAL INTEGRAL EQUATION MODELING

Gerald W. Hohmann
Department of Geology and Geophysics
University of Utah
Salt Lake City, Utah 84112

Introduction

I have been using a three-dimensional (3D) integral equation solution (Hohmann, 1975) for several years to simulate the response of the earth for various electrical prospecting methods. The computer program provides good results for DC applications, and for EM problems at low frequencies and low conductivity contrasts. However, its application to electromagnetic (EM) exploration for massive sulfides is limited due to the large amount of computer storage required for large conductivity contrasts.

Recently we have incorporated the integro-difference method (Harrington, 1968) in the solution for greater accuracy, and have applied it to magneto-telluric (MT) modeling. Convergence checks and comparisons with 2D models indicate that the results are valid. Initial calculations show that 3D models are required for MT interpretation in complex environments.

In this summary paper I briefly discuss the integral equation formulation, applications and limitations of the numerical solution, and initial MT results.

Integral Equation Formulation

The details of the integral equation formulation are given by Hohmann (1975) and will not be repeated here. An inhomogeneity is replaced by a volume of polarization currents, which are treated as the source of the secondary field. The secondary electric field then is given by

$$\bar{E}_s = -i\omega\mu \, \bar{A} - \nabla\phi, \tag{1}$$

where $\bar{A}$ and ϕ are vector and scalar potentials given in the earth by

$$\bar{A} \, (\bar{r}) = \int_V \bar{J}s \, (\bar{r}')G(\bar{r}, \, \bar{r}') \, dv, \tag{2}$$

and

$$\phi(\bar{r}) = -\frac{1}{\sigma_1} \int_V \nabla \cdot \bar{J}s(\bar{r}') \, G \, (\bar{r}, \, \bar{r}') \, dv \tag{3}$$

where $G \, (\bar{r}, \, \bar{r}')$ is a scalar, half-space Green's function (different for [2] and [3]), and where

$$\bar{J}_s = \Delta \, \sigma \, \bar{E} \tag{4}$$

is the polarization current, with $\Delta\sigma$ the difference in conductivity between the inhomogeneity and the half space, and $\bar{E}$ the total electric field.

An integral equation for $\bar{J}_s$ is obtained by adding the incident (homogeneous-earth) and secondary electric fields and applying (4). I solve the integral equation via the method of moments, with pulse basis functions and delta weight functions (Harrington, 1968). The secondary electric field outside the body is given by (1), and the secondary magnetic field is given by

$$\bar{H}_s = \nabla \times \bar{A} \tag{5}$$

To achieve greater accuracy it would be desirable, but very difficult, to use higher-order basis functions. Instead, I have incorporated the integro-difference technique (Harrington, 1968), wherein both current and charge are expanded in pulse functions, and the derivatives in (1) are approximated by differences. This gives an effect similar to that of higher-order basis functions (Miller and Deadrick, 1975), but is much easier to implement. The details of the formulation are given by Hohmann and Ting (1978).

IP - Resistivity Modeling

Resistivity and IP responses can be modeled by setting the frequency to zero. The DC solution is easier, because the vector potential term drops out, and Green's functions are simpler. Presumably a surface, scalar integral equation formulation would be more efficient, but my solution is more general in that it can account for EM coupling.

Good self-checks and comparisons with other solutions (Hohmann, 1975) show that the results are valid. For example, Figure 1 illustrates two self-checks -- convergence and reciprocity -- which any numerical solution must satisfy. The model is a conductive cube two units (dipole lengths) on a side; its depth is one unit. IP response, as percent of intrinsic response, is plotted in pseudosection form. Results are nearly identical when the body is divided into 8 and 64 cubes, indicating convergence. The transmitter was to the left and the receiver to the right for each calculation. Reciprocity is satisfied: results are the same when transmitter and receiver are interchanged.

Some Useful Approximations

It is not really necessary to calculate apparent resistivity twice or to double the matrix size by making it complex in order to compute IP. Since IP can be modeled by changing slightly (perturbing) the resistivity of a polarizable body and recomputing apparent resistivity, we can use a perturbation method to avoid the second matrix inversion, as suggested by Ted Madden (p.c.).
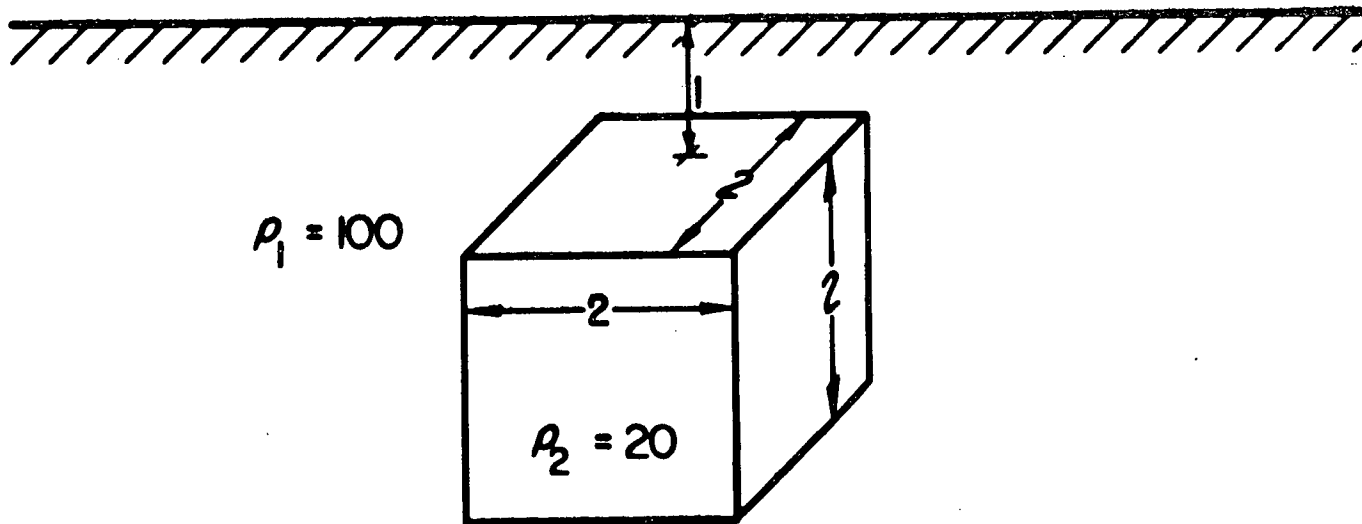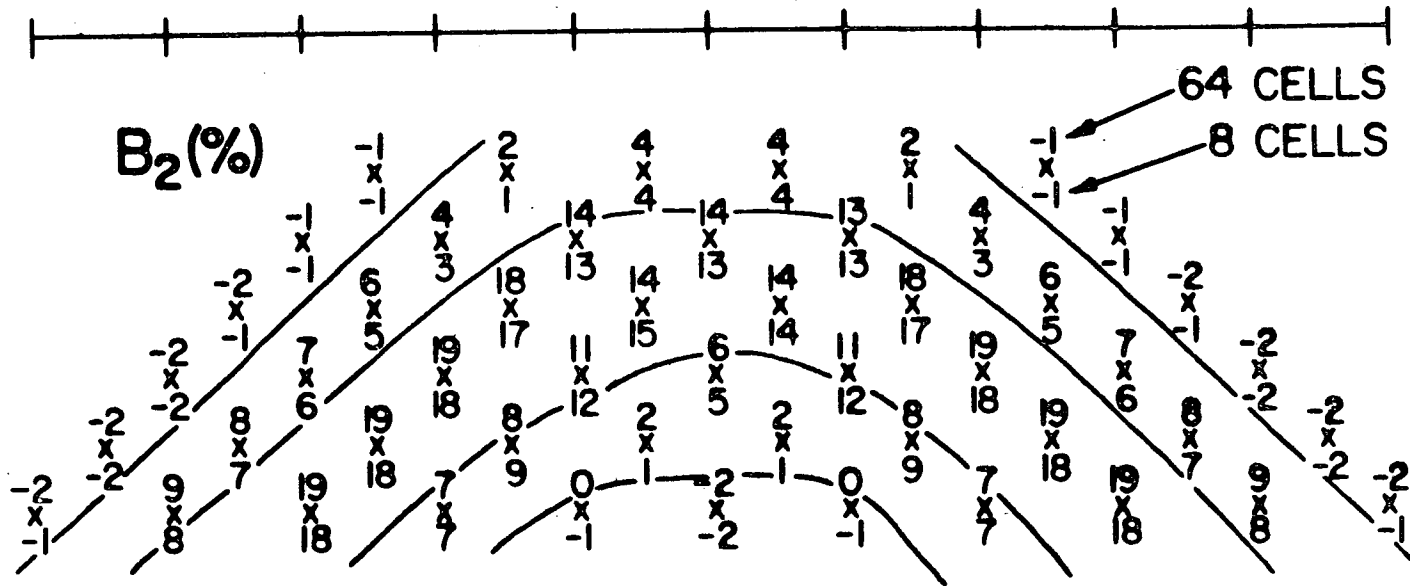
Figure 1 Check for Convergence and Reciprocity for Integral Equation Solution

If we perturb the resistivity of a body, the matrix equation becomes

$$(\overline{\overline{K}}+\Delta\overline{\overline{K}}) \cdot (\overline{\alpha}+\Delta\overline{\alpha}) = \overline{s}, \tag{6}$$

where $\Delta\overline{\overline{K}}$ and $\Delta\overline{\alpha}$ are small changes in the matrix and solution, respectively. Expanding, we obtain

$$\overline{\overline{K}} \cdot \overline{\alpha} + \overline{\overline{K}} \cdot \Delta\overline{\alpha} + \Delta\overline{\overline{K}} \cdot \overline{\alpha} + \Delta\overline{\overline{K}} \cdot \Delta\overline{\alpha} = \overline{s}. \tag{7}$$

Neglecting second order terms $(\Delta\overline{\overline{K}} \cdot \Delta\overline{\alpha})$ and noting that $\overline{\overline{K}} \cdot \overline{\alpha} = \overline{s}$ we obtain

$$\overline{\overline{K}} \cdot \Delta\overline{\alpha} = -\Delta\overline{\overline{K}} \cdot \overline{\alpha}, \tag{8}$$

which is similar to the original matrix equation. Thus, the perturbation in the solution is given by

$$\Delta\overline{\alpha} = -\overline{\overline{K}}^{-1} (\Delta\overline{\overline{K}} \cdot \overline{\alpha}). \tag{9}$$

But the time consuming part of a solution is in computing the inverse matrix, $\overline{\overline{K}}^{-1}$, which we already have done to solve the unperturbed problem. Thus we have obtained a first order solution to the perturbed problem by simple matrix multiplications which take little computer time.

Two other approximations I shall discuss apply only to integral equations. Differential equation solutions are "brute force" methods requiring little mathematical theory, and as such they are easier to program on a computer. One advantage of integral equation solutions is that the mathematics are carried further, and there are many possibilities for approximations that significantly reduce computer time but still yield results that are accurate enough. If there are no resistivity contrasts in a model, the IP response

can be calculated very simply even on a programmable calculator, because
only the diagonal elements of the matrix are needed. That is, there are no
significant interactions between cells. There are no computer storage limi-
tations, and very large models can be handled easily.

Computer time for an integral equation solution involving two or more
bodies can be reduced dramatically if interactions among them are ignored.
Figure 2 shows the errors caused by ignoring interactions between two conduc-
tive 1 x 4 x 5 bodies two dipoles apart. The upper numbers account for the
interactions, while the lower numbers do not. The approximate values are close
enough for geophysical purposes, considering that the earth is more complex
than these simple models, and that data always have some noise. However,
because the full solution requires double the number of cells, and computer
time increases as the cube of the number of cells, the approximate solution
is much less expensive.

Applications

Interpretation: At Kennecott Exploration, Inc. we used the integral equation
solution for IP-resistivity survey design and routine interpretation for a
number of years. Often one needs to interpret a number of lines simultaneously
using an interactive computer terminal. Complex models can be designed by
specifying large cells at depth and away from the lines. The cost of such
an interpretation is miniscule compared with the cost of collecting the data.

A systematic catalog of 3D models must be available both for initial field
interpretation and for insight to apply in the interactive procedure. Some
useful illustrations from such a catalog are given by Hohmann (1977).
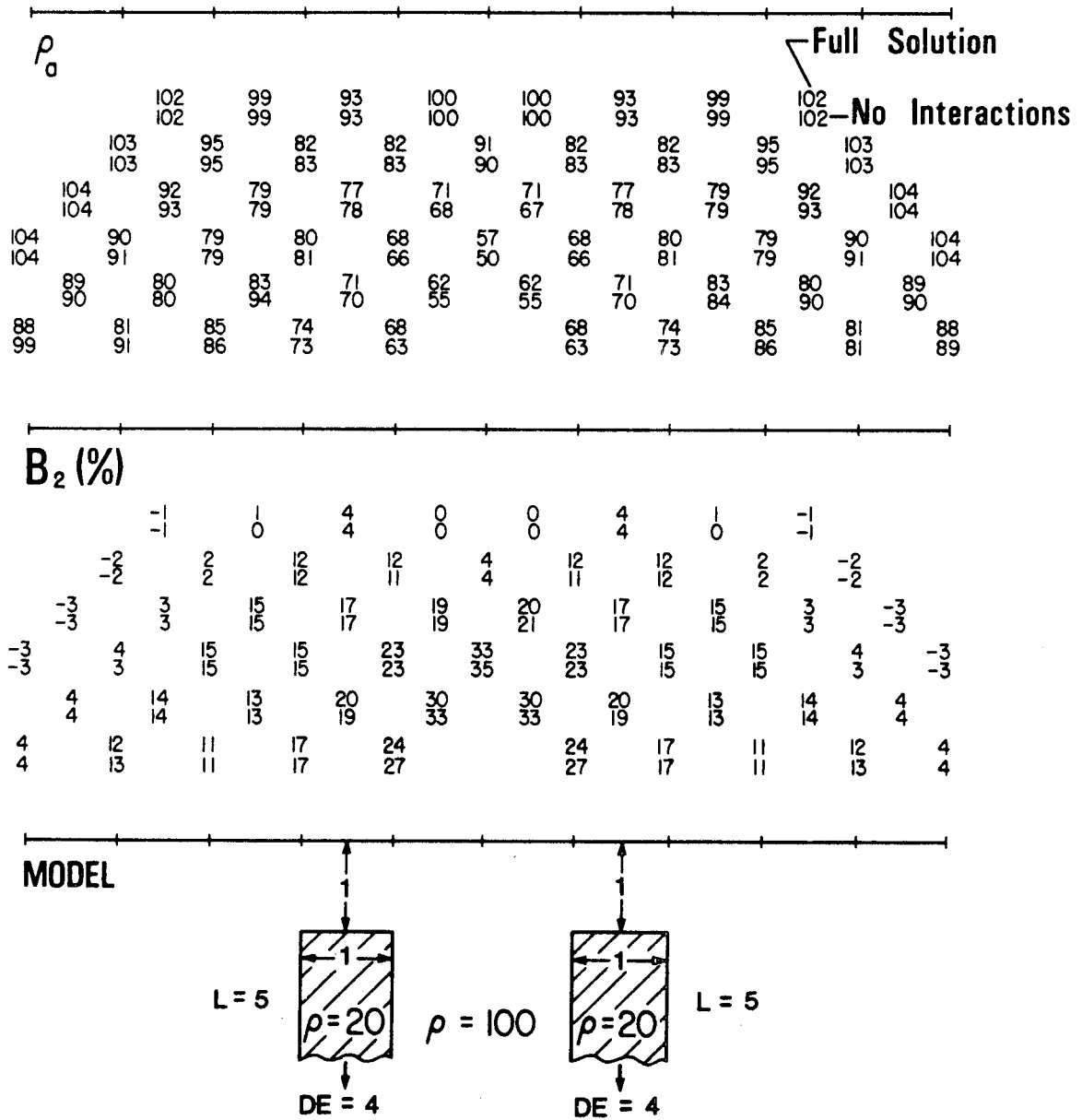
Figure 2 Comparison between Complete Solution

and Less Expensive

Solution Obtained by Ignoring Interactions

Electric Field Patterns in the Earth: Looking at IP in terms of my mathematical modeling technique provides a nice intuitive feeling for IP behavior. The measured potential is the sum of two potentials: incident and secondary. The incident potential is what would be measured over a homogeneous earth of resistivity ρ_1, while the secondary potential represents the contribution from the inhomogeneity. The secondary potential consists of in-phase and quadrature components; they originate at polarization dipoles distributed throughout the body or, equivalenty, at surface charges on the body. The quadrature dipoles, as well as the in-phase dipoles for a conductive body, are oriented in roughly the same direction as the incident field. For a resistive body, the in-phase dipoles are oriented in the opposite direction.

To illustrate, Figure 3 shows the quadrature electric field (current) pattern in a cross section of the earth through the center of a 1 x 1 x 5 body. A corresponding pseudosection is shown; the bold numbers correspond to the particular transmitter dipole to which the electric field pattern pertains. The contoured numbers in the cross section are total electric field phase; i.e., total quadrature field divided by total in-phase field. In this case the in-phase field is the homogeneous earth field, because there is no resistivity contrast. Because the intrinsic IP response of the body is 100 milliradians (mils), the numbers are $B_2(\%)$. The solid arrows show the quadrature field direction, while the broken arrows show the in-phase field direction.

The dipole-dipole array measures the component of electric field along the line. By convention, the IP response is positive when the quadrature (polarization) and in-phase fields are in opposite directions, and negative

PSEUDO SECTION

| 6 | 5 | 4 | 3 | 2 | I | 1 | 2 | 3 | 4 | 5 | 6 |

```
         0    -I   -I    I6    I6   -I   -I     0
     -I   -2    I    23    20    23    I   -2   -I
  -I   -3    3    23    IO    IO    24    3   -3   -I
-I   -3    4    23    4     0    4    23    4   -3   -I
   -4    6    22    2    -3   -3    2    22    6   -4
      7   2I    0   -4   -5   -4    0   2I    7
```

EARTH CROSS SECTION

| 6 | 5 | 4 | 3 | 2 | I | 1 | 2 | 3 | 4 | 5 | 6 |
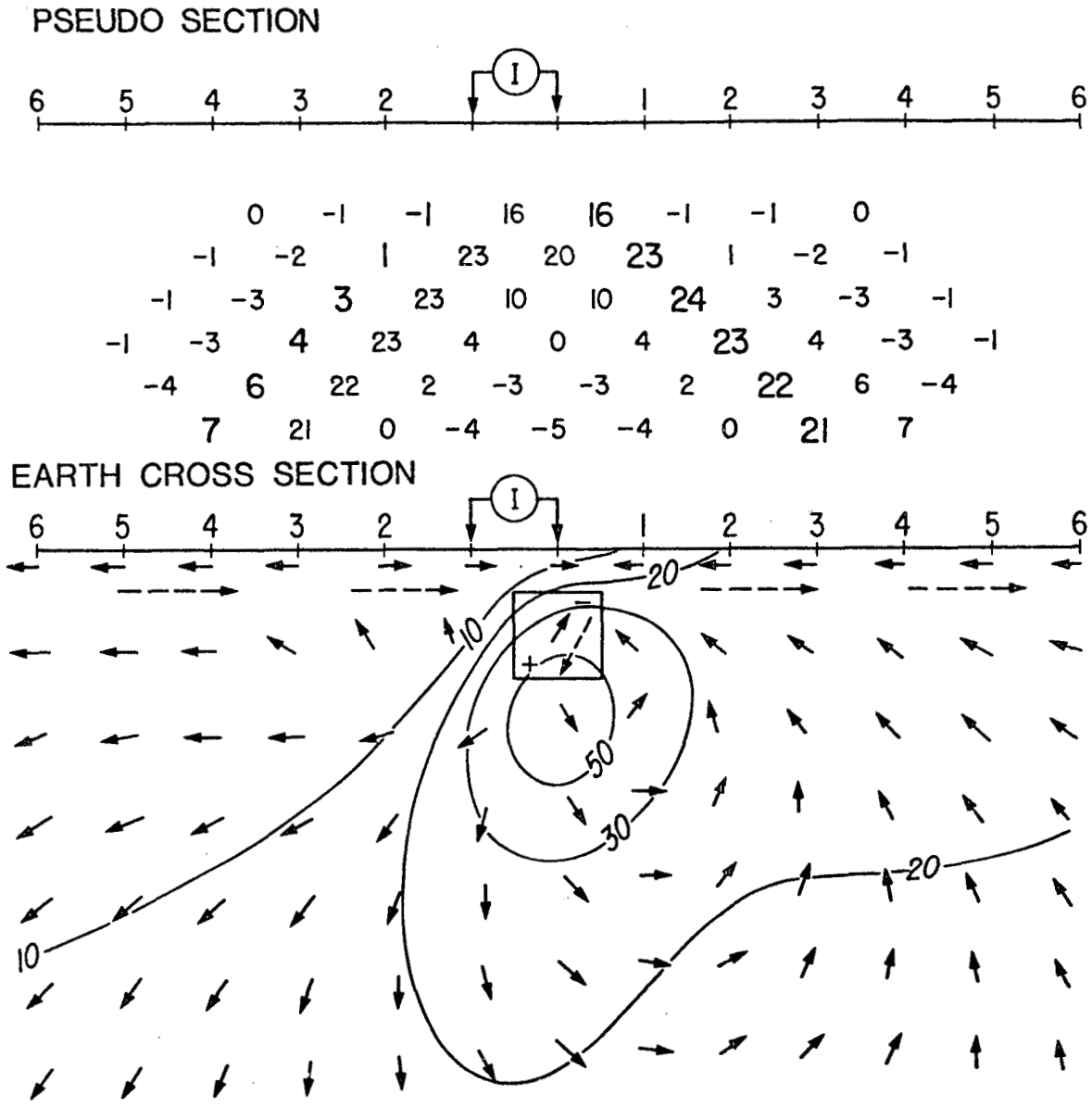
Figure 3. Total Electric Field IP Response (B$_2$%) and Quadrature Field Direction in the Earth for 1 x 1 x 5 Body with No Resistivity Contrast. Large Numbers in Pseudosection are IP Response for the Transmitter Dipole Considered. Broken Arrows Show Direction of Primary Field.

when they are in the same direction. For the transmitter dipole of Figure 3, there is only one negative IP response: -1 mil when the receiver is at 2-3 to the left. That is where the quadrature field changes direction. The quadrature current is in the same direction everywhere to the right of the body, producing a relatively uniform IP response of 20 mils. Note the positions of positive and negative surface charges, from which the quadrature field originates.

Bipole-dipole models: Apparent resistivity patterns resulting from bipole-dipole electrical surveys are frequently complex and difficult to interpret intuitively. To gain insight into the interpretation of bipole-dipole data in geothermal prospecting we have computed a library of model results for simple prisms.

In addition, we are using the program interactively to interpret field data from geothermal areas. To illustrate the complexities that can be considered, Figure 4 shows theoretical results for a complicated hypothetical geothermal model. The shaded blocks represent resistive portions of the system, both internal and external to the conductive body. Geologically, the resistive portions might be due to rock type changes, silicified zones, or vapor-filled rock pores. A salient extending from the main mass might represent a fracture zone. Our computer cost for this model was $11.75, at night rates on the University of Utah Univac 1108 computer.

Downhole-electrode models: As exploration focuses on deeper targets, drill hole geophysical techniques become more important. Surface IP surveys face

COMPLICATED GEOTHERMAL MODEL --APPARENT RESISTIVITY

PLAN VIEW

SCALE: 1 UNIT

TRANSMITTER POSITION (X,Y,Z)

9.00	9.75	1.00
9.00	8.25	1.00
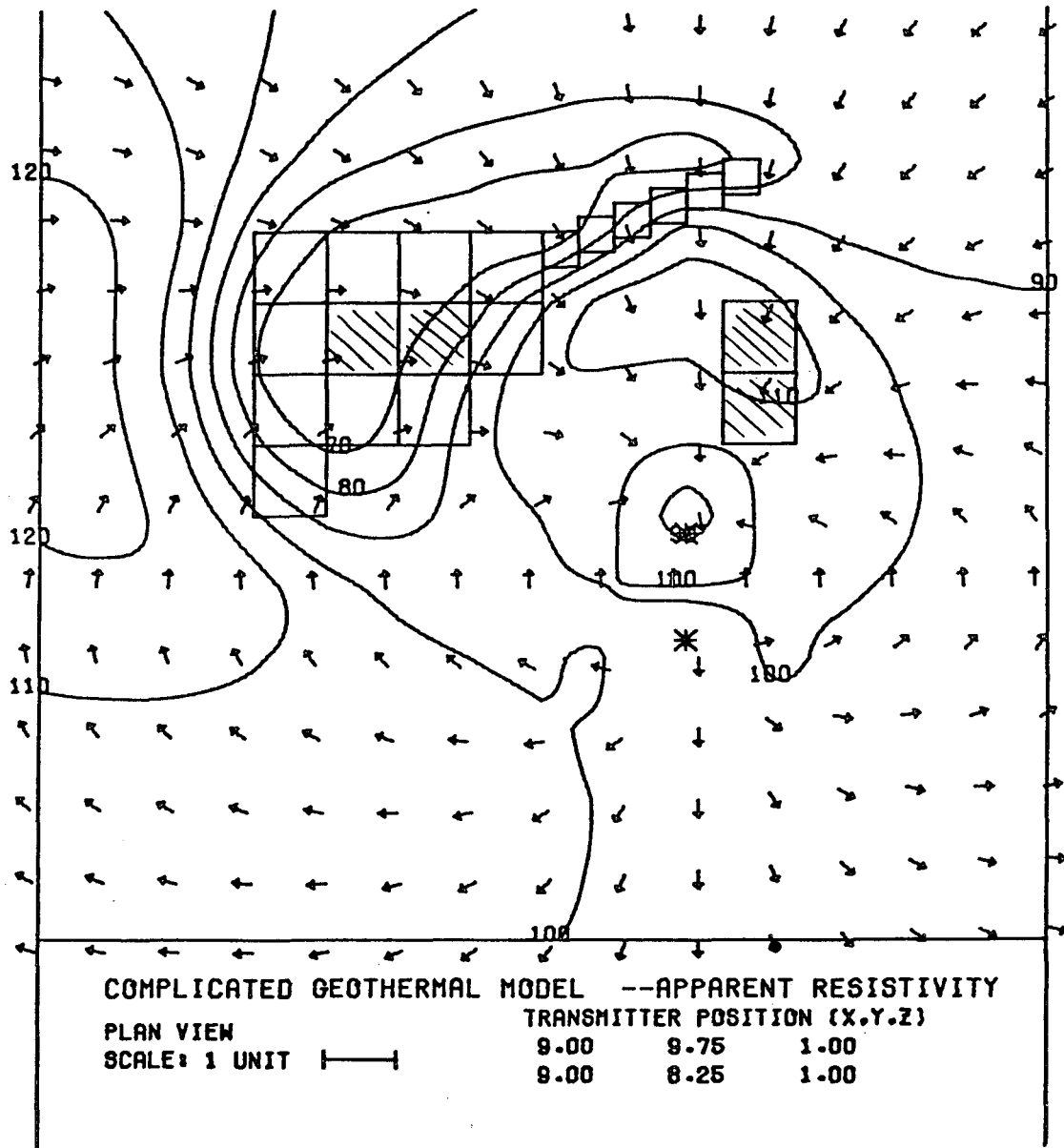
Figure 4

Bipole – dipole apparent resistivity for a complicated Model.
Background resistivity 100; shaded blocks 1000; large unshaded
blocks 10; small blocks 5.

fundamental limitations in depth of exploration. These limitations can be circumvented, however, by placing a transmitter electrode in a drill hole. Numerical modeling results in Figure 5 illustrate the increase in IP response as a transmitter electrode is lowered in a drill hole near a responsive, conductive ($\rho_2/\rho_1 = 0.1$) 1 x 3 x 3 body. These results pertain to total field measurements with short, orthogonal dipoles at the surface of the earth, and are shown in plan view. The arrows show the direction of the quadrature (IP) field, which originates at charges on the surface of the body.

When the electrode is at the surface of the earth, the IP response is negligible. However, the response is amplified considerably as the electrode approaches the depth of the body. It is easy to miss a small body in a drilling program; a drill hole IP survey could mean the difference between success and failure. Measurements also can be made in a drill hole with the transmitter electrode on the surface or in another drill hole. If a drill hole intersects a sulfide zone, measurements with an electrode in the zone can determine the direction of increasing mineralization. All of these drill hole methods can be evaluated via numerical modeling.

Magnetic IP: Evaluating new techniques such as magnetic IP is an important use of numerical modeling. Figure 6, for example, compares electric (conventional) IP and magnetic IP for a conductive prism in an otherwise homogeneous earth. The prism dimensions are 100 m x 400 m x 500 m (W x DE x L), at 100 meters depth. The transmitter is a 100-meter grounded wire, oriented perpendicular to the line. The results are shown in pseudosection form, except that
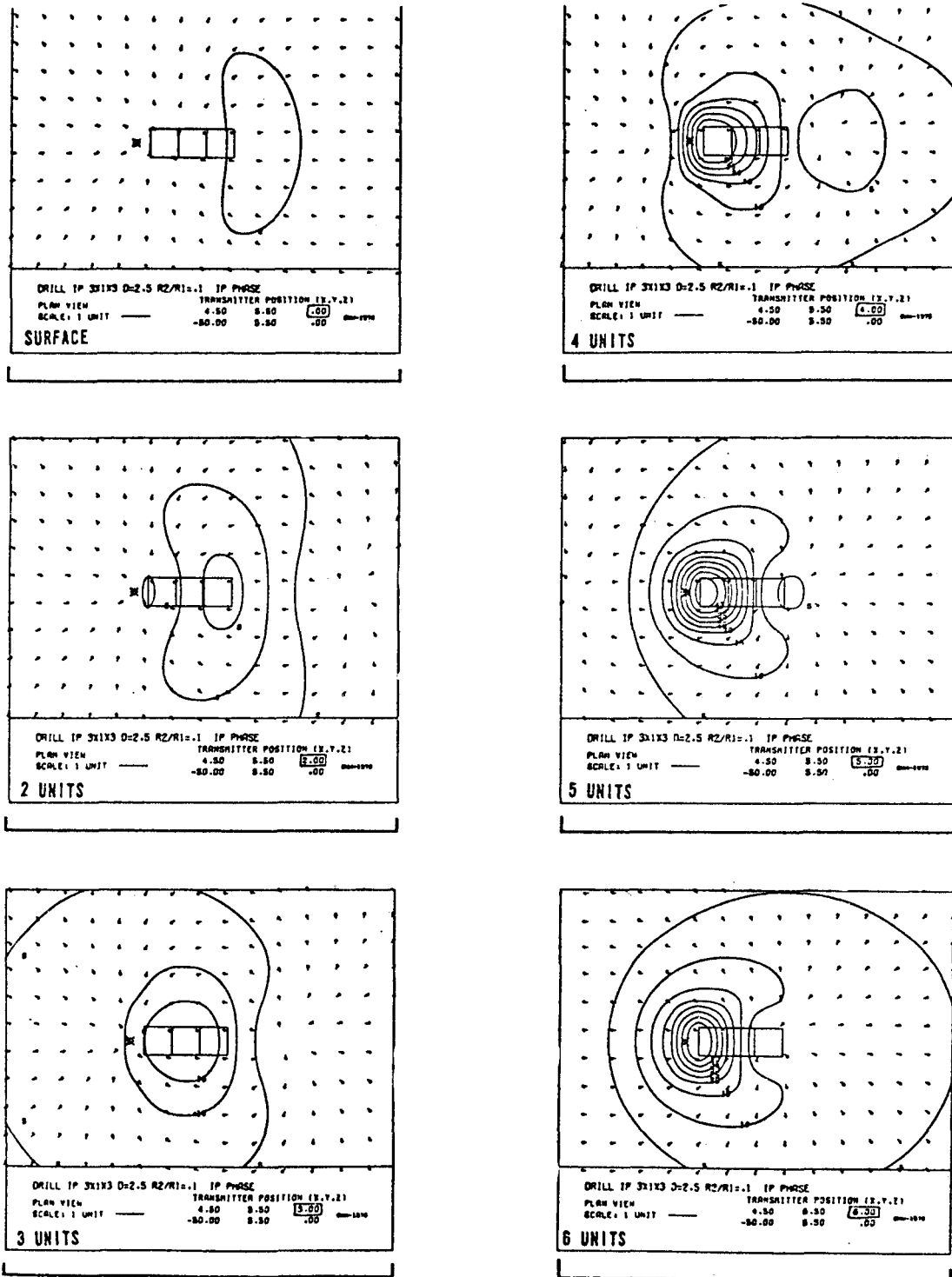
Figure 5

Surface I.P. Responce (B₂%) of a Small Deep Sulfide Body Excited by Downhole Electrodes at Depths of 0, 2, 3, 4, 5, 6 Units. Depth to Top of Body is 2.5 Units. Arrows Show

Electric Field IP Response

B_2 (%)

0	0	1	4	11	11	5	1	0	
0	1	2	7	16	20	18	8	3	1
1	3	9	18	21	22	21	11	4	1
4	10	18	21	22	23	24	14	5	2
11	19	20	20	21	24	25	16	6	
18	19	18	18	20	23	26	17	7	

Magnetic Field IP Response

B_2 (%)

0	1	2	3	6	7	5	2	1	
1	1	2	5	7	10	11	8	4	2
1	3	5	8	11	13	15	11	5	3
3	5	8	10	13	16	18	13	7	3
5	8	10	12	14	17	20	15	8	
7	9	10	12	14	19	22	17	9	

Model

100 m

100 m

L = 500 m

10 Ωm

100 Ωm

DE = 400 m
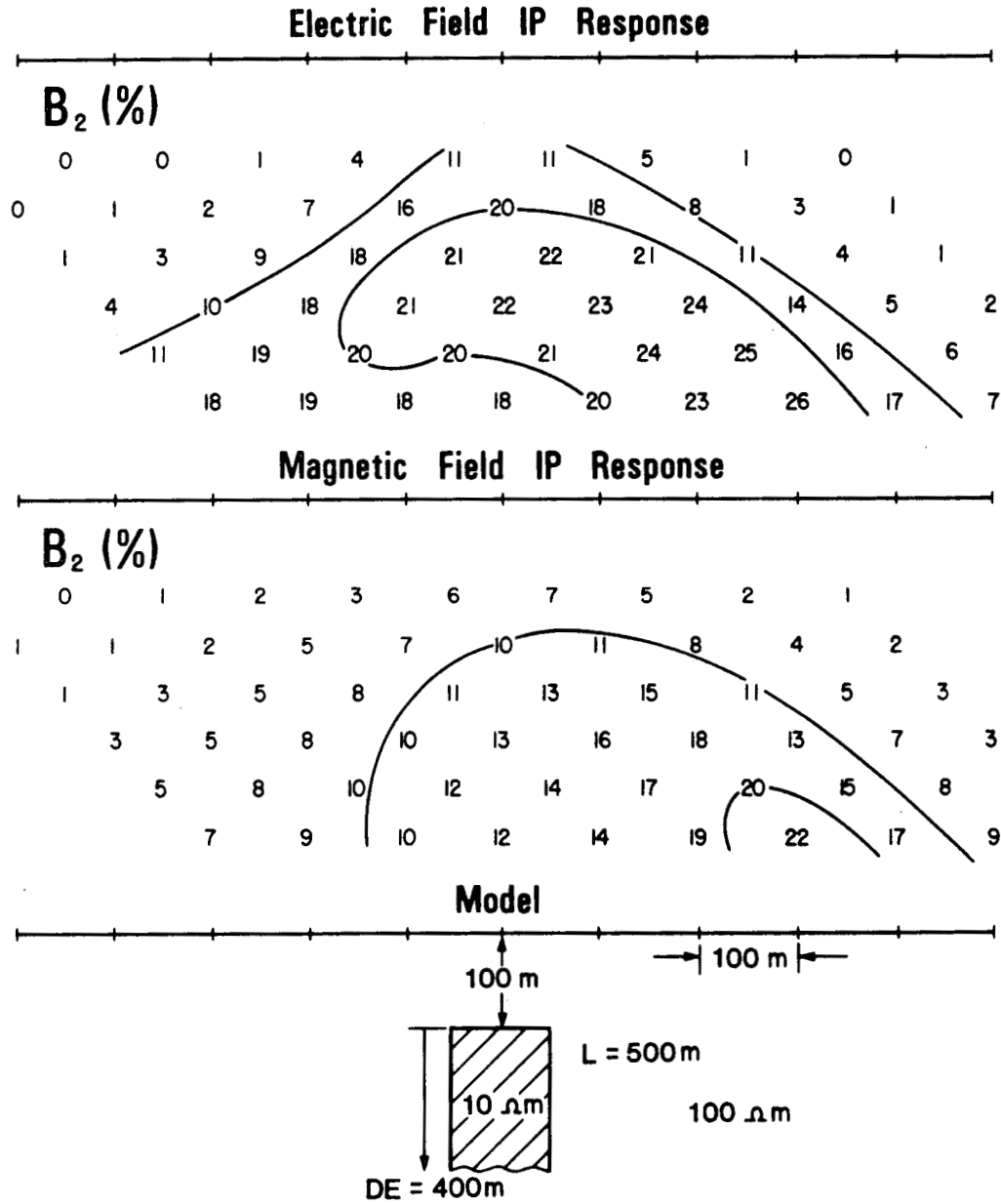
Figure 6

Comparison between Conventional and Magnetic IP. Point Measurements with Transmitter Dipole Perpendicular to Line

the transmitter and receiver (point measurements for E and H) are located
halfway between the station numbers shown. The transmitter is to the left
for each calculation; because reciprocity does not apply, the results are
not symmetric.

For this case, magnetic IP response is smaller than conventional IP
response. In fact, for all cases I have studied - resistive and conduc-
tive bodies at different depths in an otherwise homogeneous earth -- the
magnetic IP response always is smaller. I have not yet studied the effect of
conductive overburden on magnetic IP response, an obvious area for further
research. The possibilities for airborne IP also should be investigated via
numerical modeling.

<div align="center">CONTROLLED SOURCE EM</div>

Controlled-source EM results have been generally disappointing. Be-
cause of computer storage limitations, not enough cells can be used to
simulate accurately the EM response of a massive sulfide body. Although
incorporating the integro-difference approach improves the accuracy some-
what, the solution still is not very useful for massive sulfide modeling.

Figure 7 illustrates the lack of convergence for horizontal loop EM.
The in-phase and quadrature responses, in percent of primary free-space
response, are shown for a number of transmitter-receiver configurations,
in pseudosection format. Results are shown for two discretization levels:
1 x 4 x 3 - 12 cells, and 2 x 8 x 6 - 96 cells. The quadrature response
seems to be close to convergence, but the in-phase values are much different

96 Cells

12 Cells

R (%)

```
-1    -1    -1    -1    -1    -1    -1
-1    -1    -1    -1    -1    -1    -1
   -3   -3    4    8    4   -3   -3
   -2   -2   -2    4    2   -2   -2
      -4    5   13   13    5   -4   -4
      -3    3    9    8    3   -3   -4
         7   17   18   17    7   -5      -6
         5   11   13   11    5      -4   -5
            19   22   22   19    9   -6      8
            14   16   16   14    6   -6      -7
               24   24   24   22   10   -8
               19   19   19   17    8   -7
```

I (%)

```
-1    -1     2    1    1   -2   -1
-1    -1    -2   -1   -1   -2   -1
   -3   -3    4    8    4   -3   -3
   -2   -3    3    8    3   -3   -2
      -4    5   13   13    5   -4   -4
      -4    5   13   13    5   -4   -3
         7   17   18   17    7   -5      -5
         6   15   18   15    6   -5      -4
            19   22   22   19    9   -5      -5
            17   19   19   17    7   -5      -5
               24   24   24   22   10   -5
               19   19   19   17    7   -5
```

Model

$\rho = 100$

$f = 1000$

30m

30 x 120 x 90m

$\rho = 1$
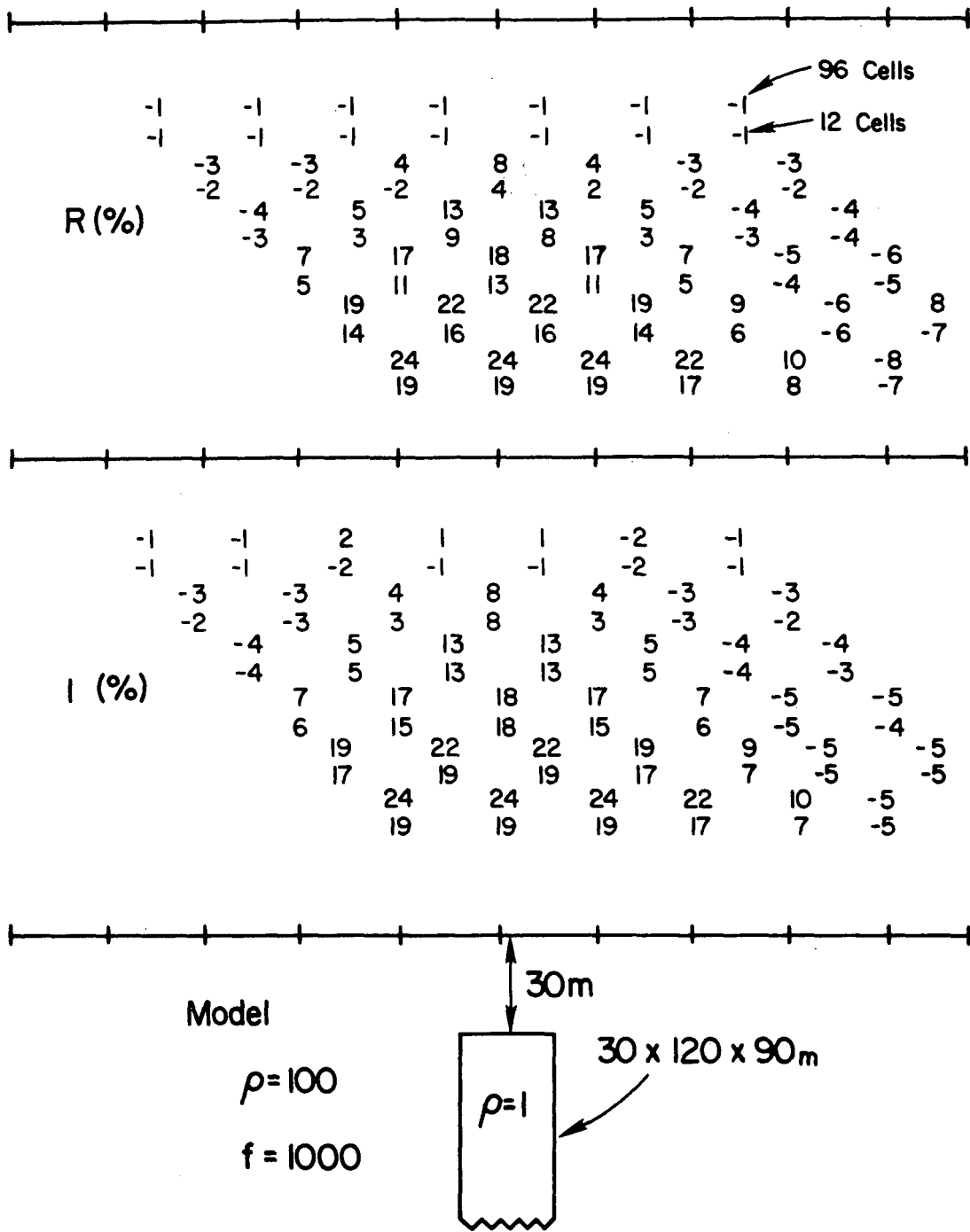
Figure 7   Convergence for Horizontal Loop EM

for the two cell sizes. This lack of convergence is not surprising, because the larger cells are two skin depths (in the body) across, while the smaller cells are one skin depth across. We should not expect the electric field to be well approximated by a constant over such distances. Results are worse, of course, for higher frequencies and higher conductivities.

We have checked horizontal loop calculations with the finite element results of Pridmore (1978) and with Frishknecht's (p.c.) scale model results, and obtain reasonable comparisons at low conductivity contrasts ($\lesssim$30). In comparison with Frishknecht's results, we obtain a smooth peak over a shallow body rather than his double peak, probably due to the cells being too large for this shallow body.

EM Coupling: Electromagnetic (EM) coupling can be a serious problem in IP surveying. Eddy currents are created in the ground to oppose changes in the electric and magnetic fields generated by the IP transmitter. These eddy currents vary with frequency, and their effects are similar to those of a polarizable body. We have calculated EM coupling for a number of three-dimensional models. Unfortunately, there are no other published cases to provide a cross check, but our results appear to be reasonable. The program predicts the negative coupling encountered in the field over very conductive bodies.

Figure 8, for example, shows theoretical EM coupling phase over a 2000' x 3000' x 6000' (W x DE x L) prism at a depth of 1000'. Its resistivity is one ohm-meter, and the background resistivity is 100 ohm-meters; the prism has no IP response. The dipole length is 1000 feet. Results are shown for three frequencies: 1.0 Hz, 0.5 Hz, and 0.1 Hz. For comparison, EM coupling

EM COUPLING

Phase (mrad)

f = 1.0 hz   Half-space
                                                                              Value

6	5	2	2	5	6		5
15	12	6	4	6	12	15	13
26	21	14	18	18	15	21	26	23
39	31	26	41	48	41	26	31	39	36
53	42	39	63	70	70	63	39	42	53	50
68	56	53	82	89	89	89	82	53	56	60

f = 0.5 hz

3	3	1	1	3	3		3
8	6	4	3	4	6	8	7
14	11	9	11	11	9	11	14	12
20	17	16	24	26	24	16	17	20	19
28	23	24	36	39	39	36	24	23	28	27
37	31	33	47	49	49	49	47	33	31	37

f = 0.1 hz

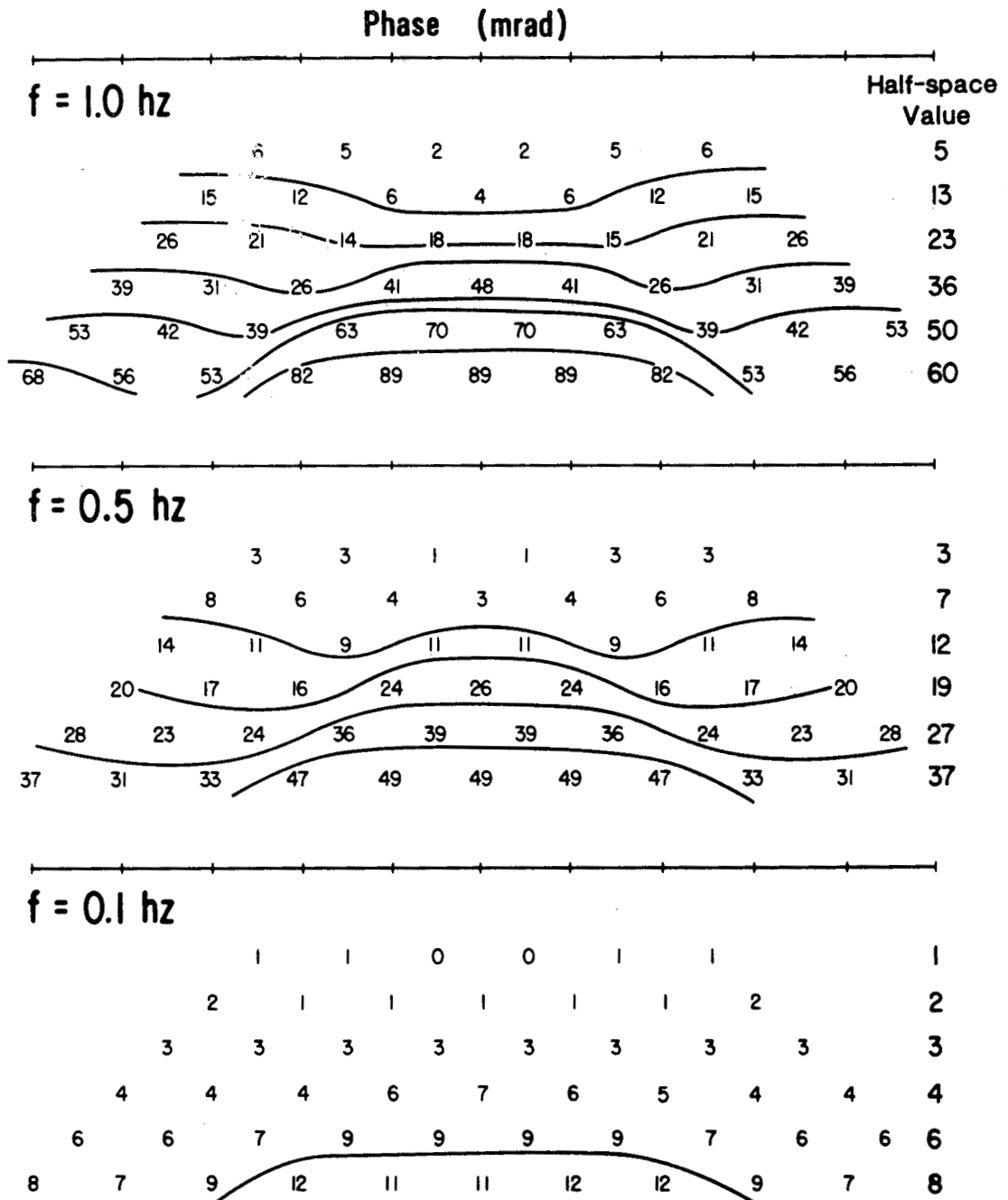| 1	1	0	0	1	1		1
2	1	1	1	1	1	2	2
3	3	3	3	3	3	3	3	3
4	4	4	6	7	6	5	4	4	4
6	6	7	9	9	9	9	7	6	6	6
8	7	9	12	11	11	12	12	9	7	8

Figure 8

EM Coupling for Three-dimensional Model; W=2000 ft,
DE = 3000 ft, L = 6000 ft, D = 1000 ft, $\rho_2 = 1$ ohm-m,
$\rho_1 = 100$ ohm-m

values for a homogeneous half-space of resistivity 100 ohm-meters are shown at the side. EM coupling is greater than half-space coupling when the transmitter and receiver straddle the body at large separations. However, there are areas in the pseudosection where coupling due to the prism is negative, i.e., less than half-space coupling.

MAGNETOTELLURIC MODELING

The MT source field is a vertically propagating plane wave impinging on the surface of the earth. Hence for a simple prismatic model there are two vertical symmetry planes passing through the center of the body, and it is only necessary to solve for one-fourth of the total number of unknowns.

Unfortunately, the new matrix is not symmetric as in the general case for equal-conductivity and equal-size cells. Even so, the computer storage and computation time are reduced considerably for the MT problem. Without symmetry planes, $3N(3N + 1)/2 \approx 9N^2/2$ storage locations are required, where N is the number of cells. With two symmetry planes, the storage requirement is $\frac{3N}{4} \times \frac{3N}{4} = \frac{9N^2}{16}$, less by a factor of 8.

Figure 9 illustrates the reduction in computer time for a two-symmetry-plane problem compared to one with no symmetry. In each case, forming and factoring (LU decomposition) the matrix account for most of the computer time. Matrix factorization time is less by a factor of about 35 when symmetry is invoked. Also, the time required to form the matrix is less for the symmetric problem, because only one-fourth of the matrix elements need to be computed.
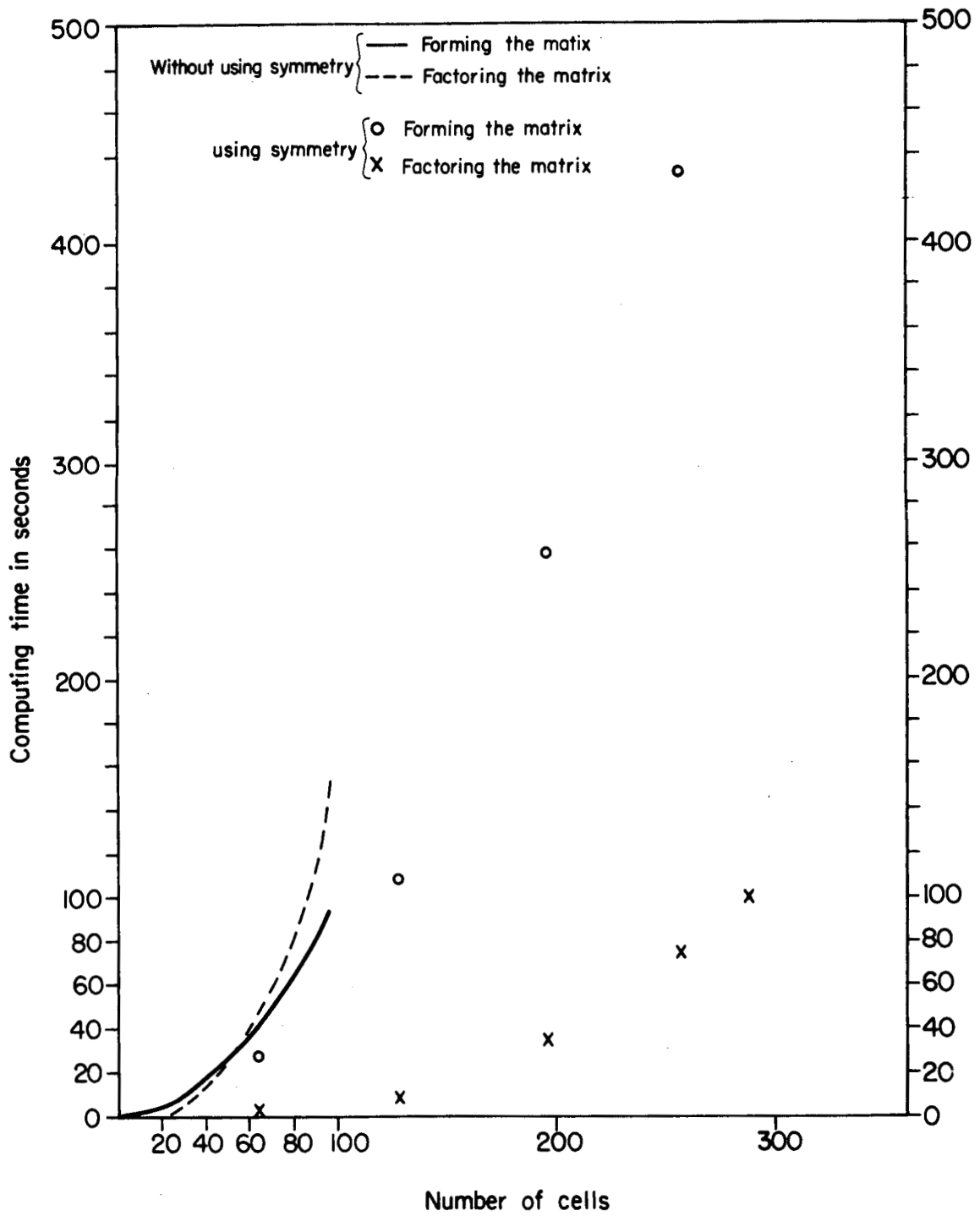
Figure 9 Reduction in Computer Time for Problem with Two Symmetry Planes.

In the general case a maximum of 120 cells can be used on the University
of Utah Univac 1108 computer, but for the symmetric problem the limitation
is 340 cells. This increase in the number of cells permits the use of smaller
cells for more accuracy, or, alternatively, the modeling of larger bodies.

Solution Checks

Unfortunately, the only other published 3D MT results are those of Jones
(1974), Weidelt (1975), and Reddy, et al., (1977), all for outcropping bodies
which we cannot model accurately. However, comparisons with Meyer (1976)
and Pridmore (1978) for controlled-source EM, comparisons with other solutions
for zero frequency (Hohmann, 1975), and comparisons with 2D models discussed
later in this paper lend credence to our results. Also, the general behavior
of the 3D MT results is as expected.

The body that we have used to check convergence is shown in Figure 10.
It is a 1 km x 2 km x 2 km conductive prism at 1 km depth, and is elongated
in the y direction. We have checked convergence at points A, B, and C at
four frequencies, and at three different discretizations: 1x2x2 = 4 cells,
2x4x4 = 32 cells, and 4x8x8 =256 cells. The cell sizes for these three
cases are 1 km, 0.5 km, and 0.25 km, respectively. The two excitation modes -
E_{11} and $E_\perp$ - are illustrated in Fig. 10a. For E_{11} excitation the incident
electric field is parallel to the long axis of the body, while for $E_\perp$ excita-
tion, the incident electric field is perpendicular to the long axis.

Figure 11 shows the convergence as a function of frequency at point A
for the E_{11} mode. Results are given in terms of apparent resistivity (ρ_{yx})
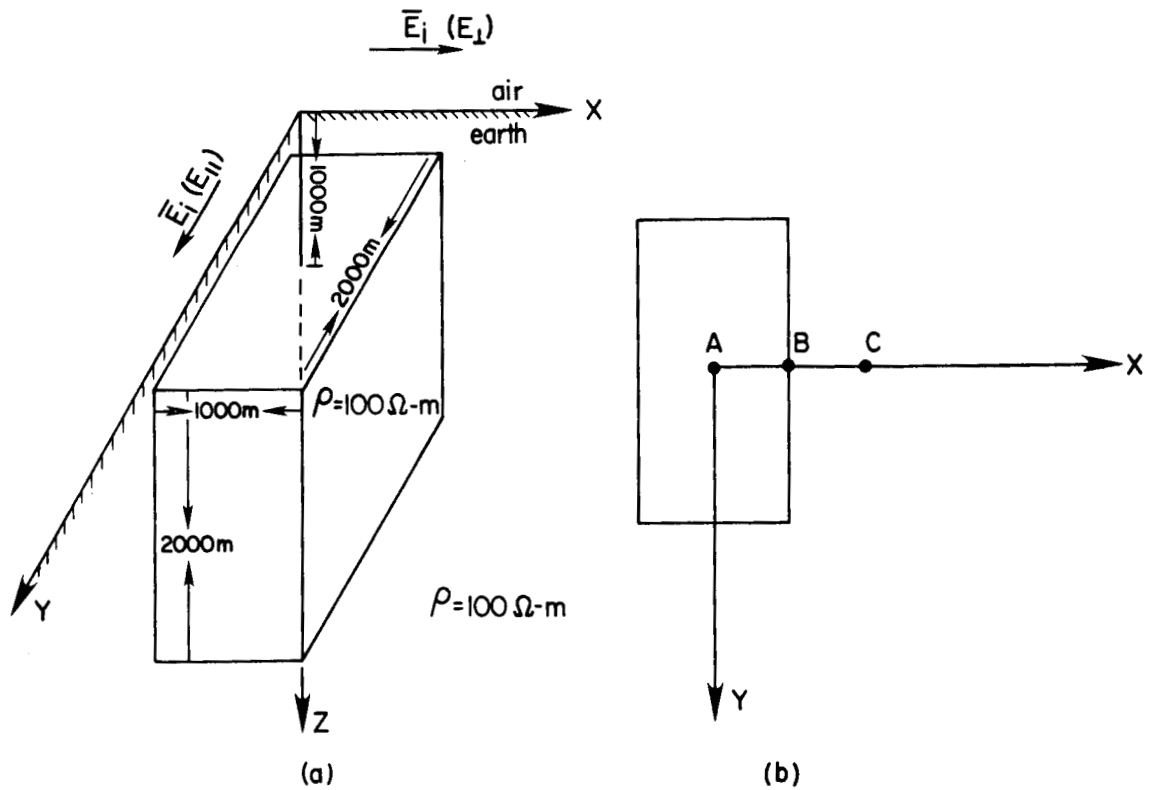
Figure 10 (a.) Three dimensional Model for Convergence Checks.

(b.) Plan View Showing the Three Observation Points on the Surface of the Earth.

and phase (E_y phase - H_x phase). The solution is convergent, and, as expected, smaller cells are required to represent the current at the higher frequencies.

At 10 Hz the cell sizes represented in Figure 11 are 2.8, 1.4, and 0.7 skin depths in the body. At 1 Hz, where the solution has converged to the final result by the middle cell size, the cell sizes are 0.89, 0.44, 0.22 skin depths in the body. Thus it appears that the minimum cell size for accurate results in this case is about 0.5 skin depths. Of course, larger cells may be adequate for particular interpretation problems, and computations would be less expensive. Another cell-size criterion, which depends mainly on conductivity contrast and depth, is that the cells must be small enough to accurately represent the current even at very low frequencies, where the skin depth is large. As a rule of thumb, we require the cells to be no larger than the depth. As a result, computations for shallow bodies are expensive.

Convergence for $E_\perp$ excitation is a little faster, as illustrated in Figure 12.

The significance of these results is that we have been able to halve the cell size two times and demonstrate convergence for this particular integral equation solution. In our previous controlled-source modeling there were no symmetry planes, so that only two discretization levels were possible, and it was impossible to determine whether the solution is convergent, except in the simple zero-frequency case. Higher-order basis functions would yield the same accuracy with fewer unknowns, but they would be difficult to implement.
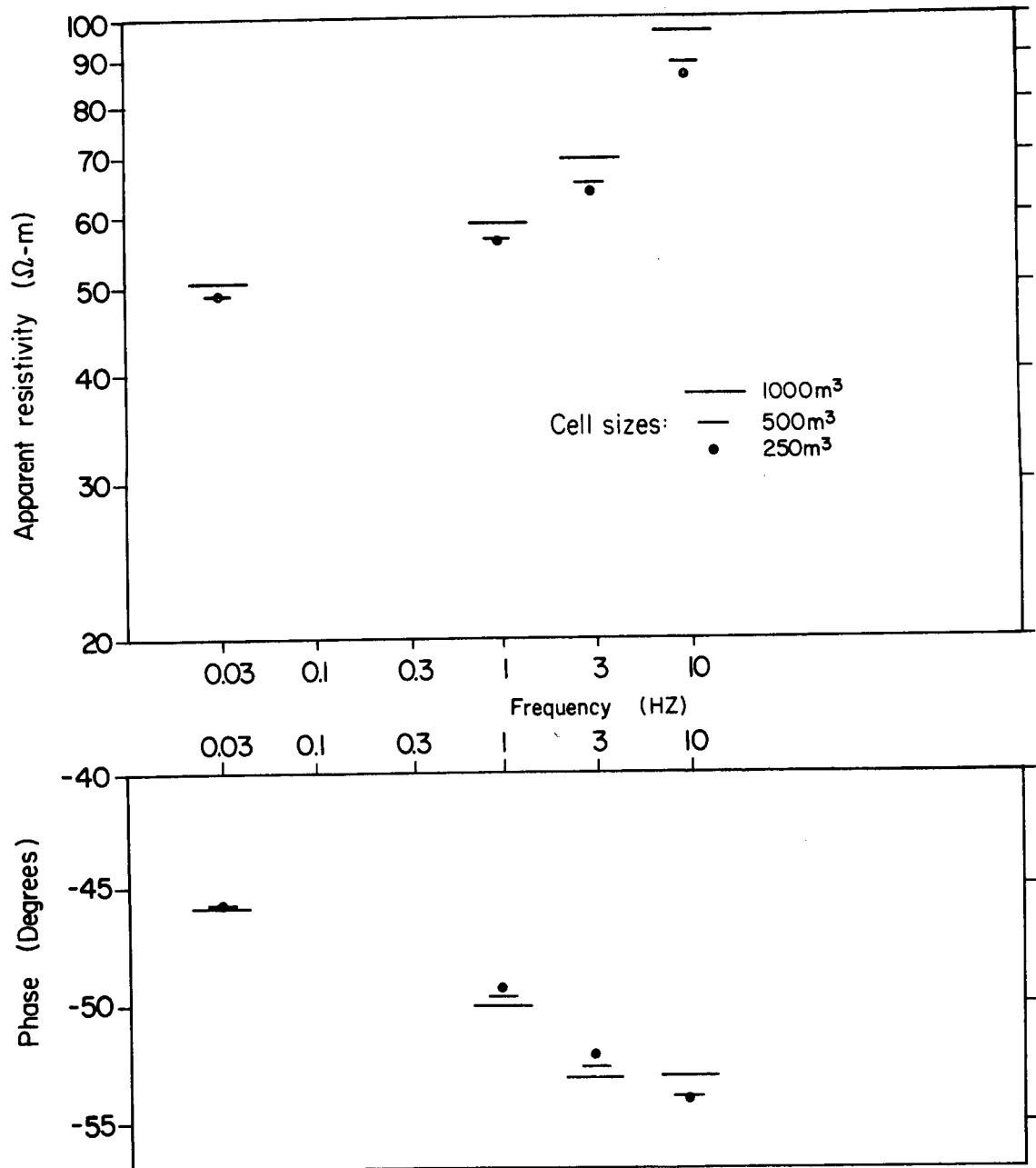
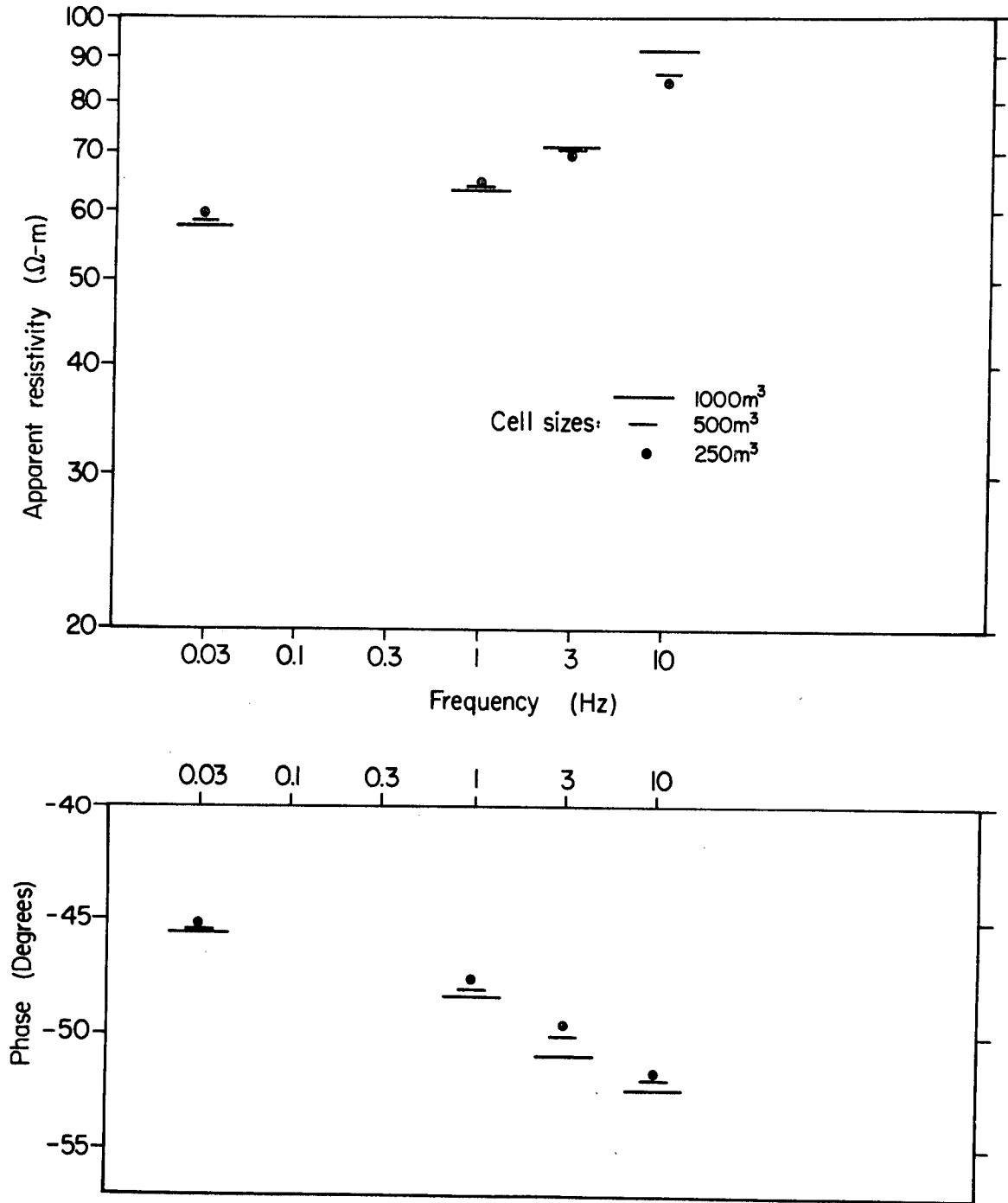Figure II   Convergence   at   Point   A   for E_{11} Excitation.

Figure 12 Convergence at Point A for $E_\perp$ Excitation.

COMPARISON WITH 2D MODELS

Another useful check, and one which is enlightening for MT interpretation, is comparison with 2D models. As the length of the 3D body increases, the fields should approach those of a 2D model. Figures 13 and 14 show comparisons between our 3D results and 2D results computed with Rijo's (1977) finite element algorithm.   The model is that of Figure 10, with variable strike length (2, 4, 8, ∞ km).

Figure 13 shows the comparison for E_{11} excitation, which corresponds to the 2D TE mode. Only E_y, H_x, and H_z components are present for the 2D model, but all five components - E_x, E_y, H_x, H_y, H_z - are present in the 3D case. Apparent resistivity(ρ_{yx}) and phase (E_y phase - H_x phase) are plotted against distance from the center of the body for the three strike lengths and for the 2D body.

Because there are no boundaries normal to current flow to generate space charges in the 2D TE case, whereas there are in the 3D model, the results are quite different. The difference is particularly great at 0.03 Hz. The secondary electric field due to polarization charge at the ends of the body is present even at zero frequency while that due to volume polarization current (the only source of secondary field in the 2D case) decreases with decreasing frequency. The secondary magnetic field, which is due only to volume polarization current, also has a frequency-independent component.

At 1 Hz and above, apparent resistivities for the 8 km-long 3D body are very close to those of the 2D model. Phase seems to converge to 2D values as the length is increased, but a body longer than 8 km would be required for good agreement.
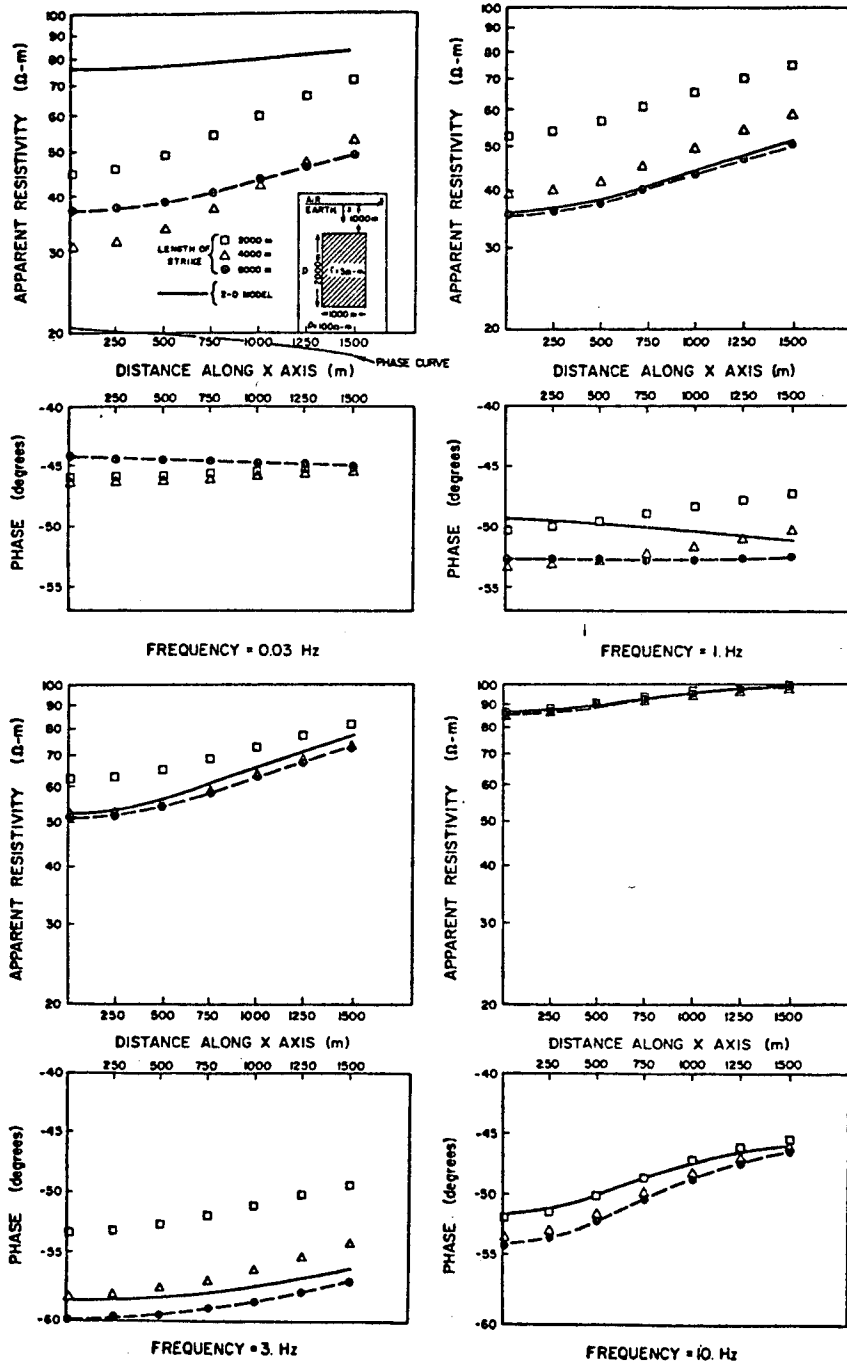
Figure 13 Comparison between 2D Results and 3D Results for Bodies of Different Length— $E_{\parallel}$ Excitation
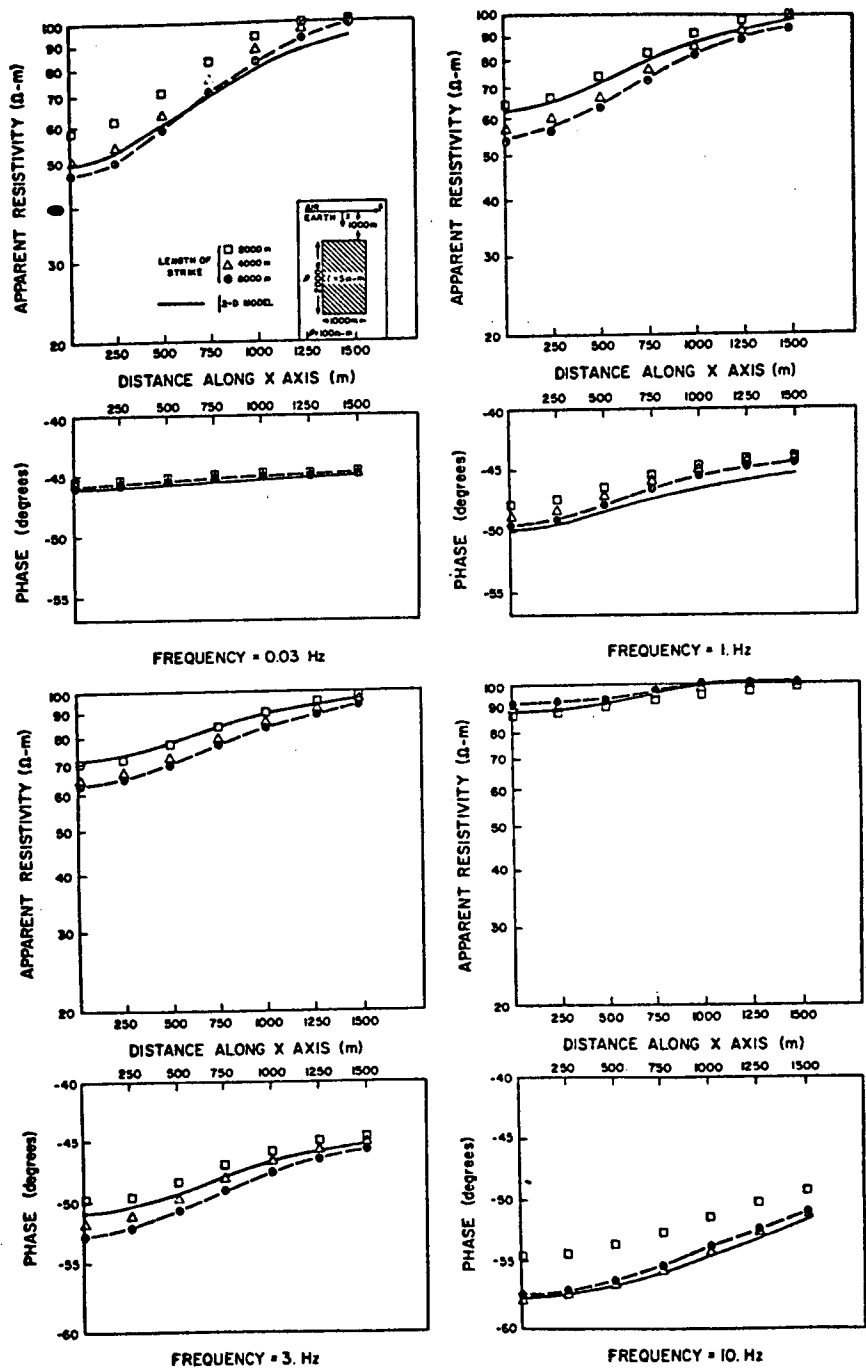
Figure 14 Comparison between 2D Results and 3D Results for Bodies of Different Length – E_1 Excitation

Comparisons between our 3D $E_\perp$ results and Rijo's 2D TM results are shown in Figure 14. Space charges are included implicitly in the 2D TM formulation, so that the two solutions do not diverge at low frequencies, as they do for E_{11} excitation. However, except at the highest frequency, the 3D solution seems to converge to values slightly different from those of the 2D solution as the length of the body increases. For example, the apparent resistivity amplitudes differ by as much as 15 percent at 1 Hz.

This discrepancy in the $E_\perp$ results could be due either to the 2D or 3D solution. While the accuracy of the 2D finite element TE results has been verified by cross checks with other numerical solutions (Hohmann, 1971; Swift, 1971), we noted some discrepancies in comparing the TM finite element results with those of Swift. This discrepancy is being investigated, but the comparison in Figure 14 is adequate to give us confidence in our 3D results.

REFERENCES

Harrington, R.F., 1968, Field computation by moment methods: New York, MacMillan Co.

Hohmann, G. W., 1971, Electromagnetic scattering by two-dimensional conductors in the earth: Ph.D. thesis, Univ. of Calif., Berkeley.

Hohmann, G. W., 1975, Three-dimensional induced polarization and electro-magnetic modeling; Geophysics, v. 40, no. 2, p. 309-324.

Hohmann, G. W., 1977, Numerical IP modeling: U. of Ariz., Proceedings, IP for Exploration Geologists and Geophysicists.

Hohmann, G. W. and Ting, S. C., 1978, Three-dimensional magnetotelluric modelling: Univ. of Utah, DOE/DGE Rpt.

Jones, F. W., 1974, The perturbation of geomagnetic fields by two-dimensional and three-dimensional conductivity inhomogeneities: Pure & Applied Phys., v. 112, p. 793-800.

Meyer, W. H., 1976, Computer modelling of electromagnetic prospecting methods: Ph.D. Thesis, Univ. of Calif., Berkeley.

Miller, E. K., and Deadrick, F. J., 1975, Some computational aspects of thin wire modeling in Numerical and asymptotic techniques in electromagnetics; R. Mittra, ed.: New York, Springer-Verlag.

Pridmore, D. F., 1978, Three-dimensional modeling of electric and electro-magnetic data using the finite element method: Ph.D. Thesis, Univ. of Utah.

Reddy, I. K., Rankin, D., and Phillips, R. J., 1977, Three-dimensional modeling in magnetotelluric and magnetic variational sounding: Geophys. J. R. Astr. Soc., v. 51, p. 313-325.

Rijo, L., 1977, Modeling of electric and electromagnetic data: Ph.D. Thesis, Univ. of Utah.

Swift, C. M., 1971, Theoretical magnetotelluric and Turam response from two-dimensional inhomogeneities: Geophysics, v. 36, p. 38-52.

Weidelt, P., 1975, Electromagnetic induction in three-dimensional structures: Geophys. J. R. Astr. Soc., v. 41, p. 85-109.

ACCURACY OF METHODS IN GEOPHYSICS MODELLING

Frank Stenger
Department of Mathematics
University of Utah

1.   INTRODUCTION

In this paper we discuss the methods of approximation that have been used
in this conference for the approximate solution of modelling problems, with
emphasis on the order of the methods, especially in the presence of singularities.
While all rates of convergence are given in terms of the order of the number of
points, these rates are nevertheless best possible with regards to order. Some
of the classical methods of approximation are found in Davis [2], the method
based on splines in Ahlberg, Nielson and Walsh [1]. The rate of convergence
of some of these methods are found in Timan [7]. The methods based on sinc
functions and their rates of convergence are found in Stenger [4,5,6], Lundin
and Stenger [3].

Let us briefly summarize the various results. Throughout, we assume that
we are approximating a quantity such as the electric field, by

$$(1.1) \qquad\qquad E \cong \sum_{i=1}^{n} E_i \phi_i$$

where the E_i are constants and the ϕ_i are functions, depending on the partic-
ular method of approximation that is being used. More specifically, the ϕ_i
take on one or products of the following forms:

  1.   Polynomials

  2.   Splines:
        (a) Piecewise constant
        (b) Chapeau
        (c) Cubic
        (d) Triangular or tetrahedronal, linear, or quadratic or cubic

3. Trigonometric functions

4. Sinc functions

These functions form the basis for the approximate methods used in modelling. All of these may be used for purposes of interpolating or approximating a function, or for numerical integration (we simply integrate exactly the interpolation or approximation rule). Finite difference methods are usually obtained by means of local approximation via Taylor's formula. The transmission line model is obtained if we make piecewise constant approximations in Maxwell's equation. All of the above functions may be used in Galerkin or moment methods.

Several of the above approximations are used for the approximate evaluation of transforms. The Fourier transforms is usually evaluated via the FFT method, which is obtained by termwise integration of the sinc approximation of f over $(-\infty, \infty)$, i.e.

$$(1.2) \qquad f(x) \cong \sum_{k=-N}^{N} f(kh) \; \frac{\sin\left[\frac{\pi}{h}(x-kh)\right]}{\frac{\pi}{h}(x-kh)}$$

$$(1.3) \qquad \int_{-\infty}^{\infty} e^{ixt} f(t)\, dt \cong \begin{cases} h \displaystyle\sum_{k=-N}^{N} e^{ikhx} \;, & |x| < \frac{\pi}{h} \\[2em] 0 \;, & |x| > \frac{\pi}{h} \end{cases}$$

The Hankel transform is usually evaluated by means of the FFT method. To evaluate the Hilbert transform we may approximate f on $(-\infty, \infty)$ by splines and then take the Hilbert transforms of the approximation, or else, we can take the exact Hilbert transform of the approximation (1.2), to get

$$(1.4) \qquad \frac{P.V.}{\pi i} \int_{-\infty}^{\infty} \frac{f(t)}{t-x} \, dt \cong i \sum_{k=-N}^{N} f(kh) \frac{\pi}{2h} (x-kh) \left[\frac{\sin \frac{\pi}{2h} (x-kh)}{\frac{\pi}{2h} (x-kh)} \right]^2$$

The Laplace transform may be accurately evaluated by means of the formula (based on sinc approximations)

$$(1.5) \qquad \int_{0}^{\infty} e^{-st} f(t) \, dt \cong h \sum_{k=-N}^{N} f(e^{kh}) \exp[kh - se^{kh}]$$

2. ERRORS OF THE APPROXIMATIONS

The errors that one makes in using various approximation schemes can be readily deduced by looking at the errors that one makes in (1) using any of the one-dimensional bases listed in the previous section. We state these, as well as the errors of simple 2 dimensional approximations. In the next section we shall examine the errors of some 3 dimensional approximations.

2.1 Error in Polynomial Approximation

Let ε_p denote the ellipse with foci at ± 1 and sum of semi-axes equal to p. Let f be analytic in ε_p, and set $M(p) = \max\limits_{z \in \varepsilon_p} |f(x)|$.
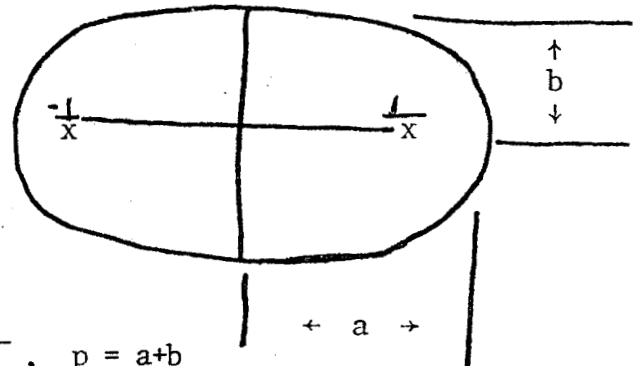
$$b = \sqrt{a^2 - 1} \,, \quad p = a + b$$

Then

$$(2.1) \quad \min_{P_n} \; \max_{-1 \le x \le 1} \; |f(x) - p_n(x)| \le \frac{4M(p)}{\pi p^{n+1}}$$

Thus the error of approximation of an analytic function with no singularities by a polynomial of degree n takes the form

$$(2.2) \quad error \; = \; O(e^{-cn})$$

2.2. Error of Approximation by Splines

(a) Piecewise Constant Approximation

$$(2.3) \quad f(x) \cong \sum_{i=1}^{n} f(\frac{2i-1}{2n}) \; X_i(x)$$

where

$$(2.4) \quad X_i(x) \; = \; \begin{cases} 1 & \text{if } \frac{i-1}{n} \le x < \frac{i}{n} \\ \\ 0 & \text{if } x \notin [\frac{i-1}{n}, \frac{i}{n}] \end{cases} .$$

The error of the approximation (2.3) is

$$(2.5) \quad error \; = \; O(\frac{1}{n})$$

provided that f is differentiable on $[0,1]$.

(b) "Chapeau" Spline

Let $S_i(x)$ be defined as in the figure, i.e.

$$(2.6) \quad S_i(x) \; = \;$$
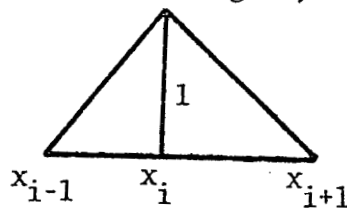
(2.7) $$f(x) \cong \sum_{i=0}^{n} f(\frac{i}{n}) S_i(x) \quad ,$$

where $x_i = \frac{i}{n}$. The error for two times differentiable functions on $[0,1]$ is

(2.8) $$\text{error} = O(\frac{1}{n^2})$$

(c) Cubic Spline

These approximations take the form

(2.9) $$f(x) \cong \sum_{i=1}^{n} [f(x_i)S_i^*(x) + f'(x_i)T_i(x))] \quad ,$$

where $x_i = i/n$, and where S_i^* and T_i are cubic polynomials. The error is

(2.10) $$\text{error} = O(\frac{1}{n^4})$$

for functions which are 4 times differentiable on $[0,1]$.

(d) Piecewise Linear Triangular Element

Assume that we approximate a function over a finite region in the plane, with n triangular patches, over each of which the approximation is linear. The length of an edge of the largest triangle is at least $O(\frac{1}{n^{1/2}})$, and the error, by (2.5) is at least $O((\frac{1}{n^{1/2}})^2)$, i.e.

(2.11) $$\text{error} = O(\frac{1}{n}) \quad .$$

Similarly, using n tetrahedra in 3 dimensional approximations, we get

(2.12) $$\text{error} = O(\frac{1}{n^{2/3}}) \quad .$$

2.3 Approximation by Trigonometric Functions

Let $R > 1$, and let A_R denote the annulus in the complex plane, located between the circles of radii $1/R$ and R .

Let f be analytic in A_R , and let

$$(2.13) \qquad \max_{z \in A_R} |f(z)| = M(R) \; .$$
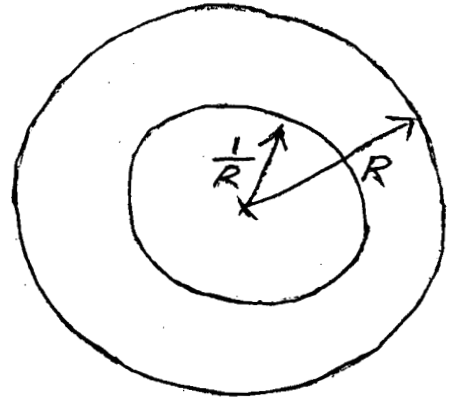
Set

$$(2.14) \qquad a_n = \frac{1}{2\pi} \int_0^{2\pi} f(e^{i\theta}) e^{-in\theta} d\theta \; , \; n = 0, \pm 1, \ldots \; .$$

Then

$$(2.15) \qquad \left| f(e^{i\vartheta}) - \sum_{k=-N}^{N} a_k \, e^{ik\theta} \right| \leq \frac{M(R)}{R^N} \; .$$

That is, the error of $n = 2N+1$ - term Fourier approximation satisfies

$$(2.16) \qquad \text{error} = O(e^{-cn}) \; .$$

2.4 Sinc Functions

Ex. Let $\mathcal{D}_d$ be the region in the figure whose boundary consists of
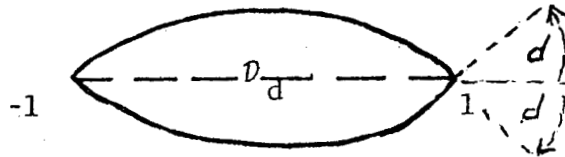
portions of circles, let f be analytic in $\mathcal{D}_d$, and on $(-1,1)$, let $|f(x)| \leq C(1-x^2)^\alpha$, $\alpha > 0$, $C > 0$. Then take $\phi(x) = \log\left(\frac{1+x}{1-x}\right)$, $x_k = \tanh(kh/2)$, $h = O(1/N^{1/2})$, $n = 2N+1$. This yields

$$(2.17) \qquad f(x) - \sum_{k=-N}^{N} f(x_k) \frac{\sin \frac{\pi}{h}[\phi(x)-kh]}{\frac{\pi}{h}[\phi(x)-kh]} = O(e^{-cn^{1/2}}), \ -1 \leq x \leq 1 \ .$$

Next, let us briefly discuss what happens to the above rates of convergence if singularities are present. Through this section, let α be a positive constant, such that $0 < \alpha < 1$. At the outset, we consider singularities at an endpoint of an interval.

Ex. 2.1. Polynomials. Let p_n be a polynomial of degree $\leq n$. Then

$$(2.18) \qquad \min_{p_n} \ \max_{-1 \leq x \leq 1} \ |(1-x)^{\alpha}(1+x) - p_n(x)| \ = \ O(\frac{1}{n^{\alpha}})$$

Ex. 2.2. Splines. All n-point approximations of $(1-x)^{\alpha}(1+x)$ by splines on $[-1,1]$ have errors $O(\frac{1}{n^{\alpha}})$.

Ex. 2.3. Trigonometric Functions. The Fourier polynomial approximation of $(1-x)^{\alpha}(1+x)$ on $[-1,1]$ satisfies

$$(1-x)^{\alpha}(1+x) - \sum_{k=-N}^{N} a_k e^{ik\pi x} = O(\frac{1}{n^{\alpha}}) \ , \quad n = 2N+1 \ .$$

Ex. 2.4. Sinc Functions. The order of convergence of approximation of $f(x) = (1-x)^{\alpha}(1+x)$ on $[-1,1]$ is given by (2.17).

Notice that sinc functions are the only ones not affected by the occurence of singularities at endpoints of an interval, and that there is a drastic change of order for the case of polynomials and trigonometric functions, depending on whether or not singularities are present.

If singularities occur in the interior of an interval, such as, for the case of the approximation of $|x|^{\alpha}(1-x^2)$ on $[-1,1]$, then the order of convergence for the various cases of approximation are respectively the same as

those given in Ex. 2.1, Ex. 2.2 and Ex. 2.3. However, the order of convergence

for the case of approximation of this function by sinc functions is then reduced

also to $O(n^{-\alpha})$, n = 2N+1 . It is thus important to know where singularities

occur. More will be said about this later.

3. ORDERS OF CONVERGENCE OF METHODS

The rate of convergence of methods is generally the same as the order to

which we can approximate a function. A slight difference occurs for the case

of quadratures, where, in e.g. one dimension the error is smaller by a factor

of 1/n . Whereas the order of convergence of n-point one-dimensional methods

is $O(\phi(n))$, the order of convergence of the corresponding n-point three

dimensional methods is $O(\phi(n^{1/3}))$. The orders of convergence for the various

methods of approximation are summarized in the tables which follow.

The tables show that there may be drastic changes in the orders of convergence,

depending on the methods of approximation that are being used, so that it can

be valuable to know when singularities occur. For the case of linear problems

singularities occur wherever the coefficients of the equation cease to be

analytic. For example, for the case of Maxwell's equations, the solutions are

analytic in each variable, wherever the coefficients are analytic in that variable.

Thus singularities occur wherever the conductivity changes abruptly, and wherever

the boundary of the region has corners and wherever the data of the problem has

singularities. Although we can determine where the singularities occur, it is

usually not possible to determine the explicit nature of the singularities. In

this latter case no method can converge faster than the sinc methods [6].

ORDER OF CONVERGENCE IN THE PRESENCE OF

METHODS	TOOLS	NO SINGULARITIES	SINGULARITIES
Interpolation Quadrature	Polynomials	$O(e^{-cn^{1/3}})$	$O(n^{-\alpha})$
	Splines	$O(n^{-a})$	$O(n^{-\alpha})$
Galerkin or Moment Methods	Trigonometric functions	$O(e^{-cn^{1/3}})$	$O(n^{-\alpha})$
	Sinc functions	$O(e^{-cn^{1/6}})$	$O(e^{-cn^{1/6}})$ (sing. at end points)

3.2 SOLUTION OF DIFFERENTIAL OR INTEGRAL EQUATIONS

ORDER OF CONVERGENCE

METHOD	NO SINGULARITIES PRESENT	SINGULARITIES PRESENT
Finite difference	$O(n^{-a})$	$O(n^{-\alpha})$ $(\alpha \leq a)$
Finite element	$O(n^{-a})$	$O(n^{-\alpha})$ $(\alpha \leq a)$
Transmission line	$O(n^{-a})$	$O(n^{-\alpha})$ $(\alpha \leq a)$
Trig. functions, Polynomials	$O(e^{-cn^{1/3}})$	$O(n^{-\alpha})$
Sinc methods	$O(e^{-cn^{1/6}})$	$O(e^{-cn^{1/6}})$ (sing. at end-points only)
FFT	$O(e^{-cn^{1/6}})$	$O(n^{-\alpha})$

We do not wish to discourage the use of other methods, at this point. Finite

difference and finite element methods have the tremendous advantage that they

lead to sparse matrix problems, whereas sinc methods lead to fuller matrix problems.

The use of sinc methods in the approximate solution of 3 dimensional PDE problems

is still in the experimental stage, and while some breakthroughs have already been

made, indicating it may be possible to solve such problems with 1/100 of the

effort required by use of other methods, an efficient method is yet to be found

for solving the resulting system of linear algebraic equations. Theoretical

analysis of the error indicates that the use of sinc methods should reduce the

amount of effort in solving a problem by two orders of magnitude.

REFERENCES

[1] Ahlberg, J. H., E. N. Nilson and J. L. Walsh, The Theory of Splines and Their Applications, New York: Academic Press (1967).

[2] Davis, P. J., Interpolation and Approximation, Waltham Mass.: Blaisdell (1967).

[3] Lundin, L. and F. Stenger, Cardinal-Type Approximation of a Function and Its Derivatives, to appear in SIAM J. Math. Anal.

[4] Stenger, F., Approximations via Whittaker's Cardinal Functions, J. Approx. Theory $\underline{17}$ (1976) 222-240.

[5] _____, A Sinc-Galerkin Method of Solution of Boundary Value Problems, to appear in Math. Comp.

[6] _____, Optimum Convergence of Minimum-Norm Approximations in H_p, Numer. Math. $\underline{29}$ (1978) 345-362.

[7] Timan, A. F., Theory of Approximation of Functions of a Real Variable, Managr. Pure Appl. Math $\underline{34}$ (1963), McMillan, New York.

APPLICATION OF THE SINC–GALERKIN METHOD TO THE
SOLUTION OF THE 3D SOURCE – 3D BODY ELECTROMAGNETIC
SCATTERING PROBLEM

Bill Petrick
Department of Geology and Geophysics
University of Utah

I.   Mathematical Formulation

The most general representation of an electromagnetic field is via Maxwell's equations.

1. $\quad -\nabla \times \bar{E} = \hat{z}\,\bar{H} + \bar{M}_s$

2. $\quad \nabla \times \bar{H} = \hat{g}\,\bar{E} + \bar{J}_s$

Where: $\bar{E}$ = total electric field

$\bar{H}$ = total magnetic field

$\bar{M}_s$ = magnetic source

$\bar{J}_s$ = electric current source

$\hat{z}$ = impedivity ($i\omega\mu$)

$\hat{g}$ = admittivity ($\sigma + i\omega\varepsilon$)

We will consider only spacial changes in conductivity and assign free space values to μ (μ_0) and ε (ε_0) everywhere. With this assumption we can write $\hat{g}$ for a 3D inhomogeneity in the earth as:

3. $\quad \hat{g} = (\sigma_H + \Delta\sigma + i\omega\varepsilon) = \hat{g}_H + \Delta\sigma$

Where $\hat{g}_H$ refers to the material properties associated with a half space problem.

Substituting 3. into 2. we have:

4. $\quad \nabla \times \bar{H} = (\hat{g}_H + \Delta\sigma)\bar{E} + \bar{J}_s$

If we now define E and H as being made up of two components, the first being E_H and H_H (fields in the vicinity of a conductive half-space of conductivity σ_H), the second being ΔE and ΔH due to perturbations of σ_H accounting for the 3D subsurface structure.

5. $\quad \bar{E} = \bar{E}_H + \Delta\bar{E}$

6. $\quad \bar{H} = \bar{H}_H + \Delta\bar{H}$

Substituting 5. and 6. into 1. and 4. we have:

7. $\quad -\nabla \times (\bar{E}_H + \Delta\bar{E}) = \hat{z}(\bar{H}_H + \Delta\bar{H}) + \bar{M}_s$

8. $\quad \nabla \times (\bar{H}_H + \Delta\bar{H}) = (\hat{y}_H + \Delta\sigma)(\bar{E}_H + \Delta\bar{E}) + \bar{J}_s$

The half-s;ace fields may be solved for analytically via

9. $\quad -\nabla \times \bar{E}_H = \hat{z}\,\bar{H}_H + \bar{M}_s$

10. $\quad \nabla \times \bar{H}_H = \hat{y}_H E_H + \bar{J}_s$

The secondary fields then must satisfy

11. $\quad -\nabla \times \Delta\bar{E} = \hat{z}\,\Delta\bar{H}$

12. $\quad \nabla \times \Delta\bar{H} = (\hat{y}_H + \Delta\sigma)\Delta\bar{E} + \Delta\sigma\,\bar{E}_H$

By substituting 12. into the curl of 11. we have

13. $\quad \nabla \times \nabla \times \Delta\bar{E} - K^2 \Delta E = -\hat{z}\,\Delta\sigma\,\bar{E}_H$

Where: $\quad K^2 = -\hat{z}\hat{y} = -\hat{z}(\hat{y}_H + \Delta\sigma)$

The inhomogeneous term in 13. $\left(-\hat{z}\Delta\sigma\bar{E}_H\right)$ may be interpreted as a source in existence only where $\Delta\sigma$ is non-zero.

Equation 13. may be solved over any region for which we can obtain boundary conditions on ΔE.

I have chosen to solve equation 13. in the earth only. The values of at the air-earth interface may than be obtained from

14. $\quad \Delta E^{BOUNDARY} = \int_{Vol} \bar{\bar{\Gamma}}\,\bar{J}_s\,dV \qquad \bar{J}_s = \Delta\sigma\,\bar{E}^{TOTAL}$

Where: $\bar{J}_s$ = the volume scattering current density.

$\bar{\bar{\Gamma}}$ = half space dyadic Greens function.

Note that 14. need only be evaluated where $\Delta\sigma$ is non-zero. If we further assume that $\Delta\sigma = 0$ at the surface of the earth then 14. is never a singular integral.

II. Method of solution of equation 13.

    a) Galerkins Method

        Consider the equation

15. $Lu = g$

where L is some integral or differential operator (linear in our case) u are a set of unknowns and g is a known forcing function attributable to applied sources or boundary conditions.

We approximate u by some basis function presumably capable of tracking the unknown throughout the region of interest. Let:

16. $$u = \sum_n u_n f$$

where f is the chosen basis function. Substitute 16. into 15. and use linearity to obtain

$$\sum_n u_n Lf \cong g$$

Subtracting g from both sides we find the error α

17. $$\sum_n u_n Lf - g = \alpha$$

Take the inner product of α with a set of weights and set this projection to zero to obtain

18. $$\sum_n u_n \int_\Gamma Lf \omega \, dV = \int_\Gamma g \omega \, dV$$

This equation results in a set of equations for u_n. Once obtaining the u_n's we may calculate u from 16.

    b) Choice of Basis Functions

        In addition to being capable of adequately describing the behavior

of the unknown function the choice of basis functions (and weights) is, from a practical point of view, dependent upon the ease with which the inner product can be calculated.

For our basis functions and weights we choose sinc functions

$$S(k,h) \circ \varphi(x) = \frac{\sin\left[\frac{\pi}{h}(\varphi(x) - kh)\right]}{\frac{\pi}{h}(\varphi(x) - kh)}$$

Where $\varphi(x)$ is some map from the particular interval over which a solution is sought to the interval $(-\infty, \infty)$. For the solution in the earth we have:

$$\varphi(x) = x, \quad \varphi(y) = y, \quad \varphi(z) = \ln\left(\sinh\frac{z}{2c}\right)$$

Another $\varphi(z)$ map which could be used is

$$\varphi(z) = \ln z$$

Both the $\ln z$ and $\ln\left(\sinh\frac{z}{2c}\right)$ transofrmations specify a higher point density near $z = 0$ but the sinh map has an apparent advantage of becoming equispaced for large Z. The constant c determines this spacing.

The specific form for the associated inner products have been worked out by Stenger (1979)*. They are:

19.
$$\int_\Gamma r(\omega) u(\omega) [S(k,h) \circ \varphi(\omega)] d\omega \cong h \frac{u_k r_k g_k}{\varphi'_k}$$

$$\int_\Gamma r(\omega) u'(\omega) [S(k,h) \circ \varphi(\omega)] d\omega \cong -h \sum_{j=-N}^{N} u_j \left\{ \frac{(rg)'_j}{\varphi'_j} \delta^0_{kj} + (rg)_j \frac{\delta'_{kj}}{h} \right\}$$

$$\int_\Gamma r(\omega) u''(\omega) [S(k,h) \circ \varphi(\omega)] d\omega = h \sum_{j=-N}^{N} u_j \left\{ \frac{(rg)''_j}{\varphi'_j} \delta^0_{kj} + \frac{[2(rg)'\varphi' + (rg)_j \varphi'']}{\varphi'} \frac{\delta'_{kj}}{h} \right.$$
$$\left. + (rg)_j \varphi'_j \frac{\delta^2_{kj}}{h^2} \right\} 9$$

*Stenger, F. S. (1979) A "Sinc-Galerkin" Method of Solution of Boundary Value Problems: to appear in Mathematics of Computation, January 1979.

where: r is the coefficient in the differential equation

$\mathcal{C}(\omega)$ map taking $\mathcal{I}$ to $-\infty, \infty$

$g(\omega) = 1/\mathcal{C}'(\omega)$

$$\delta^o_{k,j} = \begin{cases} 1 & k=j \\ 0 & k \neq j \end{cases} \qquad \delta'_{k,j} = \begin{cases} 0 & k=j \\ \dfrac{(-1)^{j-k}}{j-k} & k \neq j \end{cases} \qquad \delta^2_{kj} = \begin{cases} -\pi^2/3 & k=j \\ \dfrac{-2(-1)^{j-k}}{(j-k)^2} & k \neq j \end{cases}$$

The solution to 13. will be analytic over a region if K^2 is analytic over the region. The sinc interpolants are analytic and we consider point evaluations of $\Delta\sigma$ (also sinc expanded) so that we are considering conductivity as being an analytic function in the earth.

II. Numerical formulation and assumptions

Expanding 13. into its vector components we have:

20. $\Delta E'_{22} + \Delta E'_{33} - \Delta E^2_{12} - \Delta E^3_{13} + K^2 \Delta E' = \hat{z} \Delta\sigma E'_H$ x component

$\Delta E^2_{33} + \Delta E^2_{11} - \Delta E^3_{23} - \Delta E'_{12} + K^2 \Delta E^2 = \hat{z} \Delta\sigma E^2_H$ y component

$\Delta E^3_{11} + \Delta E^3_{22} - \Delta E'_{31} - \Delta E^2_{23} + K^2 \Delta E^3 = \hat{z} \Delta\sigma E^3_H$ z component

where: $\Delta E'_{23} = \partial \Delta E'/\partial y \partial z$ etc.

We solve this set of equations using Galerkins method with the sinc basis functions. Implicit in the use of these basis functions are zero boundary conditions. Since, at z = 0, we have a non-zero boundary condition we will solve for a function that is zero at z = 0 and add to it a boundary term obtained via 14. Define the following

21. $\Delta E^I = \varepsilon^I + \Delta E^{IB} e^{-\beta z}$ $I = 1,2,3$ $z \geq 0$

Where ε is to be solved for and is zero on all boundaries and β is a

constant to be chosen.

Continuity of normal J at z = 0 is.

$$J^3_{air} = J^3_{earth}$$

$$\sigma_o E^3_{air} = \sigma_H E^3_{earth}$$

$$\sigma_o (E^3_{Hair} + \Delta E^3_{air}) = \sigma_H (E^3_{H\,earth} + \Delta E^3_{earth})$$

Since the secondary fields must satisfy the same boundary conditions

as the primary fields we have

$$\Delta E^3_{earth} = \sigma_o/\sigma_H \Delta E^3_{air} \qquad \therefore \Delta E^3_{earth} \Rightarrow 0 \text{ at } z = 0$$

So we may set ΔE^{3B} in 21 to zero.

Substitute 21 into 20 and expand

$$\varepsilon^1_{22} = -\varepsilon^1_{33} + \varepsilon^2_{12} + \varepsilon^3_{13} - K^2\varepsilon^1 - e^{-\beta z}\left[\Delta E^{1B}_{22} - \Delta E^{2B}_{12} + (\beta^2+K^2)\Delta E^{1B}\right]$$
$$+ \hat{z}\Delta\sigma E^1_H$$

22.

$$\varepsilon^2_{11} = -\varepsilon^2_{33} + \varepsilon^3_{23} + \varepsilon^1_{21} - K^2\varepsilon^2 - e^{-\beta z}\left[\Delta E^{2B}_{11} - \Delta E^{1B}_{12} + (\beta^2+K^2)\Delta E^{2B}\right]$$
$$+ \hat{z}\Delta\sigma E^2_H$$

$$\varepsilon^3_{11} + \varepsilon^3_{22} = \varepsilon^1_{13} + \varepsilon^2_{23} - K^2\varepsilon^3 + \hat{z}\Delta\sigma E^3_H$$

If we choose $\beta^2 = -K^2_H$ (this corresponds physically to subtracting out

the planewave solution) then $(\beta^2 + K^2) = -\hat{z}\Delta\sigma$. The equations to which we seek

a Galerkin solution are then:

$$\varepsilon^1_{22} = -\varepsilon^1_{33} + \varepsilon^2_{12} + \varepsilon^3_{13} - K^2\varepsilon^1 - e^{-\beta z}\left[\Delta S^1\right] + \hat{z}\Delta\sigma E^1_H$$

23.

$$\varepsilon^2_{11} = -\varepsilon^2_{33} + \varepsilon^3_{23} + \varepsilon^1_{21} - K^2\varepsilon^2 - e^{-\beta z}\left[\Delta S^2\right] + \hat{z}\Delta\sigma E^2_H$$

$$\varepsilon^3_{11} + \varepsilon^3_{22} = \varepsilon^1_{13} + \varepsilon^2_{23} - K^2\varepsilon^3 + \hat{z}\Delta\sigma E^3_H$$

The ΔS terms are evaluated via the half space Greens dyadic.

Where: $\Delta S^1 = \Delta E^{1B}_{22} - \Delta E^{2B}_{12} - \hat{z}\Delta\sigma E^1_H$

$$\Delta S^2 = \Delta E^{2B}_{11} - \Delta E^{1B}_{12} - \hat{z}\Delta\sigma E^2_H$$

We define

24. $\quad \varepsilon^{I}(x,y,z) = \sum_i \sum_j \sum_k \varepsilon^{I}_{ijk} \, S(x,i) \, S(y,j) \, S(\ell(z),k)$

Where $\quad S(\ell(a),\ell) = \sin\left[\frac{\pi}{h}(\ell(a)-h\ell)\right] \Big/ \left[\frac{\pi}{h}(\ell(a)-h\ell)\right]$

$\qquad \ell(z) = \ln\left[\sinh\frac{z}{zc}\right]$

Substituting 24 into 23 and taking the inner product with similar weight functions we obtain for typical terms.

25. $\quad \int_{\Gamma} \varepsilon^{1}_{22} \, S(x,I) \, S(y,J) \, zc\tanh\frac{z}{zc} \, S(\ell(z),k) \, dx\,dy\,dz$

$\qquad = h_x h_y h_z \left[zc\tanh\frac{z}{zc}\right]^2 \sum_j \varepsilon^{1}_{I,j,k} \left[\frac{\delta^2_{J,j}}{h_y^2}\right]$

which can be written as the matrix multiplication

$\qquad = \frac{h_x h_y h_z}{h_y^2} \left[zc\tanh\frac{z}{zc}\right]^2 \left[\varepsilon^1_k\right]\left[I^2_j\right]$

Similarly

$\quad \int_{\Gamma} \varepsilon^2_{12} \, S(x,I) \, S(y,J) \, zc\tanh\frac{z}{zc} \, S(\ell(z),k) \, dx\,dy\,dz$

$\qquad = \frac{h_x h_y h_z}{h_x h_y} \left[I^1_x\right]\left[\varepsilon^2\right]\left[I^1_j\right]$

$\quad \int_{\Gamma} \varepsilon^3_{13} \, S(x,I) \, S(y,J) \, zc\tanh\frac{z}{zc} \, S(\ell(z),k) \, dx\,dy\,dz$

$\qquad = \frac{h_x h_y h_z}{h_x} \left[I^1_x\right] \sum_k \left[\varepsilon^3_k\right] \left\{\delta^{0+1}_{k,k}\right\}$

Where $\left[I^1_x\right], \left[I^2_j\right], \left[I^1_x\right]\left[I^1_j\right]$; and $\left\{\delta^{0+1}_{k,k}\right\}$ are composed of the previously defined

$\qquad \delta^0_{i,j} \, , \, \delta^1_{i,j} \, , \, \delta^2_{i,j}$

and where the matrices $\left[\varepsilon_{L}^{I}\right]$ $I<1,2,3$ contain the unknown coefficients at each level corresponding to z_k in the earth.

We now have the following simultaneous set of matrix equations to solve:

26.

$$\left[\varepsilon_{k}^{1}\right]\left\{\left[I_{y}^{2}\right]+\frac{h_{y}^{2}\,\delta_{k,k}^{o+1+2}}{\left[2c\tanh\frac{z_k}{2c}\right]^{2}}+h_{y}^{2}\,K_{H}^{2}\right\}=+h_{y}^{2}\,\hat{z}\,\Delta\sigma_{k}\left\{\left[\varepsilon_{k}^{1}\right]+E_{H}^{1}\right\}$$

$$-\frac{h_{y}^{2}}{\left[2c\tanh\frac{z_k}{2c}\right]^{2}}\sum_{\substack{k\\k\neq K}}\left[\varepsilon_{k}^{1}\right]\delta_{k,k}^{o+1+2}+\frac{h_{y}}{h_{x}}\left[I_{x}^{1}\right]\left[\varepsilon_{k}^{2}\right]\left[I_{y}^{1}\right]$$

$$+\frac{h_{y}^{2}}{\left[2c\tanh^{2}\frac{z_k}{2c}\right]h_{x}}\left[I_{x}^{1}\right]\sum_{k}\left[\varepsilon_{k}^{3}\right]\delta_{k,k}^{o+1}+h_{y}^{2}\,e^{-\beta z_k}\left[\Delta S^{1}\right]\,.$$

27.

$$\left\{\left[I_{x}^{2}\right]+\frac{h_{x}^{2}\,\delta_{k,k}^{o+1+2}}{\left[2c\tanh\frac{z_k}{2c}\right]^{2}}+h_{x}^{2}\,K_{H}^{2}\right\}\left[\varepsilon_{k}^{2}\right]=h_{x}^{2}\,\hat{z}\,\Delta\sigma_{k}\left\{\left[\varepsilon_{k}^{2}\right]+E_{H}^{2}\right\}$$

$$-\frac{h_{x}^{2}}{\left[2c\tanh\frac{z_k}{2c}\right]^{2}}\sum_{\substack{k\\k\neq K}}\left[\varepsilon_{k}^{2}\right]\delta_{K,k}^{o+1+2}+\frac{h_{x}}{h_{y}}\left[I_{x}^{1}\right]\left[\varepsilon_{k}^{1}\right]\left[I_{y}^{1}\right]$$

$$+\frac{h_{x}^{2}}{\left[2c\tanh^{2}\frac{z_k}{2c}\right]h_{y}}\sum_{k}\left[\varepsilon_{k}^{3}\right]\left[I_{y}^{1}\right]\delta_{K,k}^{o+1}+h_{x}^{2}\,e^{-\beta z_k}\left[\Delta S^{2}\right]\,.$$

28.

$$\left[I_{x}^{2}\right]\left[\varepsilon_{k}^{3}\right]+\left[\varepsilon_{k}^{3}\right]\left\{\left[I_{y}^{1}\right]\frac{h_{x}^{2}}{h_{y}^{2}}+h_{x}^{2}\,K_{H}^{2}\right\}=h_{x}^{2}\,\hat{z}\,\Delta\sigma_{k}\left\{\left[\varepsilon_{k}^{3}\right]+E_{H}^{3}\right\}$$

$$+\frac{h_{x}}{\left[2c\tanh^{2}\frac{z_k}{2c}\right]}\left[I_{x}^{1}\right]\sum_{k}\left[\varepsilon_{k}^{1}\right]\delta_{k,k}^{o+1}+\frac{h_{x}^{2}}{\left[2c\tanh^{2}\frac{z_k}{2c}\right]}\sum_{k}\left[\varepsilon_{k}^{2}\right]\left[I_{y}^{1}\right]\delta_{K,k}^{o+1}\,.$$

Equations 26, 27 and 28 are then solved iteratively for $\left[\varepsilon_{k}^{I}\right]$, $I=1,2,3$.

Note added 7/78

At the time of the conference I was unable to obtain, iteratively, a solution of the system represented by equations 26 thru 28. Since that time I've determined the problem to be due to the underlined terms in equations 26 and 27. These terms have the effect of generating large off-diagonal elements in the system matrix.

GENERALIZED THIN LAYER APPROXIMATION FOR MAGNETOTELLURICS
AND A MULTIPLE SCALE METHOD OF IMPLEMENTING
THE NUMERICAL CALCULATIONS

Theodore R. Madden and Rambabu Ranganayaki

Department of Earth and Planetary Sciences
Massachusetts Institute of Technology
Cambridge, Massachusetts 02139

The thin sheet analysis introduced by Prof. Price can be generalized by making the sheet anisotropic to model the effect of layers within the sheet of different conductivity and also by generalizing the boundary conditions. Calculations and analytic solutions for such models show that the resistivity thickness product of the sheet has a profound effect on the magnetotelluric field and this effect influences the telluric field over very large distances. To accurately model magnetotelluric responses one must include regions many hundreds of kilometers away. A multiple scale approach to these calculations is very appropiate as only average properties and fields are needed to describe the influence of distant zones.

AN APPLICATION OF THE MODE MATCH
METHOD TO BORE HOLE INDUCTION LOGGING

A. Q. Howard, Jr.
Department of Electrical Engineering
University of Arizona
Tucson, Arizona 85719

Abstract

The mode match method relies on local orthogonality of modes. The approach is a specialized integral equation method which results in a matrix form of an integral equation. The expansion functions are total range and have exponential convergence properties when n, the number of modes is larger than $|k_4 D|$ when k_4 is the complex awave number of the host rock and D is the largest dimension of the anomaly that requires the use of integral equations. The application here is to obtain the dipole fields of the bore hole environment. The magnetic transmitter and receiver loops are in a vertical plane to best excite eddy currents in cracks around the bore hole which are also oriented vertically.

Introduction

For the purposes of this workshop, the emphasis of this paper is placed on method rather than results. It is true that the mode match formalism is not as general as direct finite element methods or finite difference methods. However when the modes can be introduced they result in an economy in computer usage along with an improvement in accuracy. The price that must be paid is an increased amount of matrix element computation analysis and perhaps over simplified

geometric models.

Thus direct application of these methods is limited to highly specialized geometries and also as an analytic model which more general methods could be compared.

However it is becoming apparent that direct computation and modelling of geometries of practical interest are straining our largest and fastest computers and that often the desirable halving of patch sizes or node lengths when we are approaching relative convergence on these machine codes is impossible.

Hybrid methods which combine the best features of two or more methods will play a role of increasing importance in future electromagnetic modeling. An important example is the unimoment method of Professor K.K. Mei.[1] His former student S. Chang applied the method to the buried sphere at this conference and discussed how it can be applied to more general buried bodies by circumscribing the body with a mathematical sphere. Outside the sphere, known eigenfunction expansions are used and inside finite element methods are applied.

In this context mode matching takes on new relevance. An example is that of the buried dyke. To surround this structure by a sphere may be very inefficient compared to a rectangular volume or truncated cylinder. If a mode match solution could be obtained for such structures, the unimoment method could be efficiently applied to the general dyke problem. Some work [1,2] indicates that this may be possible.

Theory

The bore hole problem has sufficient symmetry to render the mode matching, at least formally, to be rather straight forward. The purpose of the calculation is to correct magnetic loop measurements to account for the source cavity as shown in Figure 1. The cavity is assumed to be filled with air. In region 1, the magneto-static fields of the loop dominate the primary fields. However, the bore hole is filled with a highly conductive fluid so that there is a strong axial component of the secondary electric field.

For a time dependence $e^{-i\omega t}$, the primary magnetic field is due to a loop as shown in the figure is computed as follows:

$$\bar{H} = i\omega\varepsilon_1 \; (\bar{\bar{I}} + \frac{\nabla\nabla}{k_1^2}) \cdot \bar{F}$$

$$\bar{F} = -i\omega\mu_1 m_o \; \hat{i}_m \; g.$$

(1)

Here, in (2) and (3) ε_1, μ, and k_1 are the dielectric constant, permeability, and wave number appropriate for the cavity or gap region. The quantity $m_o = \pi b^2 I_o$ is the magnetic dipole moment of the loop and $\hat{i}_m$ is the orientation unit vector of the loop as shown in Figure 1.

The function g satisfies the conditions.

$$(\nabla^2 + k_1^2) \; g = -\delta(\bar{x} - \bar{x}_T)$$

(2)

$$\frac{\partial g}{\partial Z} \Big|_{Z = \pm D/2} = 0$$

The appropriate solution to g when D/a is large is given approximately by:

$$g = \frac{1}{2\pi a} \; J_O \; (\alpha_{0_1} \ell/a) \; J_O \; (\alpha_{0_1} \ell^1/a) \; f(z,z')$$

$$f(z,z') = \frac{\cos h(\alpha(D/2-z_>)) \; \cos h(\alpha Z_<)}{\sinh (\alpha D/2)} \; , \; \alpha = \alpha_{0_1}/a \tag{3}$$

and $\alpha_{0_1} = 2.4048 \ldots$ is the first zero of J_O.

The interior scattered fields are represented by a Fourier series:

$$\bar{H}^S = 1/\mu_1 \; \bar{\nabla} \times \bar{A}^S, \; \bar{A}^S = \hat{i}_z \; \bar{\phi}^S \tag{4}$$

$$\phi^S = \sum_{m=o} b_m \; \cos \; (\lambda_m Z) \; I_1 \; (\beta_m Z) \; \cos \; \phi$$

where

$$\beta_m = (\lambda_m^2 - (k_1^2)^{\frac{1}{2}}, \; Re(\beta_m) \geq 0, \; \lambda_m = \frac{2\pi}{D} m. \quad \text{And,}$$

I_1 is a modified Bessel function of the first kind of order 1.

The exterior fields ($\rho \geq a$) are expressed as a Fourier transform on z with an unknown Fournier amplitude a(h).

$$\bar{A}^e \; (\bar{x}) = \hat{i}_z \; \cos \; \phi \; \int_{-\infty}^{\infty} a(h) \; k_1(\beta\rho) \; e^{ihz} \; dh \tag{5}$$

$$\beta = (h^2 - k_4^2)^{\frac{1}{2}}, \; Re(\beta) \geq 0.$$

The solution for the unknown mode amplitudes b_m as defined in (4) are obtained by matching H_ϕ and E_z on $\rho = a$. One obtains the following matrix equation.

$$\sum_{n=o}^{\infty} L_{mn} \; a_n = f_m \tag{6}$$

where $a_m = \beta_m^2 \; I_1(\beta_{ma}) \; b_m$

$$f_m = - \frac{\epsilon_m \beta_m}{2\pi a^3} \cdot \frac{I_1(\beta_m a)}{I_1{}'(\beta_m a)} \quad m_0{}^\mu 1 \frac{\cos(\lambda_m z_T)}{(m\pi)^2 + y^2} \frac{J_0(\alpha\rho_T)}{J_1(\alpha_0 1)} \tag{7}$$

$$L_{mn} = -\delta_{nm} + \frac{\epsilon_n D\tilde{\epsilon}_4 \beta_n}{2\pi\epsilon_1} \frac{I_1(\beta_n a)}{I_1{}'(\beta_n a)} I_{nm}$$

$$I_{nm} = 2A \int_0^\infty \frac{T_n(x) T_m(x) k_1{}'(u)}{u k_1(u)} dx \tag{8}$$

$$u = (x^2 A^2 - \alpha^2)^{\frac{1}{2}}, \quad A = 2a/D, \quad \alpha = k_4 a.$$

$$T_m(x) = \frac{(-1)^m x \sin x}{x^2 - (m\pi)^2}$$

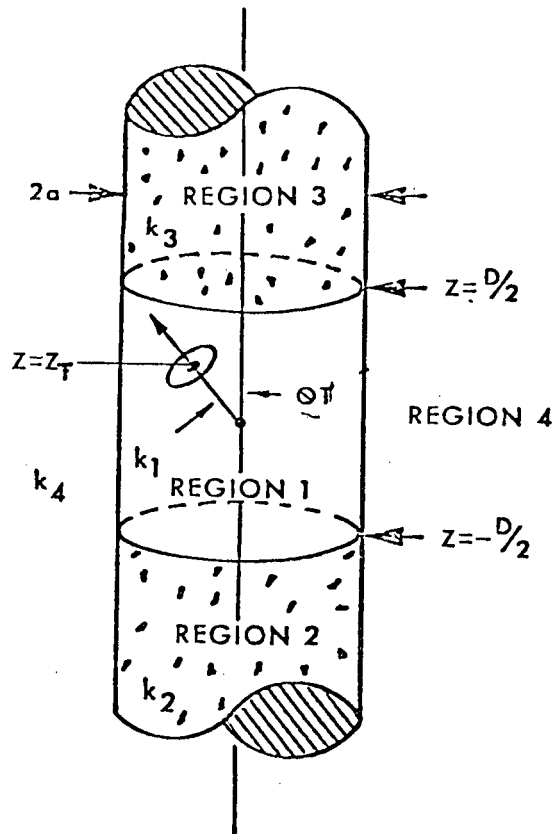Details of the solution and numerical information will be published elsewhere. (4)

Figure 1 Model Geometry

REFERENCES

(1) Mei, K.K., 1974, "Unimoment Method of Solving Antenna and Scattering Problems", IEEE Trans. Antennas Propagation. Vol A p. 22; No. 6, pp. 760-766.

(2) Howard, A. Q., Jr., 1972, "The Electromagnetic Fields of a Subterranean Cylindrical Inhomogeneity Excited by a Line Source". Geophysics, v. 37, No. 6, pp. 975-984.

(3) Howard, A. Q., Jr., 1975, "A Canonical Solution to the Three-Dimensional Electromagnetic Prospecting Problem". Radio Science, v. 10, No. 4, pp. 461-471.

(4) Howard, A. Q., Jr., 1978. To be published as a Los Alamos Scientific Laboratories Report.

CALCULATION OF MAGNETIC FIELDS DUE TO STEADY-STATE CURRENT SYSTEMS

David V. Fitterman

U.S. Geological Survey

Stop 964 Box 25046

Denver Federal Center

Denver, Colorado 80225

Introduction

The calculation of magnetic fields produced by steady-state current distributions has application in several geophysical techniques. The usual method of calculating the magnetic field is to use Ampere's law when the problem is sufficiently symmetric, or the Biot-Savart law for problems lacking the requisite symmetry. The volume integration required by the Biot-Savart law can be quite expensive when done numerically. In this paper, a technique will be demonstrated which reduces the calculation of the magnetic field to the evaluation of surface integrals over all conductivity boundaries, thereby reducing the computational effort. An added benefit of this formulation is that the components of the magnetic field that will be produced can be determined simply by inspection of the conductivity structure.

Theory

The magnetic field produced by a steady-state current system is given by the Biot-Savart law

$$\vec{B} = \nabla \times \iiint_V dv \, \frac{\mu \vec{J}}{4\pi r} \tag{1}$$

Using operator notation, (1) can be rewritten as

$$\vec{B} = \nabla \times \text{pot} \, \mu \vec{J} \tag{2}$$

where the potential operator is defined by

$$\text{pot} \, (\ ) = \iiint_V dv \, \frac{(\ )}{4\pi r} \tag{3}$$

and $\vec{r} = \vec{x}' - \vec{x}$ where $\vec{x}' = (x', y', z')$ is the magnetic field observation point and $\vec{x} = (x, y, z)$ is the source location. Numerical evaluation of the volume integration in (2) can be expensive. We now follow an exercise first described by Heaviside [1892], which provides a means of simplifying the computation. More importantly, the alternative formulation very clearly shows what controls the magnetic field.

Consider a divergence-free vector $\vec{Z}$, from which a chain of vectors is constructed by taking the curl of the previous element of the chain.

$$\vec{A} = \nabla \times \vec{Z} \tag{4a}$$

$$\vec{B} = \nabla \times \vec{A} = \nabla \times \nabla \times \vec{Z} = -\nabla^2 \vec{Z} \tag{4b}$$

$$\vec{C} = \nabla \times \vec{B} = \nabla \times \nabla \times \vec{A} = -\nabla^2 \vec{A} \tag{4c}$$

$$\vec{D} = \nabla \times \vec{C} = \nabla \times \nabla \times \vec{B} = -\nabla^2 \vec{B} \tag{4d}$$

$\vec{A}$, $\vec{B}$, and $\vec{C}$ are replaced by their curl representation respectively, i.e., $\nabla \times \vec{Z}$, $\nabla \times \vec{A}$, and $\nabla \times \vec{B}$. The expression $\nabla \times \nabla \times (\ )$ becomes $-\nabla^2 (\ )$ since $\nabla \cdot (\ ) = 0$. Recognizing that (4b-d) are vector Poisson's equations, the solutions are given by

$$\vec{Z} = \text{pot } \vec{B} \tag{5a}$$

$$\vec{A} = \text{pot } \vec{C} \tag{5b}$$

$$\vec{B} = \text{pot } \vec{D} \tag{5c}$$

Thus, we have established that the operator $\nabla \times \nabla \times (\ )$ is the inverse of pot $(\ )$.

Substituting (4d) into (5c) and (5b) into (4b) gives,

respectively,

$$\vec{B} = pot\ \vec{D} = pot\ \nabla \times \vec{C} \tag{6a}$$

$$\vec{B} = \nabla \times \vec{A} = \nabla \times pot\ \vec{C} \tag{6b}$$

proving the commutativity of pot ( ) and $\nabla \times$ ( ). Note the only assumption made is that the vectors involved are divergence free. For the case of the magnetic field we can write

$$\vec{B} = \nabla \times pot\ (\mu\ \vec{J}) = pot\ \nabla \times (\mu\ \vec{J}) \tag{7}$$

For the non-operator-inclined reader this result can alternatively be proved by starting with (1). Then,

$$\vec{B}\ (\vec{x}') = \nabla' \times \vec{A}\ (\vec{x}') = \nabla' \times \iiint_V dv\ \frac{\mu\ \vec{J}(\vec{x})}{4\pi r} = \iiint_V dv\ \nabla' \times \left(\frac{\mu\ \vec{J}(x)}{4\pi r}\right) \tag{8}$$

where ∇' denotes differentiation with respect to the observation coordinate. Recognizing that $\nabla \times \vec{J}(x) = 0$ and $\nabla'(1/r) = -\nabla(1/r)$ gives

$$\vec{B}(\vec{x}') = \iiint_V dv\ \frac{\mu\ \vec{J}(\vec{x})}{4\pi} \times \nabla'\left(\frac{1}{r}\right) = -\iiint_V dv\ \frac{\mu\ \vec{J}(\vec{x})}{4\pi} \times \nabla\left(\frac{1}{r}\right) \tag{9}$$

The integrand in (9) can be written as

$$\mu\ \vec{J}(\vec{x}) \times \nabla(1/r) = \nabla \times \left(\frac{\mu\ \vec{J}(\vec{x})}{r}\right) - \frac{1}{r}\nabla \times \left(\mu\ \vec{J}(\vec{x})\right) \tag{10}$$

thus we get

$$\vec{B}\ (\vec{x}') = \iiint_V dv\ \frac{\nabla \times (\mu\ \vec{J}(\vec{x}))}{4\pi r} - \iiint_V dv\ \nabla \times \left(\frac{\mu\ \vec{J}(\vec{x})}{4\pi r}\right) \tag{11}$$

Finally, using a generalized Gauss theorem [Nadeau, p. 16, 1964] on the rightmost term gives

D. V. Fitterman

$$\vec{B}(\vec{x}') = \iiint_V dv \, \frac{\nabla \times (\mu \, \vec{J}(\vec{x}))}{4\pi r} - \iint_S ds \, \hat{n} \times \left(\frac{\vec{J}(\vec{x})}{4\pi r} \right) \tag{12}$$

where S is a surface enclosing all current and $\hat{n}$ is the outward to this surface. As the volume of integration becomes infinite, the surface integral vanishes, since the current density approaches zero at least as fast as $1/r$, yielding the same result as in (7).

To demonstrate the advantage of this formulation, we write the current density as

$$\vec{J} = -\sigma \nabla \phi \tag{13}$$

Taking the curl of (13) gives

$$\nabla \times \vec{J} = -\nabla \sigma \times \nabla \phi \tag{14}$$

For Earth models constructed of homogeneous regions of differing conductivity, $\nabla \times \vec{J}$ will be zero except at conductivity, boundaries. The magnetic field is then given by

$$\vec{B}(\vec{x}') = \iiint_V dv \, \frac{\mu \nabla \times \vec{J}}{4\pi r} = -\sum_i \iint_{S_i} ds \, \frac{\mu \, \Delta \sigma_i \, \hat{n} \times \nabla \phi}{4\pi r} = \sum_i \iint_{S_i} ds \, \frac{\mu \Delta \sigma_i \, \hat{n} \times \vec{J}}{4\pi \sigma r} \tag{15}$$

where S_i represents the conductivity boundaries, $\Delta \sigma_i$ is the change in conductivity at the boundary, σ is the conductivity on the side of the boundary where $\vec{J}$ is specified, and $\hat{n}$ is the unit normal to S_i. Notice that the computation has been reduced from a volume integration to a sum of surface integrations--a considerable computational savings. From (14) we see that two orthogonal components of $\vec{B}$ will be produced by a planar boundary. The magnetic field will be increased by orienting the current sources such that most of the current is flowing parallel the conductivity boundary.

An Example--Electrokinetic Currents

The flow of fluid through geologic materials results in a charge separation because of the differential interaction of the ionic species in solution with the charged mineral grains. This generation mechanism is called streaming potential. For geologic materials, the pressure field is independent of electric effects; therefore, the electric field can be solved for from a known pressure distribution. An analysis of the governing equations can be found in Nourbehecht [1963] or Fitterman [1978a, 1978b]. We will consider the case of two quarter-spaces in contact with each other occupying the region $z > 0$. (See Figure 1.) For a pressure source of constant intensity within the region $a \le z \le b$ and $-1/2 \le x \le 1/2$, the surface potential is given by

$$\psi_2(x,y,o) = \frac{S_o}{\pi(1+\sigma_i/\sigma_j)} \left\{ f(x,y,b,\ell/2) - f(x,y,a,\ell/2) - f(x,y,b,-\ell/2) + f(x,y,a,-\ell/2) \right\} \tag{16}$$

where

$$f(x,y,\alpha,\beta) = \tan^{-1} \frac{(x+\alpha)\beta}{y[(x+\alpha)^2 + y^2 + \beta^2]^{1/2}} \tag{17}$$

S_o is the source intensity, and the conductivity σ_j takes the value σ_i for $y > 0$ and σ_j for $y < 0$.

On the surface of the half-space, $\nabla \times \vec{J} = -\hat{i} J_y + \hat{j} J_x$ and the resulting magnetic fields are given by

$$B_x(x',y',o) = \frac{\sigma\mu}{4\pi} \int_{-\infty}^{\infty} dx \int_{-\infty}^{\infty} dy \frac{\phi_{,y}}{R} \tag{18a}$$

and

$$B_y(x',y',0) = \frac{\sigma\mu}{4\pi} \int_{-\infty}^{\infty} dx \int_{-\infty}^{\infty} dy \, \frac{\phi_{,x}}{R}$$

(18b)

where $R^2 = (x'-x)^2 + (y'-y)^2$ and the subscript and comma denote differentiation. Equation (18) is evaluated numerically using adaptive Gaussian and Gauss-Laguerre quadratures. The singularity at $R = 0$ is analytically integrated. At the contact between the quarter-spaces the curl of $\vec{J}$ is $\hat{i}(J_{1z} - J_{2z}) - \hat{k}(J_{1x} - J_{2x})$. The contribution due to this surface can be analytically integrated to obtain

$$B_x(x',y',0) = \frac{S_o \sigma_1 \sigma_2 \mu}{2\pi(\sigma_1+\sigma_2)} \ln \frac{\left[\sqrt{(x'+\ell/2)^2+y'^2+a^2} + (x'+\ell/2)\right]\left[\sqrt{(x'-\ell/2)^2+y'^2+b^2} + (x'-\ell/2)\right]}{\left[\sqrt{(x'-\ell/2)^2+y'^2+a^2} + (x'-\ell/2)\right]\left[\sqrt{(x'+\ell/2)^2+y'^2+b^2} + (x'+\ell/2)\right]}$$

(19a)

and

$$B_g(x',y',0) = \frac{S_o \sigma_1 \sigma_2 \mu}{2\pi(\sigma_1+\sigma_2)} \ln \frac{\sqrt{(x'+\ell/2)^2+y'^2+a^2} + a\left.\right]\left[\sqrt{(x'-\ell/2)^2+y'^2+b^2} + b\right]}{\left[\sqrt{(x'+\ell/2)^2+y'^2+b^2} + b\right]\left[\sqrt{(x'-\ell/2)^2+y'^2+a^2} + a\right]}$$

(19b)

The self-potential and magnetic field component maps are shown in Figures 2, 3, 4, and 5. In Figure 2 we see that the largest gradient of ϕ is in the y-direction. From (14) we know this will produce an x-component of magnetic field (Figure 3). The x-component of field produced by the vertical interface is small compared to the contribution of the horizontal surface.

Extension To 2-dimensional MMR Anomalies

Magnetometric resistivity (MMR) anomalies have been calculated for some rather simple geometries using symmetry conditions [Stefanescu, 1958; Stefanescu and Nabighian, 1962; Edwards, 1974; Edwards and Howell, 1976]. The technique described above is well suited for the calculation of these anomalies. Let us consider a 2-D conductivity structure (constant along strike) that is represented by rectangular regions bounded by vertical and horizontal surfaces. Following a technique described by Madden [1971], the currents along the edges of the rectangles can be determined. Then, from (15) it follows that the magnetic field produced by a horizontal interface is

$$B_x^h = \frac{\mu}{4\pi} \int_{-\infty}^{\infty} dx \int_a^b dy \ \frac{\Delta\sigma}{\sigma} \ \frac{J_y}{R} \tag{20a}$$

$$B_y^h = \frac{\mu}{4\pi} \int_{-\infty}^{\infty} dx \int_a^b dy \ \frac{\Delta\sigma}{\sigma} \ \frac{J_x}{R} \tag{20b}$$

while a vertical interface produces the following components

$$B_x^v = \frac{-\mu}{4\pi} \int_{-\infty}^{\infty} dx \int_c^d dz \ \frac{\Delta\sigma}{\sigma} \ \frac{J_z}{R} \tag{20c}$$

$$B_z^v = \frac{\mu}{4\pi} \int_{-\infty}^{\infty} dx \int_c^d dz \ \frac{\Delta\sigma}{\sigma} \ \frac{J_x}{R} \tag{20d}$$

where the vertical interface occupies $c \leq z \leq d$ and the horizontal interface lies in the range $a \leq x \leq b$.

Assuming the currents are constant in the x and z directions along the edges of a cell, (20) can be integrated thus:

$$B_x^h = \frac{\mu \Delta\sigma}{4\pi\sigma} \int_{-\infty}^{\infty} dx \; J_y(x) \; \ln \frac{\sqrt{(x'-x)^2 + (y'-b)^2 + c^2} + (y'-b)}{\sqrt{(x'-x)^2 + (y'-a)^2 + c^2} + (y'-a)} \qquad (21a)$$

$$B_y^h = \frac{-\mu \Delta\sigma}{4\pi\sigma} \int_{-\infty}^{\infty} dx \; J_x(x) \; \ln \frac{\sqrt{(x'-x)^2 + (y'-b)^2 + c^2} - (y'-b)}{\sqrt{(x'-x)^2 + (y'-a)^2 + c^2} - (y'-a)} \qquad (21b)$$

$$B_x^v = \frac{-\mu \Delta\sigma}{4\pi\sigma} \int_{-\infty}^{\infty} dx \; J_3(x) \; \ln \frac{\sqrt{(x'-x)^2 + (y'-b)^2 + d^2} + d}{\sqrt{(x'-x)^2 + (y'-b)^2 + c^2} + c} \qquad (21c)$$

$$B_3^v = \frac{\mu \Delta\sigma}{4\pi\sigma} \int_{-\infty}^{\infty} dx \; J_x(x) \; \ln \frac{\sqrt{(x'-x)^2 + (y'-b)^2 + d^2} + d}{\sqrt{(x'-x)^2 + (y'-b)^2 + c^2} + c} \qquad (21d)$$

It should be kept in mind that the current densities are described by inverse cosine transforms; therefore, (21) actually involves double integration.

Conclusions

A new method of calculating the magnetic field has been discussed which requires surface integration along conductivity boundaries. This method has the advantage over the classic Biot-Savart formulation in that the order of integration is reduced by one dimension. It is by no means a panacea for calculation of magnetic field, as the resulting surface integrals are usually done numerically with all of the attendant problems. There are situations, however, when one or more of the integrations can be done analytically, thus reducing the computer time required. The most important advantage of this approach to the calculation of magnetic fields is that by inspection one can determine the components of the field that will be produced for a given orientation of a conducting boundary.

References

Edwards, R. N., The magnetometric resistivity method and its application to the mapping of a fault, Can. J. Earth Sci., 11, 1136-1156, 1974.

Edwards, R. N., and E. C. Howell, A field test of the magnetometric resistivity (MMR) method, Geophysics, 41, 1170-1183, 1976.

Fitterman, D. V., Electrokinetic and magnetic anomalies associated with dilatant regions in a layered Earth, J. Geophys. Res., in press, 1978a.

Fitterman, D. V., Calculation of self-potential anomalies near vertical contacts, Geophysics, in press, 1978b.

Heaviside, O., Electrical Papers, p. 218-224, Chelsea Publishing, New York, republished 1970, 1892.

Madden, T. R., The resolving power of geoelectric measurements for delineating resistive zones within the crust, The Structure and Physical Properties of the Earth's Crust, ed. by John G. Heacock, Geophysical Monograph Series, 14, 95-105, AGU, Washington, 1971.

Nadeau, Gerard, Introduction to Elasticity, Holt, Rinehart, and Winston, Inc., New York , 285 p., 1964.

Nourbehecht, B., Irreversible thermodynamic effects in

inhomogeneous media and their applications to certain geoelectric problems, Ph. D. thesis, Mass. Inst. of Technol., Cambridge, Mass., 1963.

Stefănescu, S. S., Über die magnetische Wirkung einiger heterogener Medien in der elektrishen Bodenforschung, Ztschr. F. Geoph., 24, 175-183, 1958.

Stefănescu, S. S., and M. N. Nabighian, Über magnetische storfelder als folge senkrechter schichtungen im gleichstrom, Reveu de Géologie et de Géographie, 6, 139-155, Académie de la République Populaire Roumaine, Bucharest, 1962.
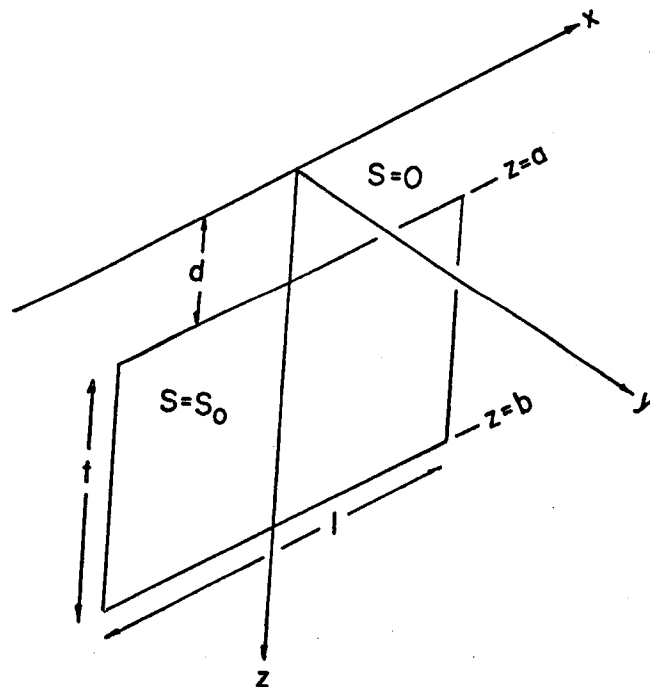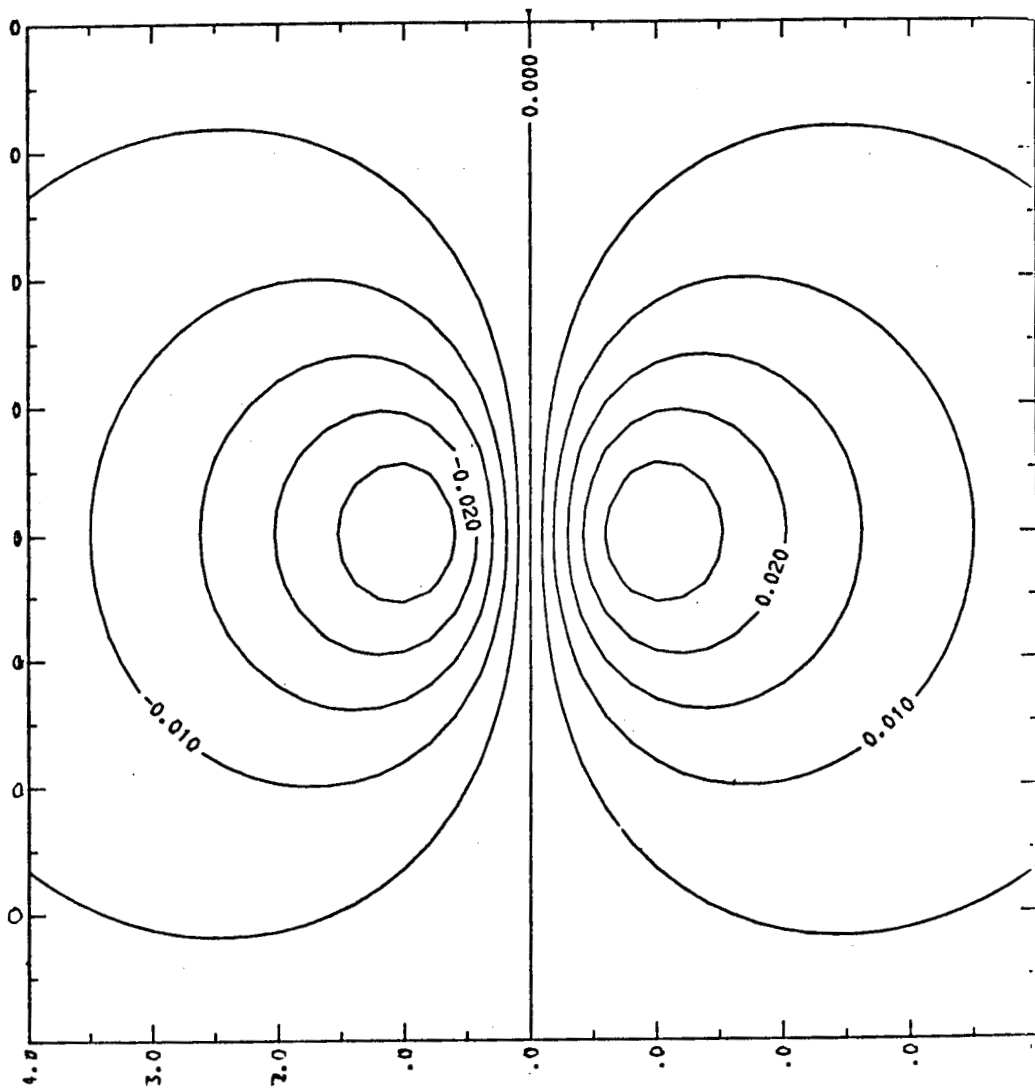
Figure 1 Geometry of rectangular constant source model. Inside the rectangle the source has an intensity of 1 volt and outside it is zero.

Figure 2 Self-potential surface map for rectangular constant-source model. Depth extent is 1, length is 1, and depth is 1. The conductivity is 1 S/m on both sides of the contact. The source intensity is 1 V. The contour interval is 5 mV. Distances are dimensionless.
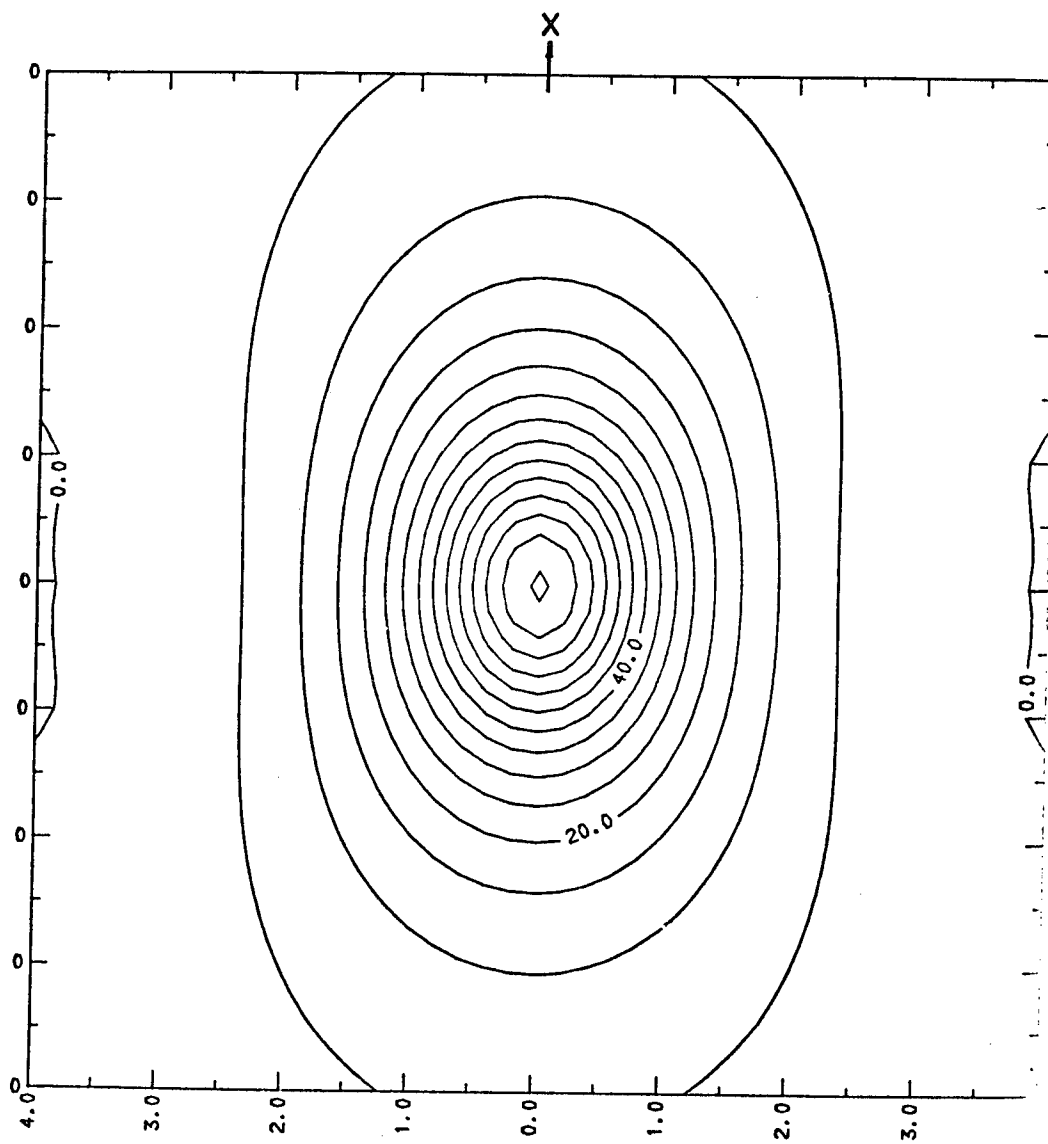
Figure 3 Bx surface map. Parameters are the same as Figure 2. Contour interval is 5 nT.
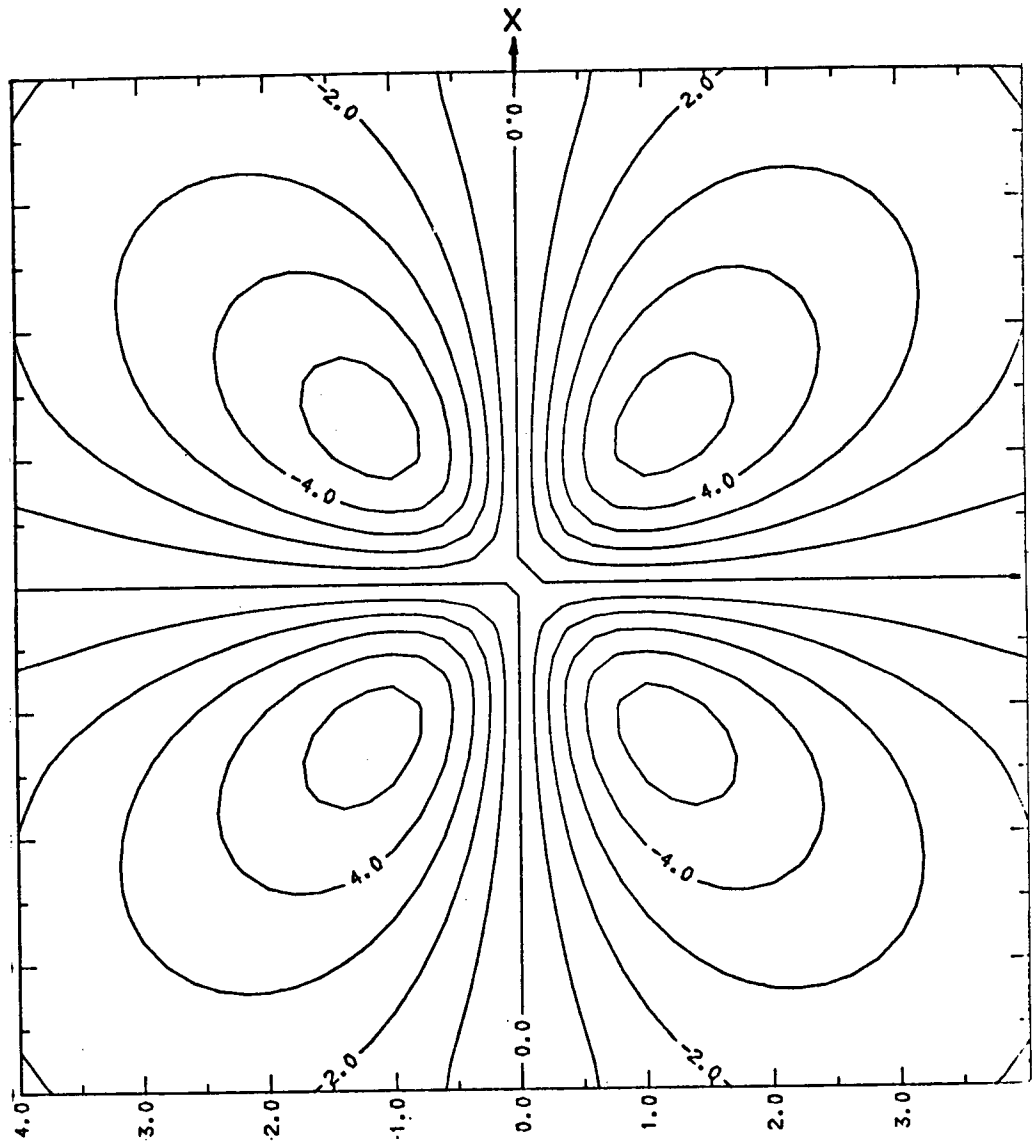
Figure 4 By surface map. Parameters are the same as Figure 2. Contour interval is 1 nT.
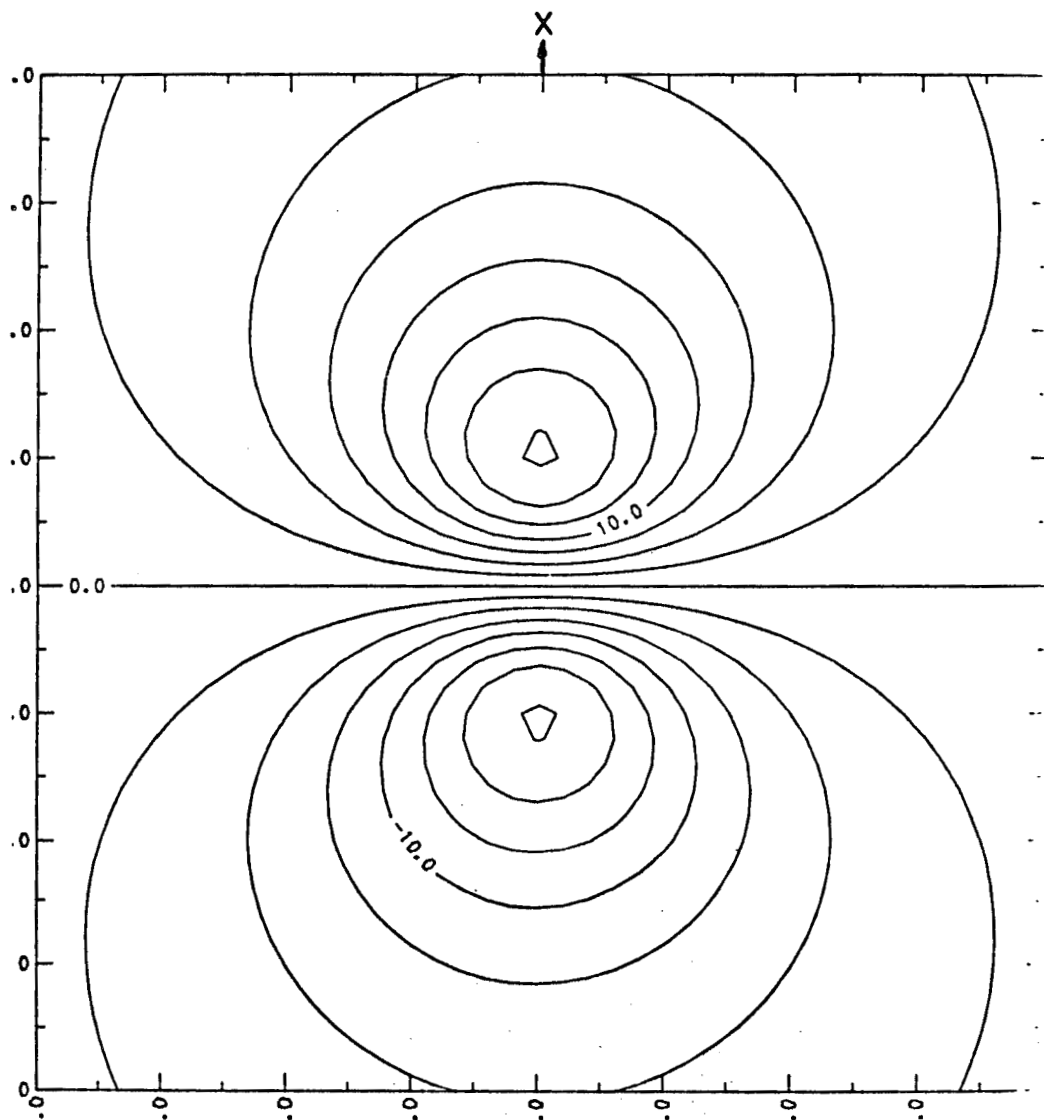
Figure 5 Bz surface map. Parameters are the same as Figure 2.
Contour interval is 2.5 nT.

SUMMARY

D.F. Pridmore
W.R. Sill

The bulk of the presentations covered the application of the classical numerical modeling techniques (i.e., finite element, finite difference, integral equation, and mode matching) to the problems addressed at the workshop. Of the twenty-three presentations on modeling, only one author discussed scale modeling; the other papers dealt with some aspect of numerical modeling. We feel that this ratio reflects the relative amount of research being carried out on the two types of modeling.

Solutions to the three-dimensional electromagnetic scattering problems were reported in all the sessions on the classical techniques. Don Pridmore showed solutions obtained with the finite element method, Walter Jones discussed solutions obtained with the finite difference method, and Jerry Hohmann and Ed Mozley presented results from integral equation methods. All the authors reported computational difficulties arising from the large matrices which need to be assembled and inverted, although the difficulties were not too severe in the integral equation solution for models characterized by compact bodies with low conductivity

contrasts. Most of the authors noted that higher-order basis functions would be a useful extension of their work, although none were optimistic that such functions would remove the computational difficulties associated with the three-dimensional problem.

Solutions using the differential equation techniques were reported for the three-dimensional-source, two-dimensional-earth problem. John Stodt and Ki Ha Lee discussed their work with the finite element method, and Charles Stoyer reported on his earlier work with the finite difference method. It was clear that the essential difficulty in this problem is making an effective choice for the values of the Fourier transform variable.

Gordon West presented results, obtained with an integral equation method, for a thin plate of finite length-extent, excited by a three-dimensional source.

Alan Howard showed a solution to a rotationally symmetric electromagnetic problem, a dipole in a borehole environment, using the mode matching method.

John Kuo presented the formalism for the general three-dimensional time-domain problem using finite element, and gave some results for the scaler problem of an infinite dyke excited by a line source.

Several solutions to the D.C. electrical problem, using the classical techniques, were discussed. Louis Bartel reported on a three-dimensional solution using an integral equation method, and Roy Greenfield presented a finite difference solution to the axisymmetric problem. Dave Fitterman and Nigel Edwards showed how magnetic fields could be calculated from the scalar electric potential. The authors

pointed out that the integrations required to evaluate the magnetic fields need only be carried out where the gradient of the conductivity is non-zero.

Several presentations were made on what might be called non-classical techniques. Will Sheen and Steve Chang presented hybrid solutions to the electromagnetic scattering problem. The use of finite elements in a central core, and termination of the finite element mesh before the behavior of the field variables is known, were the common features of the two papers. Scheen solved the three-dimensional problem using the appropriate Green's function to evaluate the boundary fields, while Chang used an eigen-function expansion in the exterior region to obtain a solution to the rotationally symmetric problem.

Frank Stenger summarized the different species of basis functions which may be used in numerical methods, concluding that the relatively obscure sinc functions offer the best order of approximation. Bill Petrick reported on how these sinc functions may be applied to the three-dimensional electromagnetic scattering problem. The sinc function approach is fundamentally different from most of the other numerical techniques described at the workshop in that the basis functions are non-zero over the whole domain, instead of being non-zero over just a small section of the domain.

Gordon West briefly described an image technique which might be useful for calculating the electromagnetic response of a layered earth in which one or more of the layers have a somewhat irregular shape. West expected this approach to be significantly cheaper than the analysis carried out by a full finite-element or finite-difference

solution. Ted Madden illustrated the profound effect of a resistive lower crust on magnetotelluric measurements, and pointed out that a "multiple scale" approach is an important aid for calculation of such effects.

Phil Wannamaker·illustrated the inadequacy of one- and two-dimensional solutions in the interpretation of a detailed set of magneto-telluric observations made in a geothermal area in southern Utah.

Al Tripp showed how Cohn's sensitivity theorem may be used to calculate, trivially, the perturbation in D.C. potential due to a perturbation in the conductivity structure, once the solution for the unperturbed model is known. The important application of this result is in the inverse problem, where such derivatives are required.

Terry Killpack presented the results of an investigation into the suitability of mini-computers for multi-dimensional modeling algorithms. The author pointed out that the limited addressing capabilities of most mini-computers would make it impossible to simply transfer a working program from a large main-frame computer to most mini-computers. However, the recent development of mini-computers with virtual memory removed this restriction. Killpack noted that it was difficult to determine, a priori, the cost effectiveness of a mini-system, but a crude analysis indicated that a large mini-computer, such as the VAX 11/780, may be the most cost-effective approach.

Brian Spies reported on a novel approach to scale modeling of transient electromagnetic data. By using materials with a relatively high conductivity, Spies noted that it was possible to simulate earth conditions in a relatively small laboratory facility.

Our conclusions on the state-of-modeling of electrical and electro-magnetic modeling are as follows:

(i) The classical techniques give satisfactory solutions to the scalar electromagnetic problems, and one-, two-, and possibly three-dimensional resistivity problems. By satisfactory, we mean that the solutions are relatively well documented in the literature, and that they can be solved on available computers, without excessive effort. Solutions to the vector electromagnetic problems, such as the three-dimensional-source, two-dimensional-earth, and the full three-dimensional problem, can require significant computational resources when approached via the classical techniques. Research into hybrid techniques, the use of different basis functions, and special methods for certain restricted models, is urgently needed for this class of problem.

(ii) It is clear that, in the near term, accurate solutions to a wide class of three-dimensional models will come only from either scale-model studies or from numerical solutions generated by using unprece-dented amounts of computer time.

The participants drew up a set of recommendations, which follows.

RECOMMENDATIONS

The following recommendations and comments were made and approved by participants at the workshop.

1. Dedicated Mini-Computers for Modeling

   Preliminary investigations indicate that 32-bit mini-computers (such as the VAX 11/780 might offer a more cost-effective way to conduct large modeling exercises than the fast main-frame computers (such as the CDC 7600). It was agreed that a careful and complete cost/benefit study and comparison is needed. It was also agreed that a dedicated mini-computer had to be accessible via remote terminals to many users, and that it be located at a facility where continuity and support of operations is assured, e.g., a National Laboratory.

2. Full Differential Equation Methods Should Be Pursued

   Although differential equation methods (e.g., finite element, finite difference, sinc-galerkin methods) usually require greater computational effort than integral equation, hybrid, and analytic methods, it is this class of solutions which is amenable to the complex geological conditions most often found in nature.

3. Integral Equation, Hybrid, and Analytic Methods Should Be Pursued

   These methods are preferred to the full differential equation methods for relatively simple geometries, since they are less expensive, computationally, and are very useful for gaining an understanding of the physics of the problem.

4. **Encourage the Development of Innovative and Inexpensive Techniques to Handle Special Problems**

5. **Increase Scale Modeling Efforts**

    Scale modeling efforts need to be increased to obtain an understanding of the physics in these problems and as a check on the numerical modeling algorithms.

6. **Standard Model Suite**

    A standard model suite was adopted for the purpose of comparing calculated results from different programs. It included the same three models suggested during the Workshop on "Electromagnetic Exploration in Deeply Weathered Terrains" held in Sydney, Australia in November 1977. In addition, a rotationally symmetric model was added to this set. The models are shown in Figures 1, 2, and 3.

7. **Technology Transfer Should Be Improved**

    A major effort is needed to refine, optimize, and document existing programs, so that they are readily useable at centers other than the development site. It was agreed that not enough is being done to document programs at present. Programs are often lost or are unuseable when graduate students depart, and follow-on students must either start all over or do a major program revision.
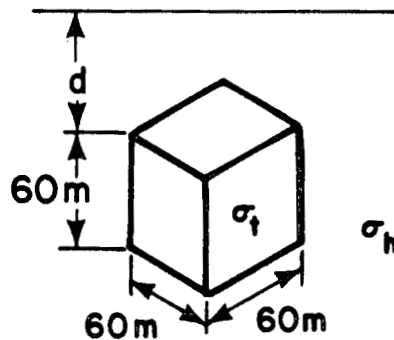
8. **Explore Inverse Problems**

    Simple yet direct, low-cost inverse solutions should be sought for the low-frequency electromagnetic problem.

Body I (Hohmann)
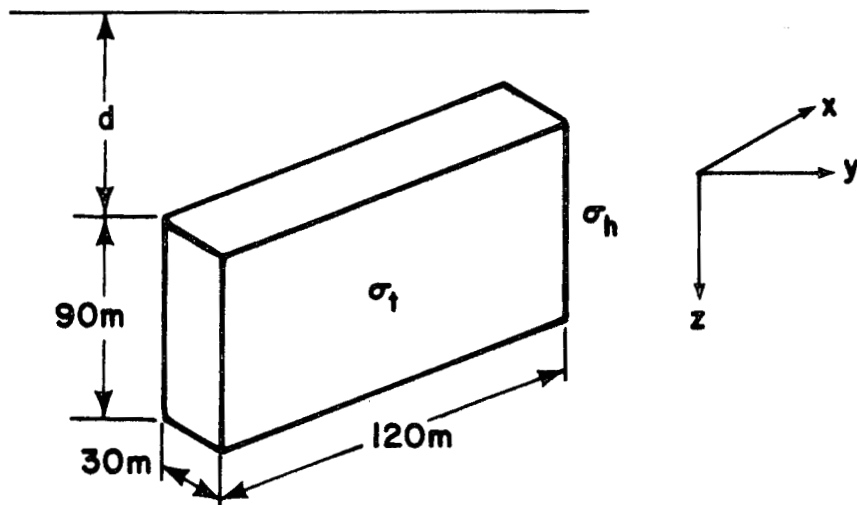
Body 2 (Cube)

XBL 787-1400

For Body 1 and 2

$$d = 30m, 60m$$
$$\sigma_t = 1 \text{ s/m}$$
$$\sigma_h = 0.01, 0.1 \text{s/m}$$
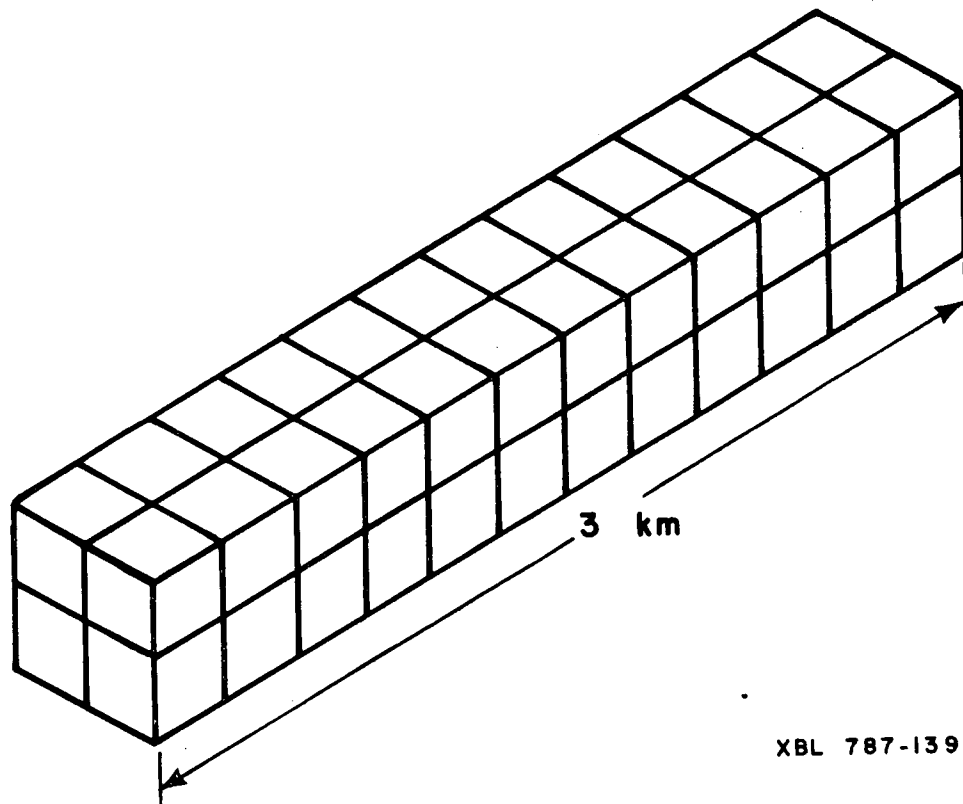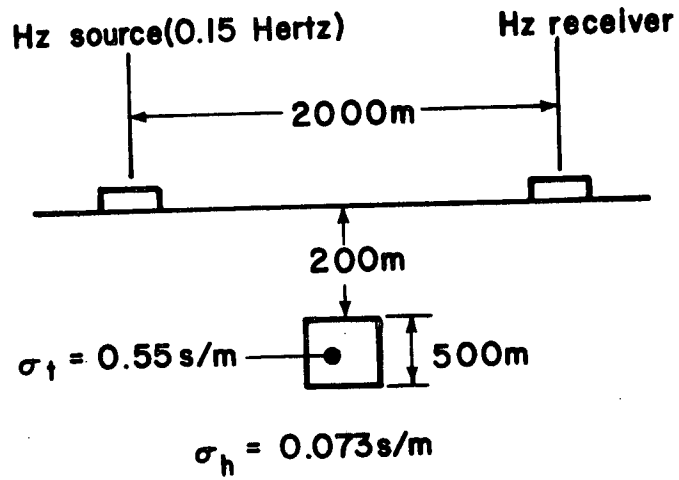Frequency = 30, 100, 300, 1000, 3000 Hz
Slingram spacing = 30, 60, 120m
Crossed E dipoles = 30m. long at 120m from y-face

Figure 1: Standard models adopted by the workshop. The rectangular geometry is easily approximated by the usual three-dimensional modeling algorithms. These models are based on the work by Hohmann.
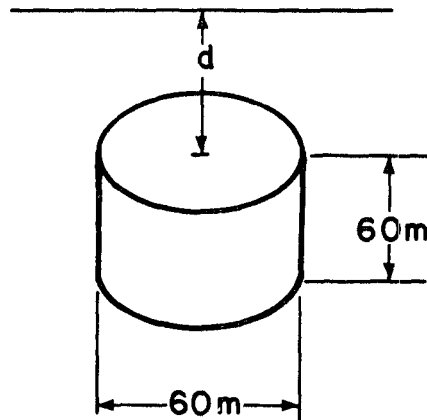
Body 3 (Frischknecht)

Figure 2: Standard model adopted by the workshop. Model used by Frischknecht in scale modeling experiments.

Body 4

XBL 787-1402

For Body 4

$$d = 30m, \ 60m$$

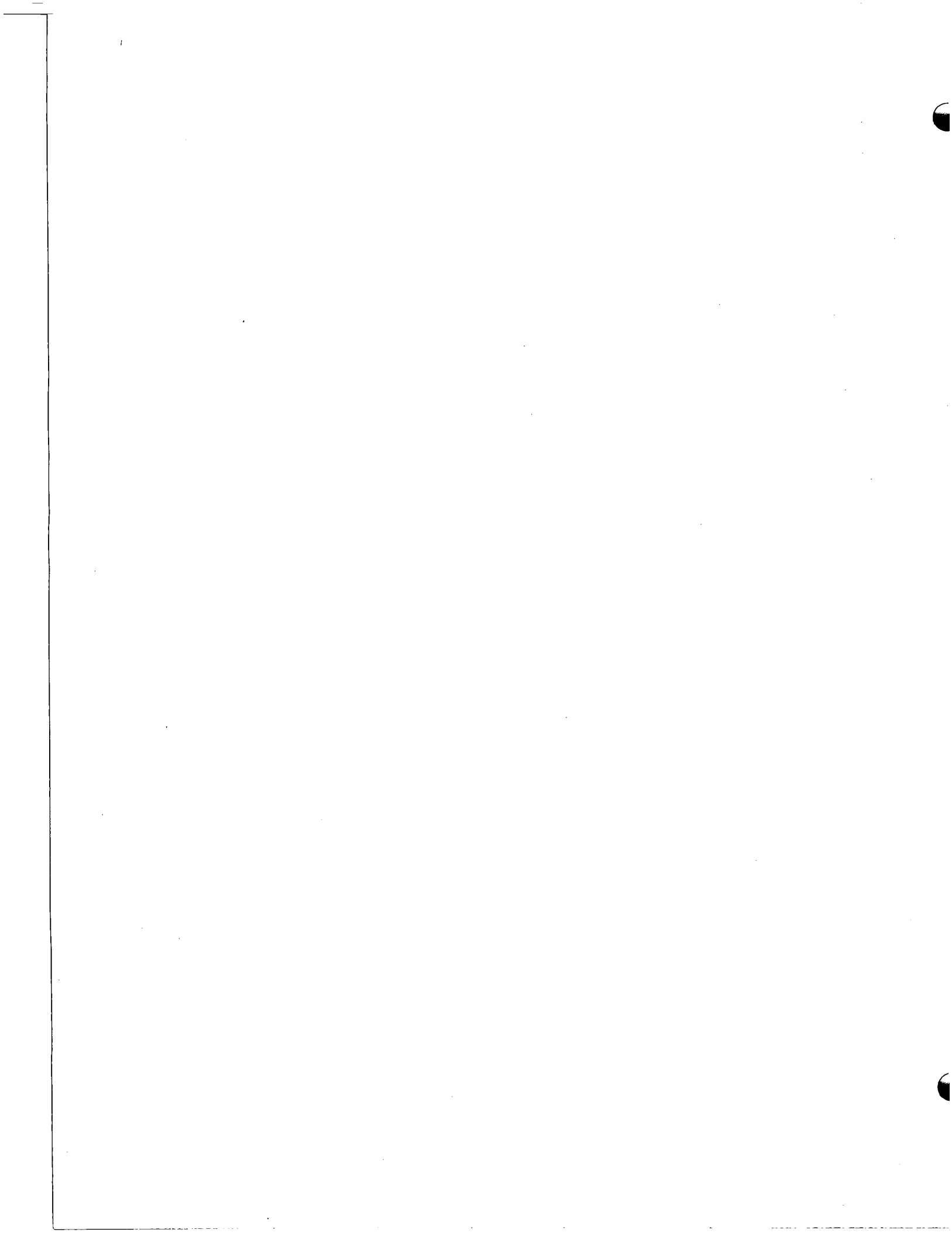$$\sigma_t = 1 \ s/m$$

$$\sigma_h = 0.01, \ 0.1 \ s/m$$

$$Frequency = 30, \ 100, \ 300, \ 1000, \ 3000 \ Hz$$

$$Slingram \ spacing = 30, \ 60, \ 120 \ m$$

Figure 3: Standard models adopted by the workshop. Rotationally

symmetric model which can be easily approximated by the

usual two-dimensional modeling algorithms.

PARTICIPANTS

Dhari S. Bahjat

Continental Oil Co.
Ponca City, OK 74601

Lou C. Bartel

Sandia Laboratories
Geotechnology Research Div.
Albuquerque, NM 87115

Mel Best

Shell Canada Ltd.
Shell Building
Minerals Department
Exploration and Production
Calgary, Alberta
Canada

Steve Chang

Science Applications, Inc.
125 University Avenue
Berkeley, CA

Nigel Edwards

Geophysics Laboratory
Department of Physics
University of Toronto
Toronto, Ontario M5S1A7
Canada

Dave Fitterman

U.S. Geological Survey
MS 964 Box 25046
Denver Federal Center
Denver, CO 80225

Norm Goldstein

Lawrence Berkeley Laboratory
Rm 1042 Building 90
Berkeley, CA 94720

Roy J. Greenfield

Pennsylvania State University
600 N. McKee Street
State College, PA 16801

Jerry Hohmann

Department of Geology & Geophysics
University of Utah
Salt Lake City, UT 84112

Allen Howard, Jr.

Department of Electrical Engineering
University of Arizona
Tucson, AZ 85719

F. Walter Jones

Department of Physics
University of Alberta
Edmonton T6G2J1
Canada

Terry Killpack

Earth Science Institute
Research Park
Salt Lake City, UT

John Kuo

Krumb School of Mines
Columbia University
New York, NY 10027

Ki Ha Lee

Engineering Geoscience
University of California
Berkeley, CA 94720

Jeff Lytle

Lawrence Livermore Laboratory
P.O. Box 808
Livermore, CA 94550

Ted Madden

Department of Geology & Geophysics
Massachusetts Institute of Technology
Cambridge, MA 02139

Mario Martinez G.

C.I.C.E.S.E.
Espinoza 843
Ensenada, B.C.
Mexico

Frank Morrison

Engineering Geoscience
University of California
Berkeley, CA 94720

Ed Mozley

Engineering Geoscience
University of California
Berkeley, CA 94720

Bill Petrick

Department of Geology & Geophysics
University of Utah
Salt Lake City, UT 84112

Don Pridmore

Engineering Geoscience
University of California
Berkeley, CA 94720

I. K. Reddy

Shell Development Co.
P.O. Box 481
Houston, TX 77001

Will Scheen

KSEPO
Volmerlaan 6
Rijswijk, Holland 2289GD

Bill Sill

Department of Geology & Geophysics
University of Utah
Salt Lake City, UT 84112

Brian Spies

School of Earth Sciences
Macquarie University
North Ryde, Sydney
N.S.W. Australia 2113

Frank Stenger

Department of Mathematics
University of Utah
Salt Lake City, UT. 84112

John Stodt

Department of Geology & Geophysics
University of Utah
Salt Lake City, UT 84112

Charlie Stoyer

Department of Geophysics
Colorado School of Mines
Golden, CO 80401

Charlie Swift

Chevron Resources Company
320 Market Street
San Francisco, CA 94111

Sam Ting

Department of Geology & Geophysics
University of Utah
Salt Lake City, UT 84112

Allan Tripp

Department of Geology & Geophysics
University of Utah
Salt Lake City, UT 84112

Keeva Vozoff

Engineering Geoscience
University of California
Berkeley, CA 94720

Phil Wannamaker

Department of Geology & Geophysics
University of Utah
Salt Lake City, UT 84112

Stan Ward

Department of Geology & Geophysics
University of Utah
Salt Lake City, UT 84112

Gordon West

Geophysics Laboratory
Department of Physics
University of Toronto
Toronto, Ontario M5S1A7
Canada